ESA contract 4200021396
CCN2

FURTHER VALIDATION AND REFINEMENT OF THE TENTI MODEL FOR ATMOSPHERIC LIDAR BACKSCATTER

Final Report

Ziyu Gu and Wim Ubachs,

Department of Physics and Astronomy, and LaserLaB,
Vrije Universiteit Amsterdam, The Netherlands

March 2014

ESA STUDY CONTRACT REPORT

No ESA Study Contract Report will be accepted unless this sheet is inserted at the beginning of each volume of the report

ESA CONTRACT No	**SUBJECT**	**CONTRACTOR**
21396/07/NL/HE	Further Validation and Refinement of the Tenti Model for Atmospheric Lidar Backscatter	LaserLAB, Vrije Universiteit Amsterdam, Netherlands
*** ESA CR( ) No** CCN2	**No of Volumes:** 1 **This is Volume No:** 1	**CONTRACTOR'S REFERENCE** Final Report of CCN2 to ESA contract 4200021396

ABSTRACT:

The objective of this study was to further validate and refine the Tenti Model for Atmospheric Lidar Backscatter in temperature, wavelength and scattering angle space. This was achieved through experimental Rayleigh-Brillouin scattering measurements recorded in the laboratory using a home-built setup. The set-up included a high-power narrowband tuneable laser source in the ultraviolet and blue range of the spectrum, an enhancement cavity to produce some 5 Watts of power in the scattering zone, and a Fabry-Perot spectral analyzer that records the spectrum at a 90 degrees scattering angle. Scattering in the forward direction could not be tested in this activity due to technical and time constraints. RB-spectra are obtained in air for both 366 nm and 403 nm wavelengths for a pressure-temperature parameter space covering 0.3, 0.75, 1.0 and 3.0 bar and -20, 4, 24, 45 and 65 ^{o}C. These data match predictions from the TENTI S6 model to 1% accuracy, if the proper values for the macroscopic transport coefficients are included. In this model also a value for the bulk viscosity is used, which is derived from the present optical data. The TENTI model calculations can be used to retrieve the temperature levels in the experiment to within 0.4 ^{o}C.

The work described in this report was done under ESA contract. Responsibility for the contents resides in the author or organization that prepared it.

Names of authors:
Ziyu Gu and Wim Ubachs

**** NAME OF ESA STUDY MANAGER**	****ESA BUDGET HEADING**
Anne Grete Straume-Lindner **DIV:** TEC-EE	ESA's basic Technology Research Programme (TRP)

* Sections to be completed by ESA

** Information to be provided by ESA Study Manager

FURTHER VALIDATION AND REFINEMENT OF THE TENTI MODEL FOR ATMOSPHERIC LIDAR BACKSCATTER

Executive Summary

General background to the project

The present study on laboratory Rayleigh-Brillouin scattering is intimately linked to future lidar missions of the European Space Agency. The immediate connection is to the ADM-Aeolus mission aiming to measure wind profiles in the Earth atmosphere *on a global scale*. This is pursued by *active* remote sensing, i.e. by measuring the spectral profile of the back-scattered light from an ultraviolet laser on board of the satellite.

In the recent past it was noted that the molecular scattering functions are not Gaussian profiles and the deviations from gaussianity will influence the Doppler measurements and impact the wind profile analysis. In particular acoustic phenomena known to produce the characteristic Brillouin side-wings on the Doppler profile have a strong effect. This was identified as a major problem in a previous study (the ILIAD report[1]) and it was estimated that neglecting the Brillouin effect will result in errors in the radial wind measurement of up to 10% in several cases. These estimates were made on the basis of models known in the literature since the 1970s as the TENTI models. These TENTI models had only been tested for a few measurement configurations and for a very small subspace of gases, pressures and mixtures. It had not been tested for air under the various atmospheric conditions. Hence the goal of subsequent ESA-funded projects was defined: measuring the spontaneous Rayleigh-Brillouin (RB) scattering profile and comparing them to both versions of the TENTI-models (the so-called TENTI S6 and TENTI S7 varieties) in conditions relevant for upcoming ESA LIDAR missions.

A first study was performed to verify the TENTI models for various conditions of light scattering [2]: A *spontaneous* Rayleigh-Brillouin light scattering experiment was performed for wavelengths of 366 nm in the ultraviolet, and an additional experiment on coherent Rayleigh-Brillouin light scattering at 532 nm. Good agreement with the TENTI S6 model was obtained. Spectral profiles were reproduced to within 2% of theoretical predictions of a code based on the TENT S6 model and including as input the macroscopic gas transport coefficients such as the heat conductivity, the shear viscosity, the internal specific heat capacity, and the elusive bulk viscosity. Measurements were performed for pure nitrogen and oxygen, as well as air at various pressures. The combination of spontaneous and coherent RBS experiments allowed for a test in a wide range of the possible parameter space. As an important general result it was shown that with currently available optical and laser equipment high-quality spontaneous RB-scattering profiles could be measured at atmospheric pressures, much better than obtained in previous decades. The 18-month duration of the first measurement campaign was too short to cover the entire parameter space. Some important issues were left open to be dealt with in an extension study (CCN2) on which we report now. In particular *temperature*-dependent as well as *wavelength*-dependent phenomena were identified as relevant topics to deal with in extended studies. Furthermore *angle*-dependent scattering effects as well as *polarization*-dependent effects were mentioned as possible targets of study; however these are not covered in the present study, although preparations for angle-dependent studies have reached a stage (with a new experimental setup ready) that these may be performed soon.

---

[1] C. Loth, P. H. Flamant, A. Dabas, M.-L. Denneulin, A. Dolfi-Bouteyre, A. Garnier and D. Rees, *ILIAD - Impact of Line Shape on Wind Measurements and Correction methods,* ESA Contract No 18334, (2005).

[2] W. Ubachs, E.-J. van Duijn, M.O. Vieitez, W. van de Water, N. Dam, J.J. ter Meulen, A.S. Meijer, J. de Kloe, A. Stoffelen, E.A.A. Aben, *A Spontaneous Rayleigh-Brillouin scattering experiment for the characterization of atmospheric Lidar backscatter*, ESA report, AO/1-5467/07/NL/HE (2009).

Some highlights of results

In the present study a large data set is collected on Rayleigh-Brillouin spectral profiles covering the parameter space of pressures and temperatures relevant to the Earth atmosphere. These experimental data (all for 90 degrees scattering and for wavelengths 366 nm and 403 nm) were confronted with the TENTI S6 model calculations. Part of the data obtained for 366 nm are displayed in Fig. 1.

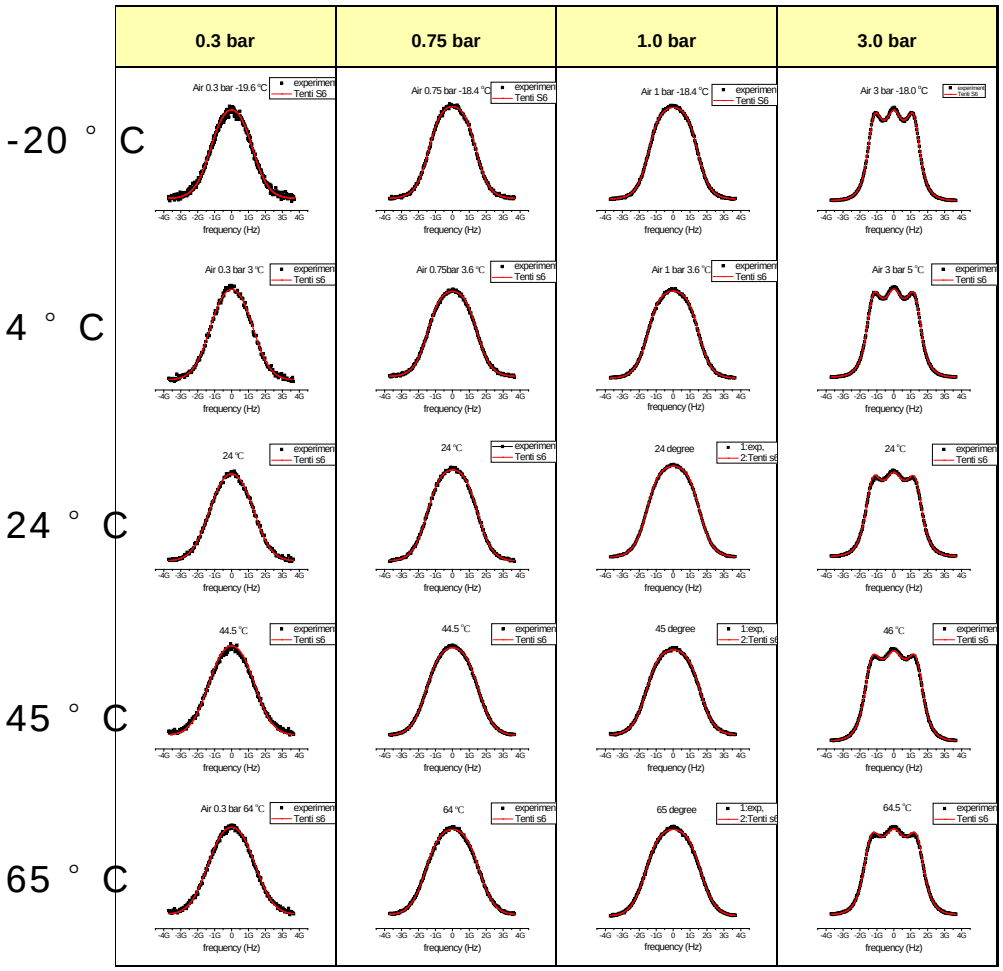

Fig. 1: Collection of RB scattering measurements in air for various (p,T) settings at 366 nm.

The data obtained for pressures of 3 bar allow for a determination of the bulk viscosity. This is a macroscopic transport coefficient that has been determined through acoustic measurements, but it is anticipated that the actual values for light scattering frequencies (in the GHz domain) may not correspond to those derived from acoustic data (in the MHz domain). The large data set allows for a determination of the bulk viscosity in air for a range of temperatures. The values for η_b, obtained for higher pressures, where bulk viscosity is a prominent effect, can be inserted in the TENTI model, also for the atmospheric range. That defines the rationale to perform dedicated measurements at super-atmospheric pressures. It is found, as a central result of the present study, that the bulk viscosity increases with temperature, as does the shear viscosity (see Fig. 2).

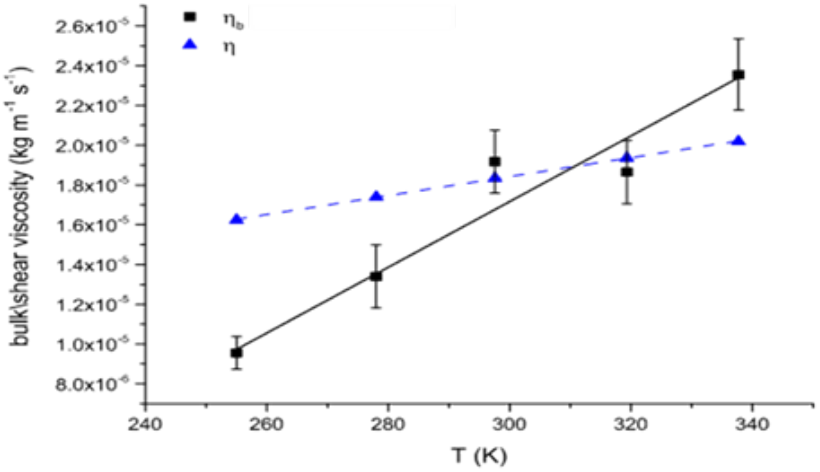

Fig. 2: Results on values for the bulk viscosity in air, compared to the shear viscosity, derived from measurements at 366 nm.

Also, the large experimental data set was included in a retrieval analysis. The observed RB spectral profiles were, after a determination of the bulk viscosity η_b, implemented in a retrieval procedure to determine the gas temperature. The data at 366 nm and relevant to atmospheric pressures are analyzed in Fig. 3. This procedure is also performed for a second set of data recorded for at a wavelength of 403 nm.

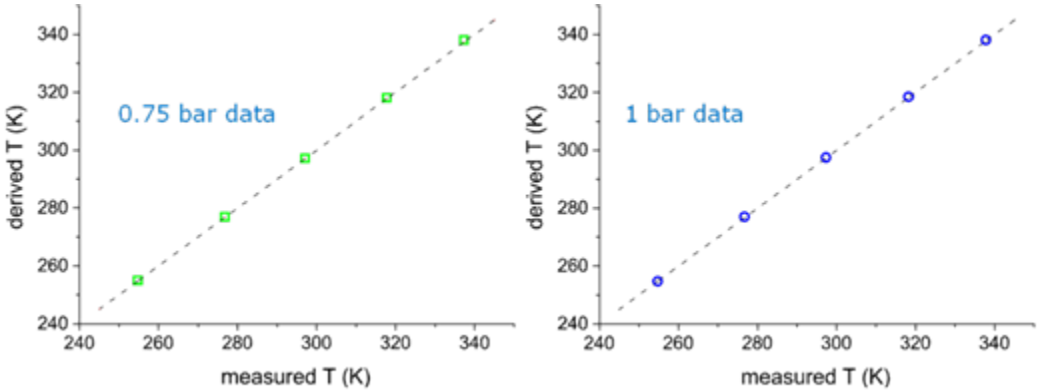

Fig. 3: Temperature retrieval from the RB-scattering profiles measured in the present study, derived from measurements at 366 nm.

A maximal difference of 0.4 K is obtained between the retrieved and the measured temperatures (see Fig. 3), provided that all the other conditions (pressure, angle) and the transport coefficients are known to a high accuracy.

Overall the TENTI model is tested in a wide parameter space and the accuracy of the representations of the RB scattering profile (for 90 degrees scattering) reaches the 1% level when using the bulk viscosity as determined in Figure 2. Some deviations pertain that seem to be systematic. Such deviations could be related to a few causes:

- The TENTI model is only an approximation, involving a truncation of the full Boltzmann equation in 6 terms. As for any approximation the validity is limited.
- There is a physical shortcoming of treating air as a single component gas, where in fact air is a mixture of nitrogen and oxygen (with some minority species, that will have only little influence on the scattering profile; previously it was found that

even a saturated amount of water vapor does not yield measurable effects on the scattering profile).

- The TENTI model does not consider depolarized scattering such as Rayleigh-wing scattering and Raman scattering, which our setup is sensitive to. Rayleigh-wing scattering does not occur for molecules with an isotropic polarizability tensor, such as O_2, N_2 (hence air). Most part of the Raman scattering corresponds to a large frequency shift and is ascribed to be the reason for the background of the measurements at 366 nm. This background is fully reduced by implementing a narrow band filter (1 nm) for 403 nm measurements. Comparison between the measurements with and without the narrow band filter indicates that the background does not influence the results of our measurements. A special part of rotational Raman scattering, corresponding to no frequency shift, is estimated to be ~1 % of the total scattering. This scattering component is a possible reason for the 1~2 % deviation between the measurements and the model in centre of RB-scattering profiles.

The second issue makes that the study of gas mixtures is a valid one for testing the RB-profiles of air. In all prevailing theoretical models air is treated as a single-component gas consisting of particles with mass 29, and the transport coefficients as experimentally determined for air.

For this reason an attempt was made to perform measurements of an extreme case: a mixture of He and Ar gas. The scattering profiles, as shown below, demonstrate that the RB-scattering profile of Argon (at 2 bar in each case) becomes different if 2 bar He-gas is added, although the contribution of the He-gas to the scattering profile may be ignored (in view of its tiny cross section). It is concluded that the TENTI-model is not suited to describe the RB scattering of gas mixtures.

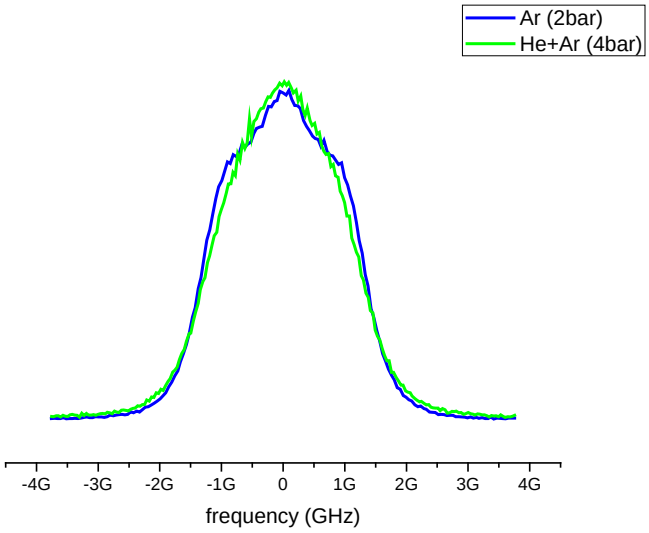

Fig. 4: Collection of RB scattering measurements in air for various (p,T) settings.

There remain some further open issues in testing the TENTI models for light scattering. The parameter space is not fully covered: *angle*-dependences are not yet investigated. Also the effects of polarization remain a target for future studies.

As an outcome of the Rayleigh-Brillouin studies at LaserLaB VU the following papers were published in the scientific literature:

Scientific Papers

Y. Ma, H. Li, Z. Gu, W. Ubachs, Y. Yu, J. Huang, B. Zhou, Y. Wang, K. Liang
Analysis of Rayleigh-Brillouin spectral profiles and Brillouin shifts in nitrogen gas and air, Optics Express 22, 2092-2104 (2014)

Z. Gu, B. Witschas, W. van de Water, W. Ubachs
Rayleigh-Brillouin scattering profiles of air at different temperatures and pressures, Appl. Optics 52, 4640 (2013)

Z. Gu, W. Ubachs
Temperature-dependent bulk viscosity of nitrogen gas determined from Rayleigh-Brillouin scattering,
Optics Letters 38, 1110 (2013)

Z. Gu, M.O. Vieitez, E.-J. van Duijn, W. Ubachs
A Rayleigh-Brillouin scattering spectrometer for ultraviolet wavelengths,
Rev. Scient. Instrum. 83, 053112 (2012)

M.O. Vieitez, E.-J. van Duijn, W. Ubachs, B. Witschas, A. Meijer, A.S. de Wijn, N. Dam, W. van de Water,
Coherent and spontaneous Rayleigh-Brillouin scattering in molecular gases and gas mixtures,
Phys. Rev. A 82, 043836 (2010)

B. Witschas, M.O. Vieitez, E.-J. van Duijn, O. Reitebuch, W. van de Water, W. Ubachs,
Spontaneous Rayleigh-Brillouin scattering of ultraviolet light in nitrogen, dry and moist air, Appl. Optics 49 (2010) 4217-4227

Further papers in preparation:

Z. Gu et al.
RB-scattering in air for various (p,T) , and comparison with N_2 and O_2, at 403 nm
In preparation

B. Witschas, Z. Gu, W. Ubachs
Temperature retrieval from RB scattering data
In preparation

Z. Gu, W. Ubachs, W. van de Water
Rayleigh-Brillouin scattering of carbon dioxide
In preparation

Z. Gu, W. Ubachs, W. Marques, W. van de Water
RB-scattering in gas mixtures: HeAr, He Kr
In preparation

CONTENTS

List of acronyms

ADM-Aeolus	Atmospheric Dynamics Mission- Earth Explorer
AR coated	Anti-Reflection coated
CRBS	Coherent Rayleigh-Brillouin Scattering
CW	Continuous Wave (laser light, for example)
ESA	European Space Agency
F	Finesse (of an etalon)
FPI	Fabry-Perot Interferometer
FSR	Free Spectral Range
FWHM	Full Width at Half Maximum
laser	Light Amplification by Stimulated Emission of Radiation
Lidar	LIght Detection And Ranging or Laser Imaging Detection And Ranging
LOS	Line-of-Sight
Nd:YAG laser	Neodymium-Doped Yttrium Aluminium Garnet ($Nd:Y_3Al_5O_{12}$) crystal as laser medium
PMT	Photo-Multiplier Tube (light detector)
Q-switch	Quality-factor switch (inside a laser cavity)
RBS program	Updated tenti code, provided by Willem van de Water
RBS	Rayleigh-Brillouin Scattering
ROC	Radius of Curvature
SHG	Second Harmonic Generation – create frequency 2ω of and original frequency ω
SRBS	Spontaneous Rayleigh-Brillouin Scattering
Ti:Sa laser	Titanium-doped Sapphire crystal as a laser medium
VU	Vrije Universiteit

List of symbols

$\mathbf{r}$	position vector of the particles (molecules or atoms)
t	time
$\varepsilon(\mathbf{r},t)$	instantaneous dielectric constant
ε_0	mean dielectric constant
$\boldsymbol{v}$	velocity vector
c	speed of light in vacuum (299792458 m/s)
n	index of refraction of the medium
$\boldsymbol{k}$	propagation vector of the laser
f	frequency
$\omega = 2\pi f$	angular frequency of the incident electric field (SRBS)
$\sigma(\mathbf{k}, \omega)$	scattering cross section
$S(\mathbf{k}, \omega)$	Space-time Fourier transform of the density correlation function, gives the shape of the Rayleigh-Brillouin peaks.
T	temperature
k_B	Boltzmann constant
m	mass of the molecule
$x = \omega/(kv_S)$	generalized frequency scale
κ	thermal conductivity
η	shear viscosity
η_b	bulk viscosity
$y = (1/2\pi)(\Lambda/L) = 1/(kL)$	kinetic parameter y
λ	wavelength
ρ	gas density
c_P	isobaric heat capacity
c_V	heat capacity at constant volume
$\gamma = c_P/c_V$	adiabatic index
$F_k(v)$	King factor: gives the contribution to the unpolarized scattering due the non-sphericity of the molecules
α	molecular polarizability
J	collision operator
$f(\boldsymbol{r},\boldsymbol{v},t)$	microscopic phase-space density
$\Phi(v)$	Maxwell distribution
$h(\boldsymbol{r},\boldsymbol{v},t)$	deviation (fluctuation) from equilibrium (Maxwell distribution) of the microscopic phase-space density, $f(\boldsymbol{r},\boldsymbol{v},t) = \Phi(v)(1 + h(\boldsymbol{r},\boldsymbol{v},t))$

Part I

1 Introduction

The present study is intimately linked to future missions of the European Space Agency. The immediate connection is to the ADM-Aeolus mission (see Figure 1-1) aiming to produce a velocity (wind) profile of vertical layers in the Earth atmosphere *on a global scale*. This is pursued by *active* remote sensing, i.e. by measuring the spectral profile of the back-scattered light from an ultraviolet laser on board of the satellite. An ultraviolet wavelength is chosen in the range where (i) powerful lasers are available, (ii) absorption is minimal, and (iii) the scattering cross section is high, allowing for high quality wind measurements for cloud-free conditions. The backscattered light is encoded with information of the velocity profile of the air-masses in various layers through the Doppler frequency shifted Mie (aerosol particle) and through Rayleigh-Brillouin (molecular) scattering process. The LIDAR principle is employed to gather information from the various atmospheric layers: signals triggered and induced by the short-duration laser pulses arrive at different times on the detector, thus allowing for the conversion of temporal information in terms of depth into the atmospheric layers.

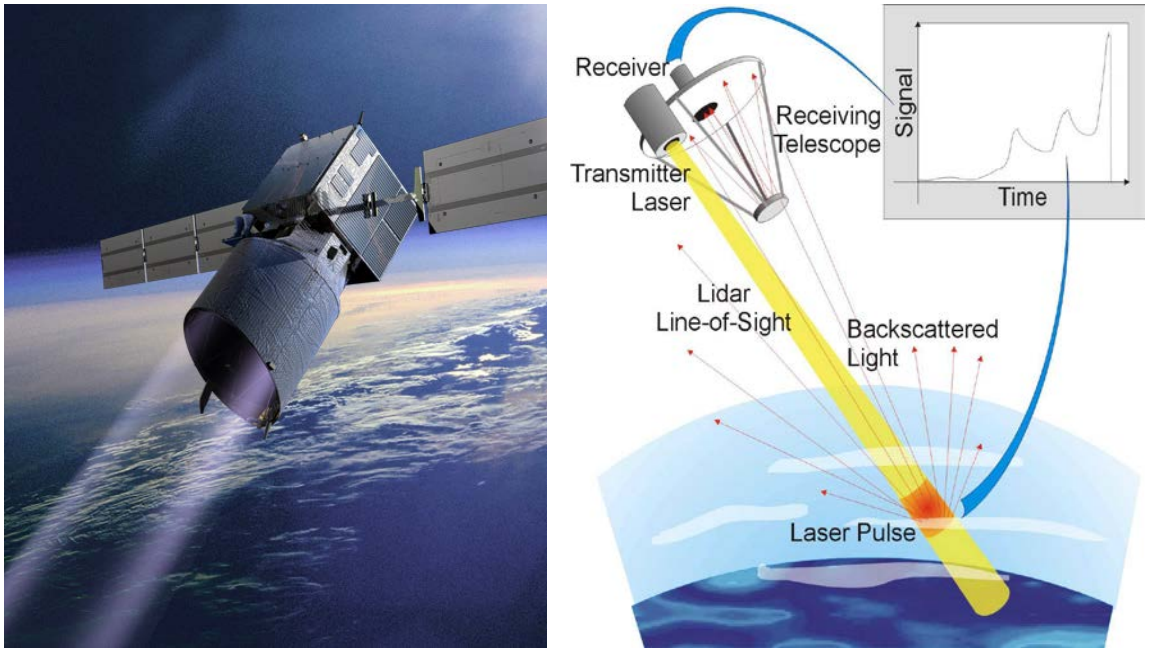

Figure 1-1: A pictorial representation of the ADM-Aeolus satellite mission; on the left the envisioned satellite system, and on the right a physical representation of the wind measurement scheme: a combination of LIDAR and Doppler sensing techniques.

Recently a project was carried out measuring the spontaneous Rayleigh-Brillouin (RB) scattering profile and comparing them to both versions of the TENTI-models (the so-called TENTI S6 and TENTI S7 varieties) in conditions relevant for upcoming ESA LIDAR missions. For this project, funded by ESA [1] two experimental setups were

constructed to measure the Rayleigh-Brillouin profile under various conditions, a coherent RB scattering experiment at the Radboud University Nijmegen, and a spontaneous RB scattering experiment at the “Institute for Lasers, Life and Biophotonics” (LaserLaB), VU University, Amsterdam. In both setups unprecedentedly high signal-to-noise ratios were achieved and accurate tests of the TENTI profile were performed. Rayleigh-Brillouin scattered light from a target cell, filled with N_2, O_2, dry air, humid air, for ranges of pressures at ambient temperature were measured. The obtained spectra represent the best experimental data obtained so far to test lines shape models such as TENTI. Further validation of the Tenti-model at different temperatures, however, is still required for applications in space-borne LIDARs.

In the first part of this report, we present new data on RB scattering profiles using the unique facility of the spontaneous RB spectrometer at the LaserLaB Amsterdam. Measurements are extended to RB-scattering in air and N_2 at varying temperatures in the range -20 ℃ to +65 ℃. Moreover a series of further test measurements on RB scattering in CO_2 are performed. In order to investigate the reproducibility of the setup, we have compared a series of measurements recorded previously with novel data. The experimental data are compared to the Tenti S6 model with the previously developed code (*RBS-program*). Temperature measurements in air at up to 65 ℃ have been performed, recorded at pressures of 300, 750, 1000 and 3000 mbar. Measurements under N_2 under the same conditions are in progress. Water deposition or ice formation on the windows of the scattering gas cell has been recognized as a problem for measurements below 0 ℃, and has hampered progress. A modification of the gas cell has been implemented, which counteract these problems and made measurements at temperatures down to -20 °C possible.

2 The experimental SRBS setup

During a previous study on “A Spontaneous Rayleigh-Brillouin Scattering Experiment for the Characterization of Atmospheric LIDAR Backscatter” [1] an experimental setup was constructed that was successfully implemented to measure Rayleigh-Brillouin (RB) line scattering profiles. The same system with only a slight modification is used to carry out the measurements in this part. Therefore, only the essentials of the experimental system will be described with special emphasis on the modifications. It was decided to perform the first round of measurements at a wavelength of 366.6 nm, similar as in the previous study.

2.1 Laser source

The laser source is a Ti:Sa laser pumped by a Millennia laser. The Millennia laser delivers up to 10 W of laser light at 532 nm wavelength, with a stable output power (1% instability in 20 hours). The Ti:Sa laser (Figure 2-1) is tuned to deliver continuous-wave laser light at the wavelength of 733.3 nm with an output power of 1.5 W. The laser bandwidth is 1 MHz. The wavelength of the Ti:Sa laser is measured by an ATOS wavemeter, that measures the absolute wavelength and feeds the signal to a piezoelectric device attached to a mirror inside the cavity of the Ti:Sa laser.

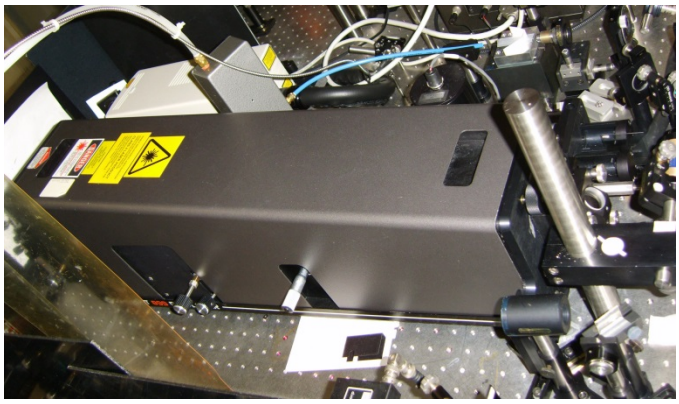

Figure 2-1: Top view of the continuous wave Titanium:Sapphire laser (Coherent Inc.).

2.2 UV laser light from a frequency doubling (SHG) cavity

The UV laser light is generated from a frequency-doubling cavity (Figure 2-2), which doubles the frequency of the laser light, hence converting the wavelength from 733.3 nm to 366.65 nm. With a good adjustment of the SHG cavity, the output UV light can reach an intensity of up to 500 mW, with a bandwidth of 2 MHz. The cavity is locked to the frequency of the Ti:Sa laser (via a home-built Hänsch-Couillaud electronic locking scheme), therefore being equally stable.

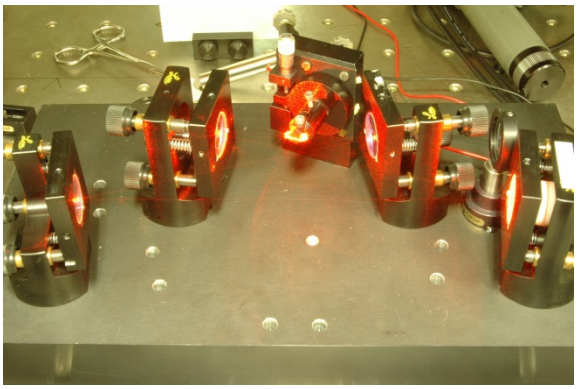

Figure 2-2: View on the frequency-doubling cavity consisted with 4 high reflecting mirrors and a LBO crystal.

Below (Figure 2-3) is a sketch of the Rayleigh-Brillouin light scattering setup at LaserLaB VU. All the components and optics are kept exactly the same as in the previous campaign [1], with only the exception of the scattering cell, which is modified for the temperature variation measurements. The laser light is divided into two branches by mirror M1. A fraction of 99% of the light is reflected toward the enhancement cavity and the scattering gas cell. A fraction of about 1% of the UV light leaks through mirror M1, and is then spatially filtered and used as a reference beam for aligning the detecting setup. The RB-scattered light is collimated and projected onto a Fabry-Perot Interferometer (FPI), which acts as the spectrometer. The scattered light is finally detected on a Photo Multiplier Tube (PMT). The modification of the gas cell will be documented in Section 3.3. Details of the enhancement cavity and FPI are described in ESA-AO5467-Final Report [1] and in [2].

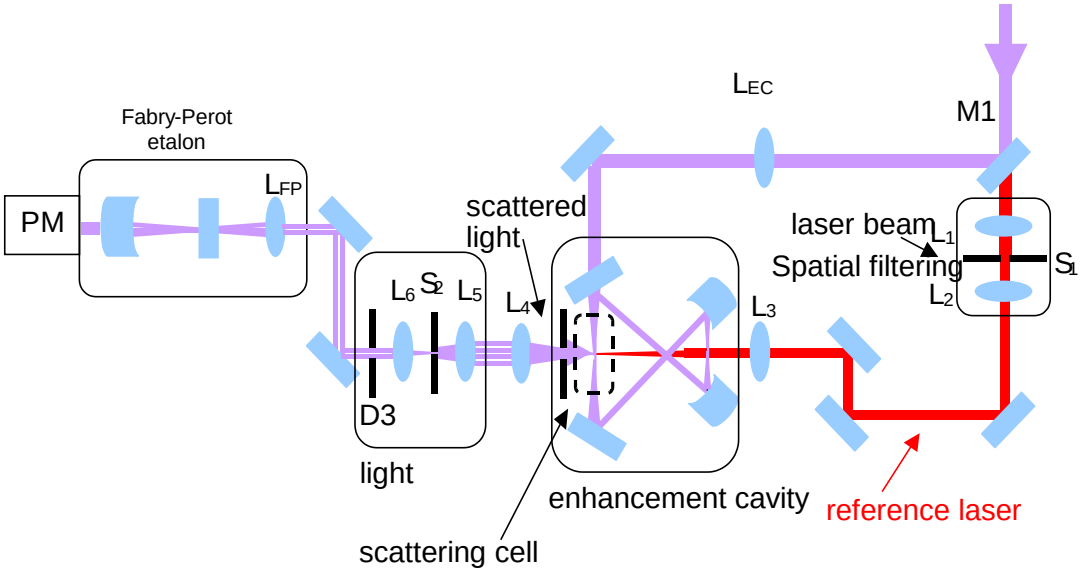

Figure 2-3: Schematic of the setup. It remains the same as previous campaign [1].

2.3 Scattering cell

The scattering gas cell used in previous activity is retained with slight modification. It has input and output Brewster angle windows for light in the 365-355 nm region to minimize reflection losses. The scattered light is transmitted through an anti-reflection coated window at 90 degree with respect to the beam pass. The cell allows for pressure variation and temperature variation. The pressure is varied by gas inlets and vacuum pumps. It is built from a solid piece of aluminum that prevents vibration problems and allows for a uniform heating and cooling of the gas.

2.3.1 Modification of scattering cell for measurement above 0 ℃

The modification of the scattering cell for temperature dependent RB scattering measurements above 0 ℃ is sketched in Figure 2-4. The temperature is varied using 4 Peltier coolers/heaters from Marlow Industries inc. (Figure 2-5) attached to a water cooling system underneath. The thermoelectric cooler can either transfer heat upwards or downwards when different signs of voltage are applied. As a function of voltage setting, the thermoelectric cooler generates a temperature difference between its two sides. While keeping the bottom of the thermoelectric cooler at 20 ℃ by the water cooling system, the temperature of the entire scattering cell, which is made of aluminum (with the thermal conductivity being 250 W/Km) can be simply adjusted by the applied voltage. It is important that an inhomogeneous temperature distribution, or a temperature gradient across the cell, is avoided. It has been experimentally verified that for a temperature setting of 65 ℃, the temperature difference between two corners of the cell, where the two resistance thermometers (Pt-100 elements) are mounted, is no more than 0.5 ℃. Hence the temperature gradient of the gas inside the cell is negligible. The thermal conductivity of the windows on the cell is 1 W/mK, which is much smaller than that of aluminum (250 W/mK), so the windows actually isolate the inside from outside. Hence the temperature gradient of the gas resulting from the windows is also negligible. It was, furthermore, discovered that it is more difficult for the thermoelectric heaters/ coolers to cool down than to heat up the cell. Therefore, with the full power applied, the cell may not be cooled to temperatures below -20 °C.

It has been tested that no water deposition occurs on the windows of the scattering cell if the temperature of the cell is above 0 ℃. Therefore, the RB scattering profile of air and N_2 can be measured from 0 ℃ up to 70 ℃ (the actual measurements were performed at a maximum temperature of 65 ℃).

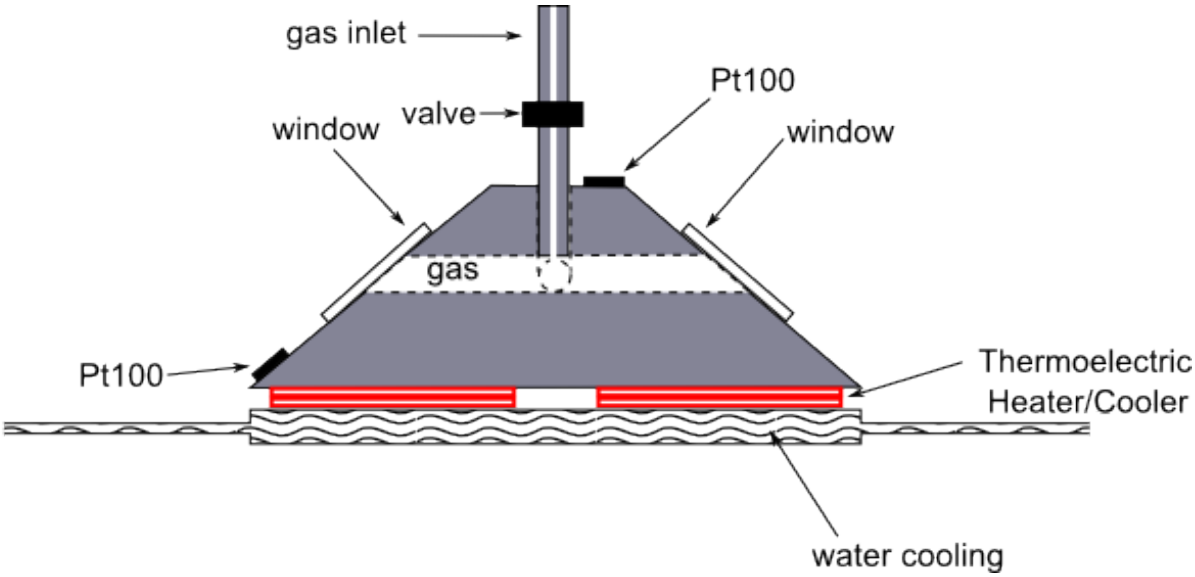

Figure 2-4: The scattering cell modified for temperature dependent measurements in the range of 0~65 ℃.

Figure 2-5: The thermoelectric heater/cooler from Marlow Industries inc.

2.3.2 Additional modification of scattering cell for measurement below 0 ℃

When the temperature is below 0 ℃, however, there is water deposition or even ice formation on the windows. This has a destructive effect on the amplification in the enhancement cavity, therewith effectively hampering the measurements. The ice on the windows can also result in additional scattering, which will finally be detected in the scattering profile.

After having tried placing a liquid-nitrogen cooled finger in the box containing the cell and flushing the windows, finally the ice deposition was prevented by flushing of dry nitrogen. Since the entire scattering cell (and the enhancement cavity) is inside a box, the entire box is flushed by N2 from an inlet at the right bottom corner (see Figure 2-6). Covering the box from the top and keeping it under steadily N2 flush, the water vapor in the

ambient air is driven out from the box, hence the ice deposition problem is solved even at the temperature as low as -20 ℃. The flush of N2 introduces turbulence in the laser beam path inside the enhancement cavity, thus resulting in additional noise of the recorded photon counts. This noise can be compensated by longer measurement and averaging. Therefore, the final averaged scattering profiles at -20 ℃ have the same quality as those measured at higher temperature (without a flush of N2). This is demonstrated in the comparison of scattering profiles in Table 4.1 and Table 4.3

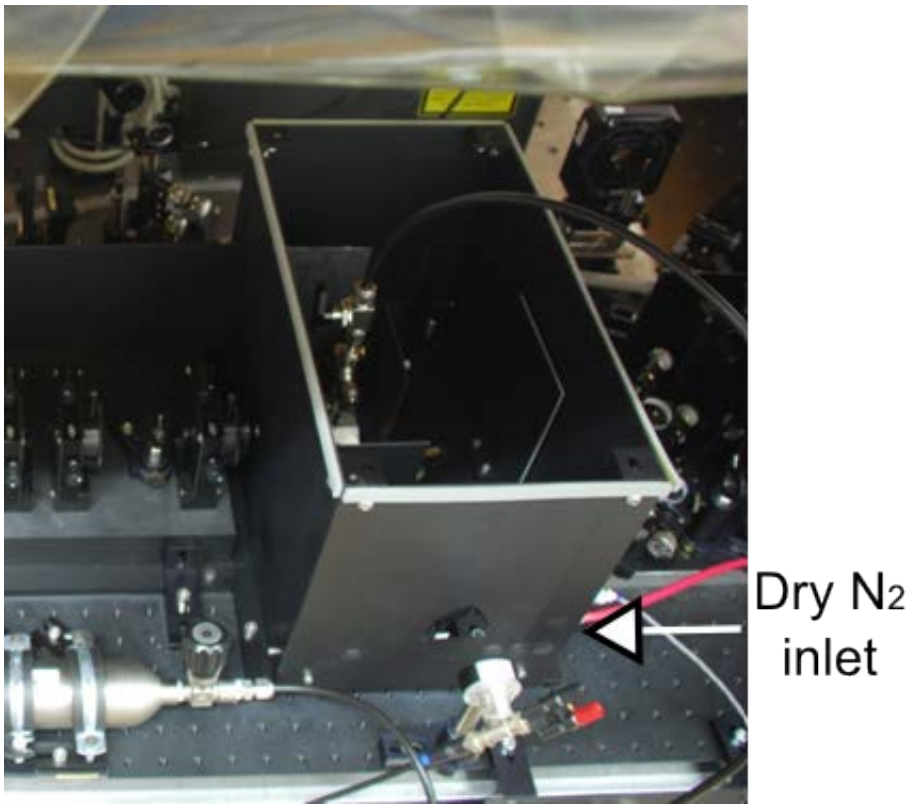

Figure 2-6: A picture of the RB scattering cell setup with the dry nitrogen flush inlet at the right bottom corner.

2.3.3 Measurement procedure for the higher and lower temperature ranges

The measurements are conducted according to the following procedure: After evacuating the cell, a gas flow will be let into the cell, at room temperature (T_1), to a certain pressure (p_1). The cell is then sealed off by closing the valve at the top of the cell and the cell is heated to the temperature T_2. By using the ideal gas law: $p_1/p_2=T_1/T_2$ after increasing the temperature, the pressure of the gas inside (p_2) can be calculated. As a result, all the parameters for the Rayleigh-Brillouin scattering measurement are known, and the measurements of the scattering profiles can be performed. It is verified that no gas leakage occurs during the measurement procedures. This is done by the measuring the pressure inside the cell shortly before and after the RB profile measurements.

2.4 Fabry-Perot Interferometer (FPI)

To verify that experimental conditions are similar as for the previous ESA project, the instrumental function and the free spectra range (FSR) of the Fabry-Perot Interferometer were measured again. This was done in a mode by keeping the applied voltage of the piezo constant and scanning the frequency of the reference laser beam, which is simultaneously measured by the wavemeter, ATOS.

2.4.1 Instrumental function

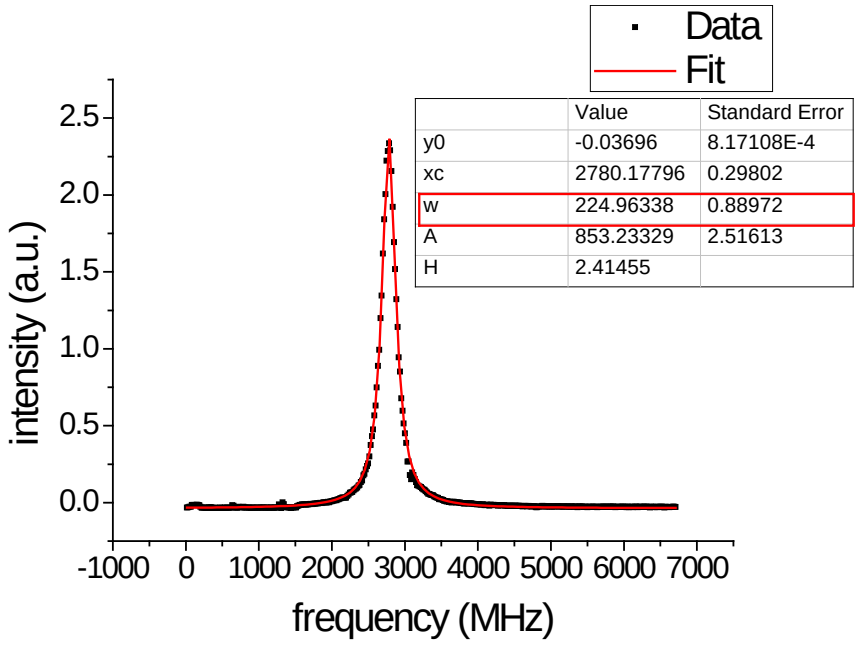

Figure 2-7: The output intensity of the FP analyzer with respect to the frequency of the laser. The instrumental linewidth is given by the FWHM of the fit, which is 224.96 ± 0.89 MHz (indicated in the legend).

The output intensity of the reference laser was plotted as a function of the measured frequency and a Lorentzian function was fitted to the data points (Figure 2-7). The instrumental function (instrumental linewidth) is determined as the width of the fit (full width half maximum), which is 224.96 ± 0.89 MHz (see Figure 2-7). It is worth noting that the measured instrument function can vary slightly due to the temperature variation of the lab. The instrument function was regularly checked by scanning the piezo in the FP-analyzer instead of the frequency of the laser.

2.4.2 FSR

The free spectral range, calibrated by measuring the frequency difference between the two main peaks, was determined at 30.5 GHz.

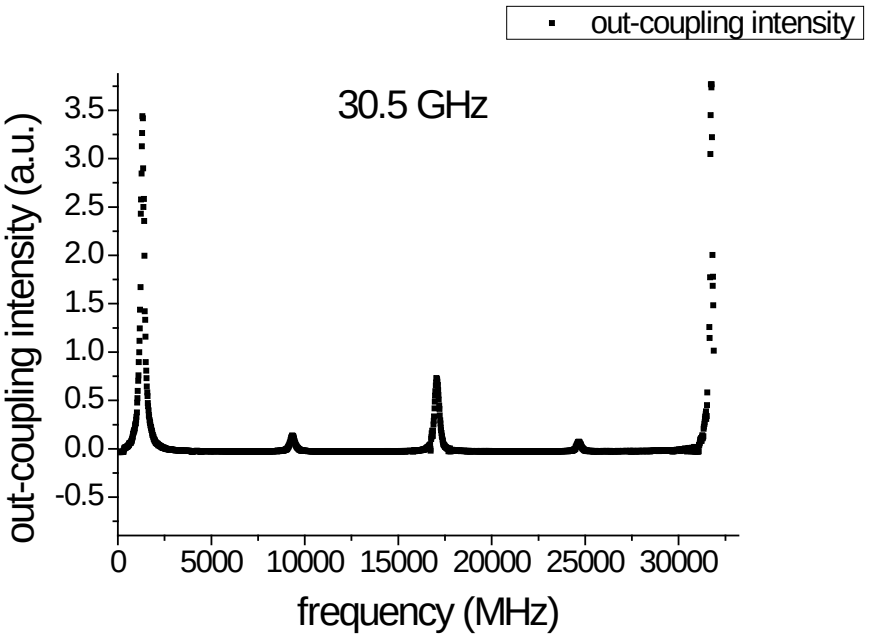

Figure 2-8: The output intensity of the FP analyzer with respect to the frequency of the laser. The free spectral range is given by the frequency difference between the two main peaks, which is 30.5 GHz.

During the previous ESA RBS activity, the measured FSR and the instrumental function were 29.76 GHz and 230 $\pm$ 10 MHz. Even though the FPI is very sensitive to the environment temperature, it can still be concluded that the FPI in the current project is operated under similar condition as the previous project, resulting in a very similar FSR.

3 Verification of the experimental set-up

3.1 Comparison with spectra measured in the previous RBS activity

3.1.1 Comparisons on air

To verify that the experimental setup is controlled at the same level as in the previous campaign, the presently acquired data of air under the same pressure conditions and room temperature are compared with those of the previous campaign. Results are shown in Table 3.1 below.

Table 3.1: Measurements of RB scattering in air at different atmospheric pressures in 2009 [1] (red dots) and in 2011 (this activity, black dots). The residuals are the different between the measurements and the modeled RB scattering line shape by the TentiS6 model.

P [bar]	scattering profiles	residuals
0.3	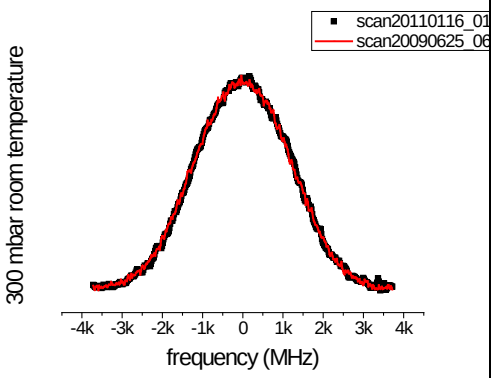	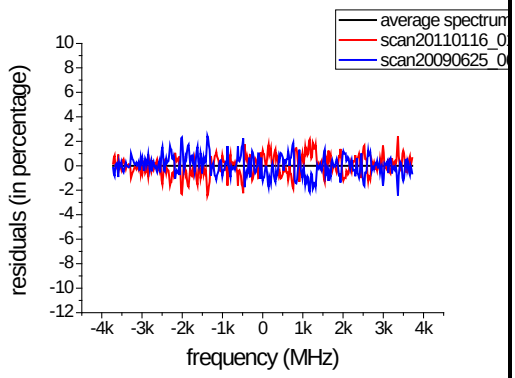
0.75	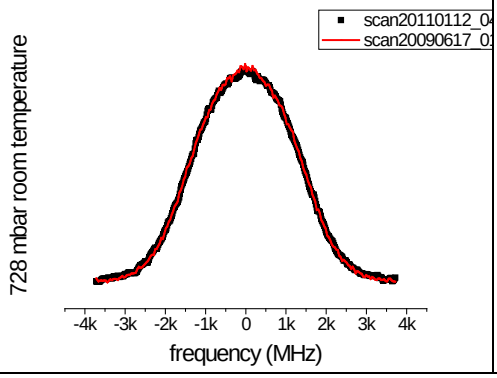	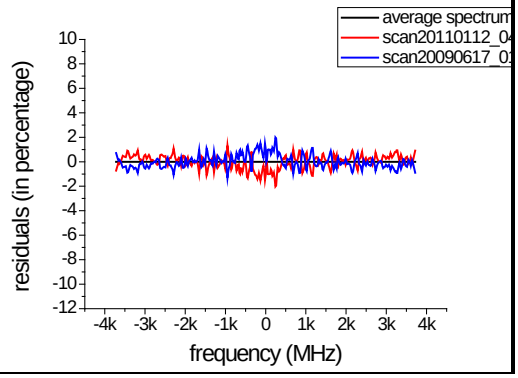

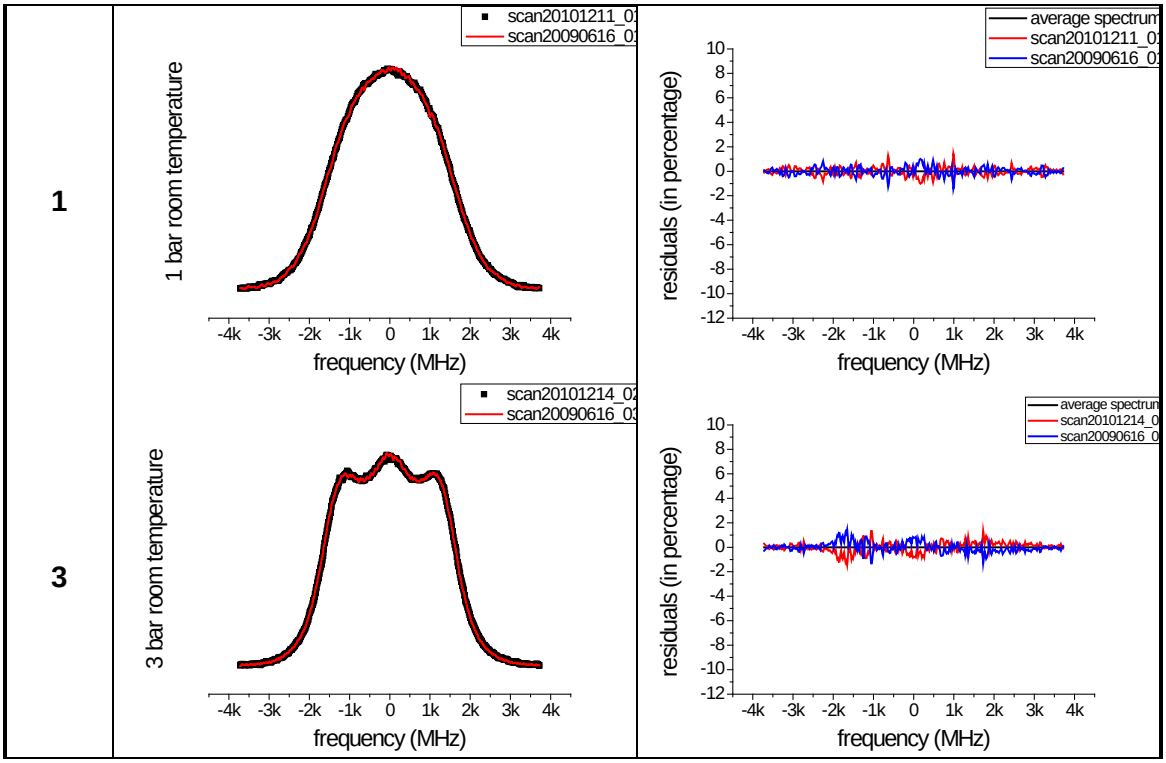

The residuals of the comparison are all at the 1% rms level, which corresponds to the noise level of the experiment. Hence, it is concluded that the experimental setup is well controlled and provides reproducible results. Also, the issue of Mie scattering from optics observed in previous RBS study seems to be more controlled now, because the windows of the cell have been replaced by new ones. During the investigations the cell windows were unmounted and cleaned every month to remove contamination and dust.

3.1.2 Comparisons on N_2

Also, the presently acquired data of N_2 at room temperature are compared with those of the previous campaign in The results of the comparisons show that the old and new measurements at the same pressure agree with each other until 2 bar. However, an increasing trend of discrepancy was found for the pressures higher than 2 bar. To investigate the discrepancy of the new measurements with those performed during the previous campaign, and to check the repeatability, N2 at 3 bar (room temperature) were measured 3 times. The first one was measured in March 2011, before the new air conditioning in the laboratory was reconstructed. The other two were performed in July 2011, but also in two different weeks, after realigning the setup. Comparison of these three measurements is shown in Figure 3-1. Since these three measured scattering profiles overlap nicely, it is concluded the repeatability of measurements in current project is within 1% level and the system is stable.
Table 3.2 below.

The results of the comparisons show that the old and new measurements at the same pressure agree with each other until 2 bar. However, an increasing trend of discrepancy was found for the pressures higher than 2 bar. To investigate the discrepancy of the new measurements with those performed during the previous campaign, and to check the repeatability, N2 at 3 bar (room temperature) were measured 3 times. The first one was measured in March 2011, before the new air conditioning in the laboratory was reconstructed. The other two were performed in July 2011, but also in two different weeks, after realigning the setup. Comparison of these three measurements is shown in Figure 3-1. Since these three measured scattering profiles overlap nicely, it is concluded the repeatability of measurements in current project is within 1% level and the system is stable.

Table 3.2: Measurements of RB scattering in N2 at different atmospheric pressures in 2009 [1] (red dots) and in 2011 (black dots). The residuals are the different between the measurements and the modeled RB scattering line shape by the Tenti S6 model.

P [bar]	scattering profiles	residuals
1.0	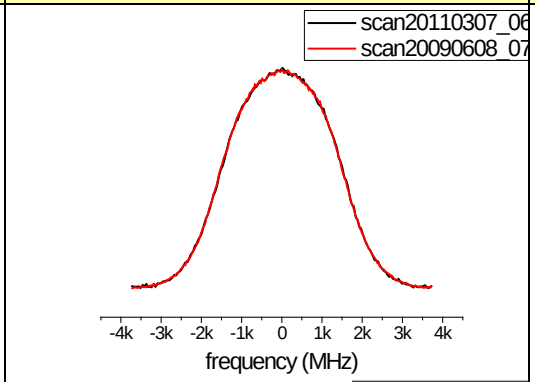	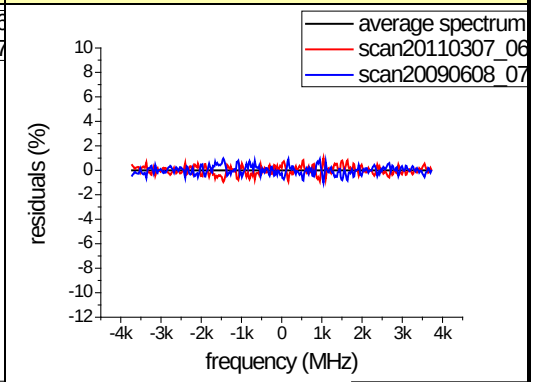
2.0	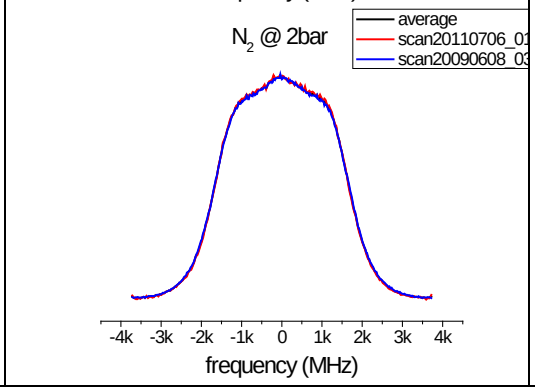	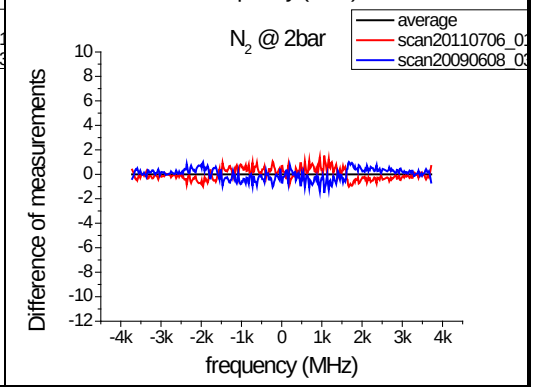

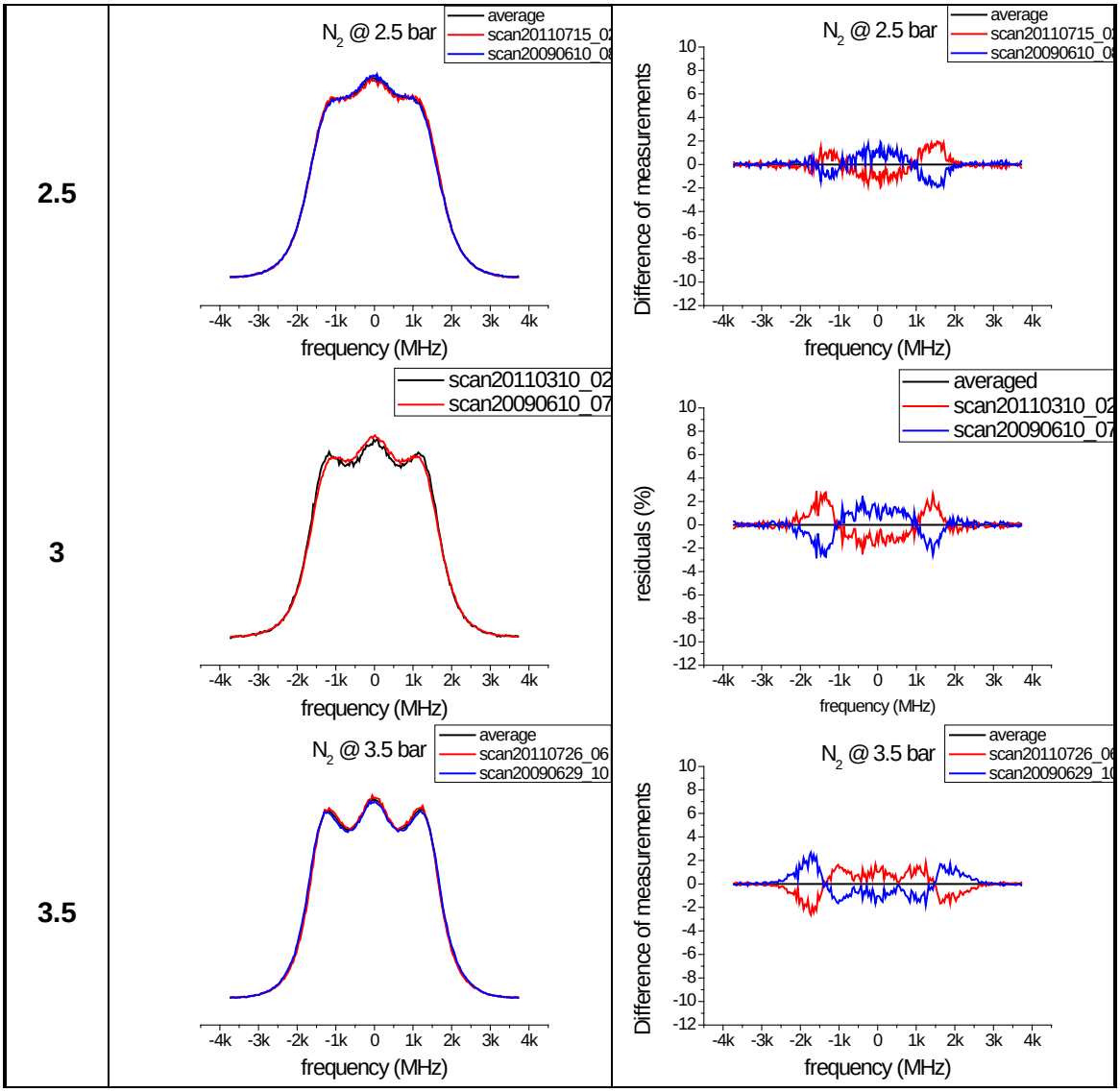
2.5
3
3.5
N2 @ 2.5 bar
average
scan20110715_02
scan20090610_08
frequency (MHz)
Difference of measurements
N2 @ 3.5 bar
scan20110726_06
scan20090629_10
scan20110310_02
scan20090610_07
averaged
residuals (%)

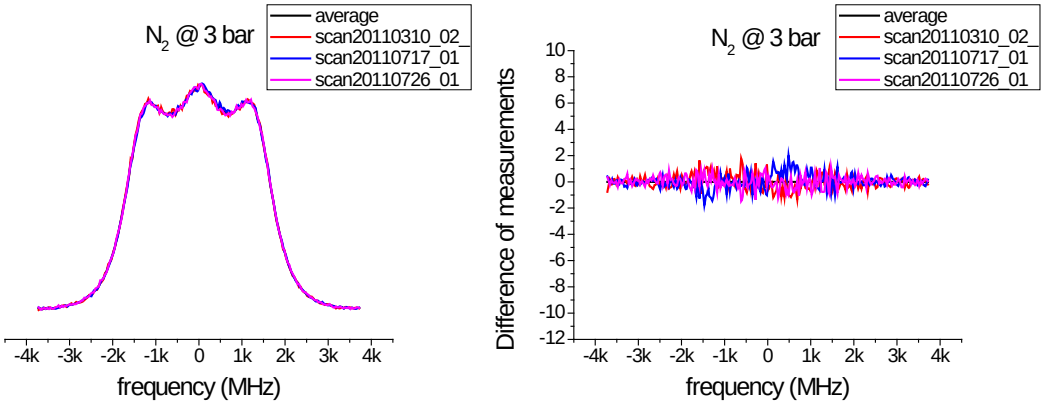
N2 @ 3 bar
average
scan20110310_02_
scan20110717_01
scan20110726_01
frequency (MHz)
Difference of measurements

(a) (b)

Figure 3-1 (a) The comparison of three measurements performed on 10-03-2011 (red), 17-07-2011(blue) and 26-07-2011(pink). (b) The residuals of these three measurements with respect to the average. The difference between these measurements is within the noise level.

3.2 Test measurements on CO_2

In order to further test the operation of the SRBS setup, and to widen the scientific scope of the project, measurements on CO_2 at different pressures and room temperature were performed. The acquired scattering profiles at the pressures indicated are shown in Table 3.3.

Table 3.3: Measured scattering profiles of CO2 (black dots) and Tenti S6 models (red line) at different pressures indicated in each figure. All these data are recorded at room temperature.

500 mbar	1000 mbar
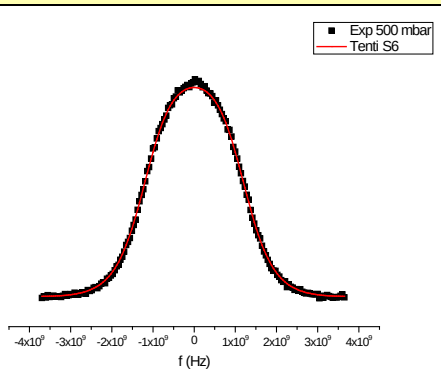	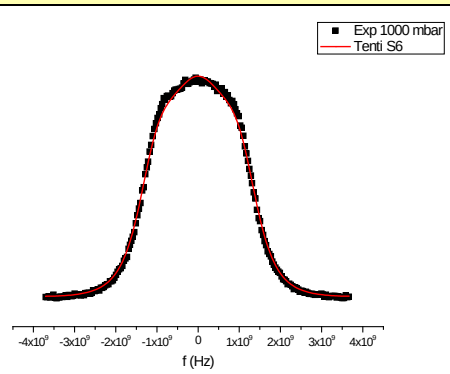
2000 mbar	**3000 mbar**
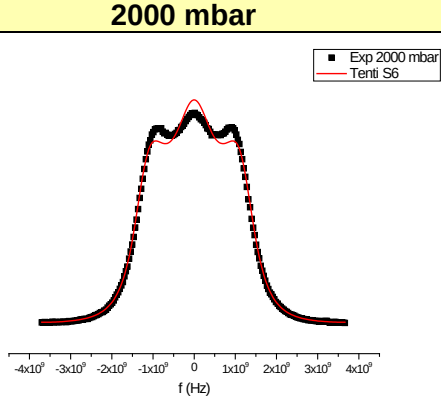	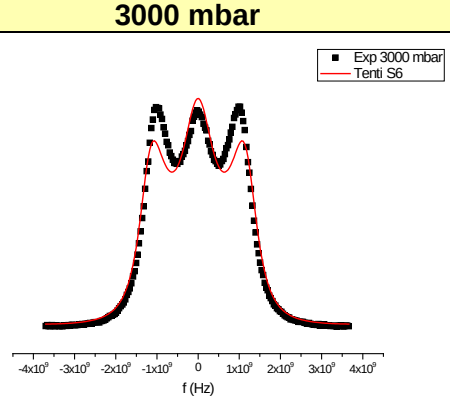

Each recorded line shape is compared with the TENTI S6 model (red line), calculated by using the RBS program with the transport coefficients delivered from the previous activity. The experimental (pressure, wavelength, temperature) and the modeling parameters (shear and bulk viscosities) are listed in Table 3.4. For conditions of pressures below 1 bar, the difference between measurements and the Tenti S6 model are small. However for higher pressures, the experimental results deviate considerably from the model.

Table 3.4: The parameters for the RB profile measurements on CO2

Pressure P (mbar)	Wavelength λ (nm)	Temperature T (k)	Bulk viscosity (Pa·s)	Shear viscosity (Pa·s)
520	366.75	297.0	1.46e-2	1.46e-5
1090	366.75	297.2	1.46e-2	1.46e-5
2010	366.75	301.2	1.46e-2	1.46e-5
2950	366.75	298.0	1.46e-2	1.46e-5

The large deviations at higher pressure were due to a wrong value of the bulk viscosity of CO_2 used in the *RBS program.* The bulk viscosity η_b, originally derived from the relaxation of the internal degrees of freedom of poly-atomic molecules in collisions, is one of the transport coefficients needed for modeling RBS profiles. This bulk viscosity parameter is, however, the least understood of all the bulk parameters, and only little is known about the numerical values [3]. One of the problems is that the bulk viscosity is essentially dependent on the frequency, and originally the value was determined from experiments at acoustic frequencies, orders of magnitude away from the frequencies of relevance for Brillouin scattering.

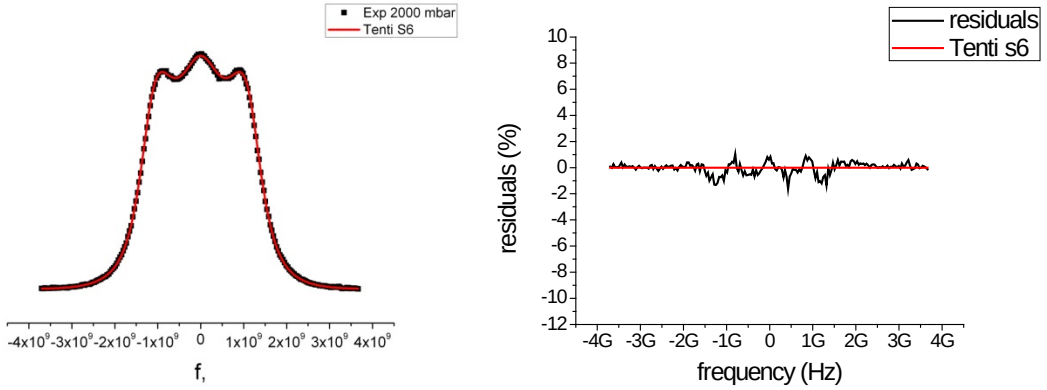

Figure 3-2 The measurement of the RB profile for CO2 at 2 bar (black), the Tenti S6 model (in red) and their deviation (right hand side) when 1.46e-6 Pa·s instead of 1.46e-2 Pa·s is used as the value for the bulk viscosity. The residuals are within 1%, which is at the level of the measurement noise.

The bulk viscosity value of CO_2 originally used in the *RBS program* was quoted from Pan *et al*. in 2004 [4], the one measured with ultrasonic waves. As the frequencies in light scattering are much larger, η_b may be considerably different for light scattering. However, one year after [4] was published it was established that in RB light scattering the value for the bulk viscosity should be in the order of 1,000 times smaller than the value derived from acoustic measurements. This paper by Pan *et al*. in 2005 [5] was already reviewed during the previous RBS activity, but since CO_2 was not investigated, the values for CO_2 had not been updated in the *RBS program*. If 1.46e-6 Pa·s is assumed, the calculated spectra and our measurement match perfectly, as demonstrated in Figure 3-2.

So far, all experimental information about η_b of every gas derives from measurements involving ultrasonic frequencies. As in light scattering experiments the sound frequencies are at least 2 orders of magnitude larger than in acoustic experiments, the currently known values of η_b may not be reliable for modeling SRB-experiments, as is shown here for the example of CO_2. Hence, the current RB-scattering experiments may be used to deduce the bulk viscosity, one of the relevant macroscopic transport coefficients of a gas. The bulk viscosity value could be inferred by optimizing the Tenti S6 fit to the measured spectrum as it was done in the previous RBS study.

4 Results: RB scattering at different temperatures

After the preceding test measurements Rayleigh-Brillouin scattering profiles were determined for both air and N_2 at various pressures and temperatures. The temperature was measured by two PT-100 temperature sensors, mounted on different corners of the scattering cell. For temperatures as high as 65 °C, these two sensors indicate a less than 0.5 °C difference. The temperature difference at the beginning and the end of each measurement is also measured to be less than 0.5 °C. The pressure of the gas inside the cell was measured by a pressure meter and then (if the temperature was changed after sealing the cell) calculated according to the ideal gas law. Tables containing all the measurement-model deviations are presented below.

4.1 Experimental data on air

Measurements for Air at a range of temperatures from -20 °C to 65 °C at various pressures have been performed. All the acquired scattering profiles and the corresponding calculated Tenti S6 model spectra are shown in Table 4.1.

Table 4.1: Measured scattering profiles and Tenti S6 models, for measurements of air performed at different pressures and high temperatures.

T [℃]	0.3 bar	0.75 bar	1.0 bar	3.0 bar
-20	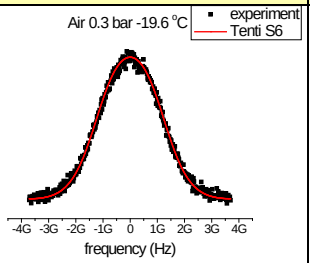	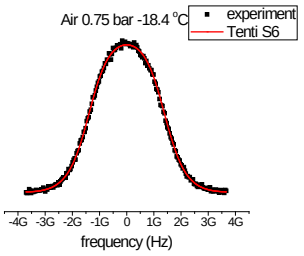	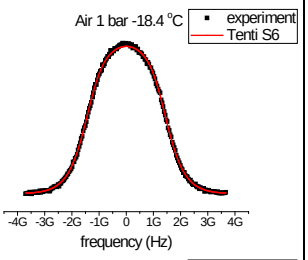	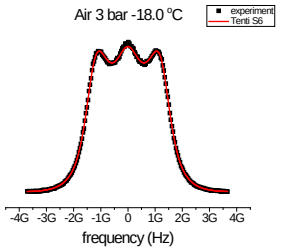
4	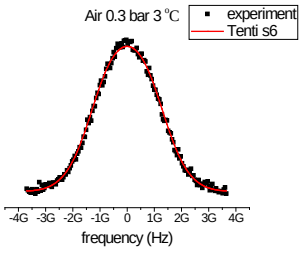	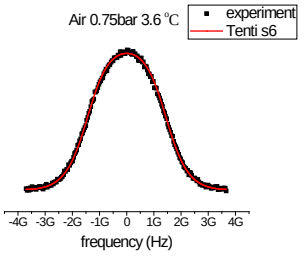	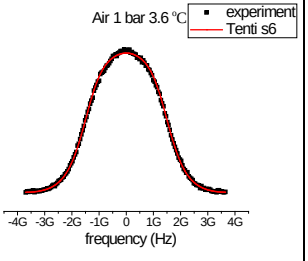	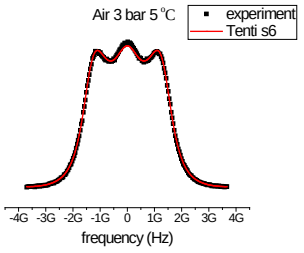
24	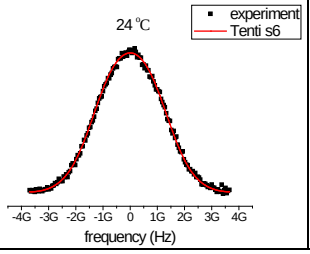	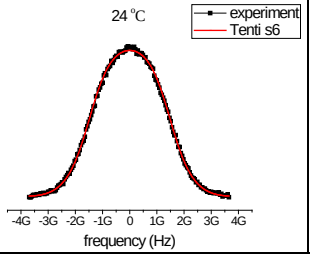	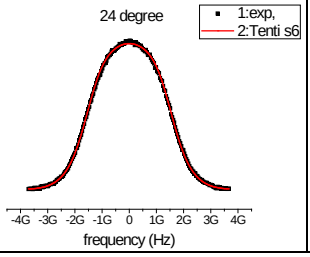	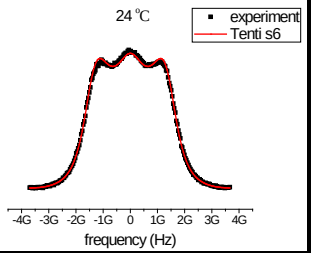

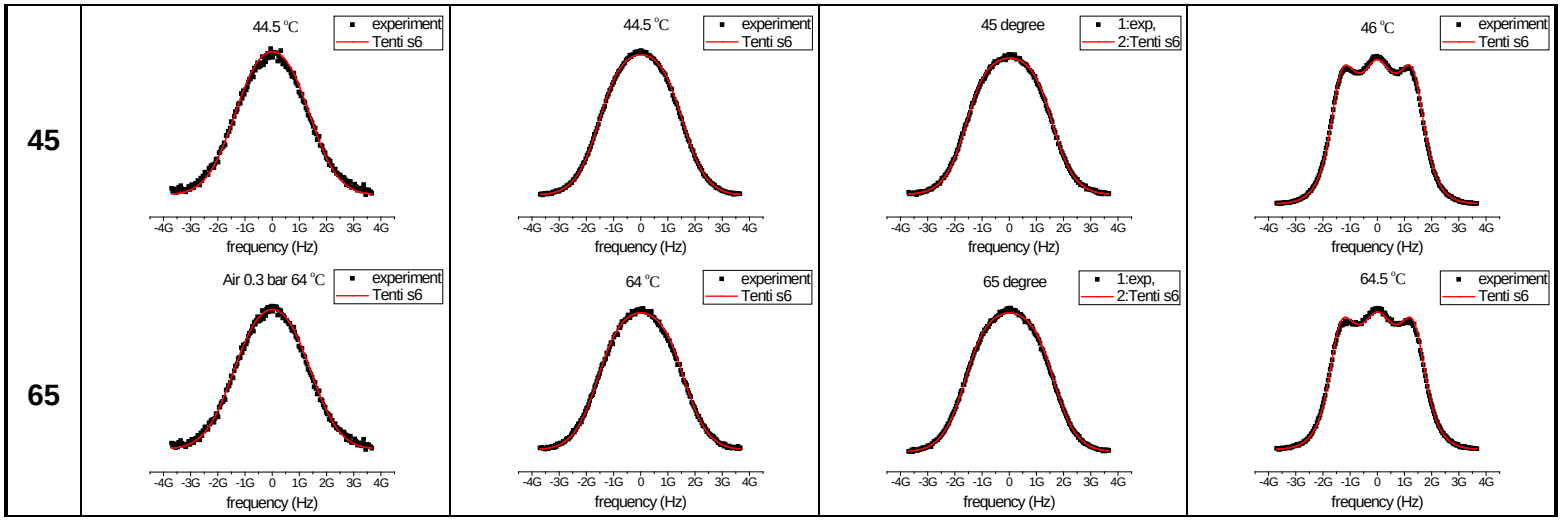

Table 4.2 summarizes the parameters used for the Tenti S6 model calculations. Bulk viscosity, shear viscosity and thermal conductivity depend on temperature but not on pressure.

Table 4.2: The parameters of the experimental conditions and the values for the transport coefficients for Air, used for modeling RB-scattering and given directly by the output files of the RBS Program.

Original P (mbar)	Calculated P (mbar)	Wavelength λ (nm)	Temperature T (k)	Bulk viscosity (Pa·s)	Shear viscosity (Pa·s)	Thermal conductivity W/(m·K)
300	256	366.84	253.5	0.970e-5	1.617e-5	2.254e-2
300	287	366.84	276.0	1.038e-5	1.730e-5	2.435e-2
300	300	366.65	297.2	1.100e-5	1.833e-5	2.602e-2
300	320	366.65	318.7	1.160e-5	1.933e-5	2.768e-2
300	340	366.65	337.0	1.210e-5	2.016e-5	2.906e-2
750	643	366.84	254.8	0.974e-5	1.624e-5	2.265e-2
750	703	366.84	276.7	1.040e-5	1.734e-5	2.441e-2
726	726	366.65	297.0	1.099e-5	1.832e-5	2.601e-2
726	776	366.65	317.7	1.157e-5	1.928e-5	2.760e-2
728	826	366.65	337.2	1.210e-5	2.017e-5	2.908e-2
1000	858	366.84	254.8	0.974e-5	1.624e-5	2.265e-2
1030	1030	366.65	297.0	1.099e-5	1.832e-5	2.601e-2
1010	1010	366.65	318.2	1.159e-5	1.931e-5	2.764e-2
1020	1020	366.65	338.6	1.214e-5	2.023e-5	2.918e-2
3000	2569	366.84	254.3	0.973e-5	1.621e-5	2.261e-2
3000	2813	366.84	278.0	1.044e-5	1.740e-5	2.451e-2
2910	2910	366.65	297.2	1.100e-5	1.833e-5	2.602e-2
2910	3130	366.65	319.2	1.161e-5	1.935e-5	2.772e-2
2910	3310	366.65	338.2	1.213e-5	2.021e-5	2.915e-2

The deviation of each measurement with respect to the model at the same condition is shown in Table 4.3. The deviations are within ±2% for all the measurements, whilst the noise level for the lowest pressure (0.3 bar) is a little higher than the others.

Table 4.3: Deviations model-measurement in percentage of the maximum signal of the model, for measurements of air performed at different pressures and high temperatures.

T [℃]	0.3 bar	0.75 bar	1.0 bar	3.0 bar
-20	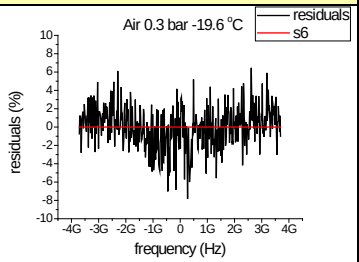	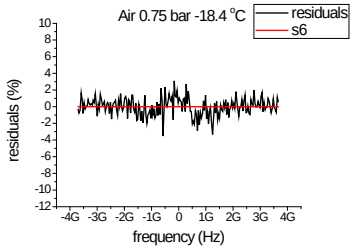	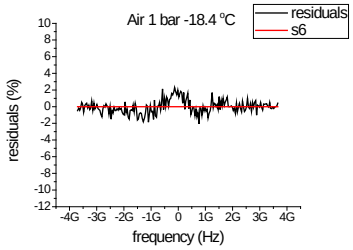	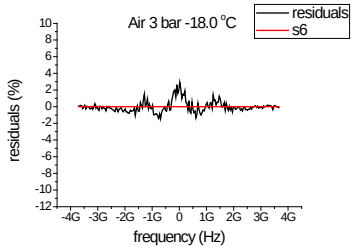
4	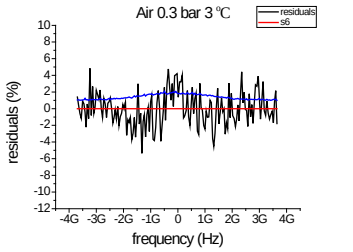	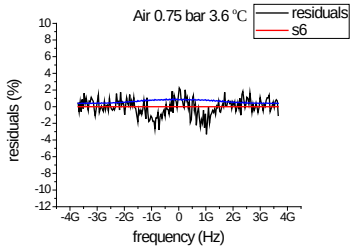	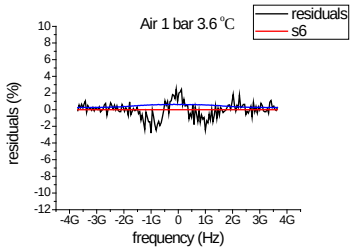	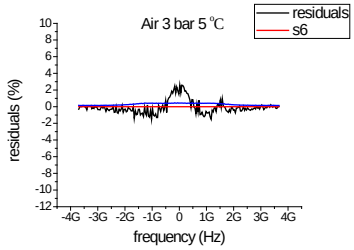
24	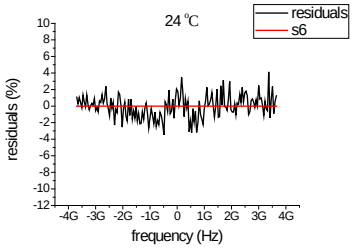	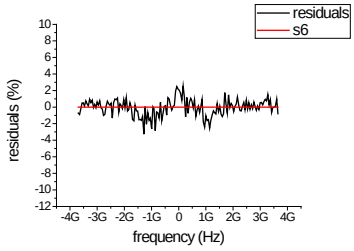	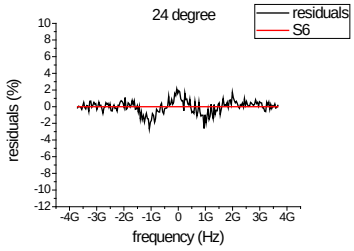	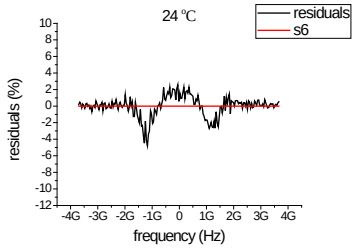
45	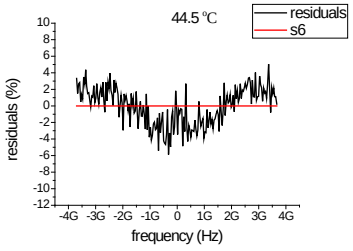	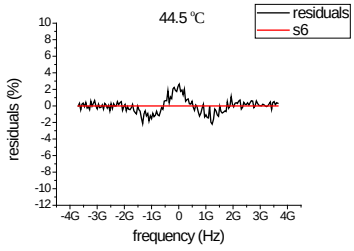	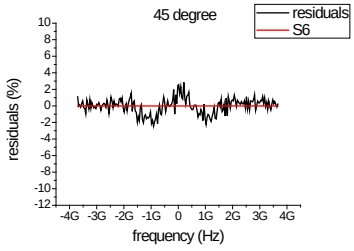	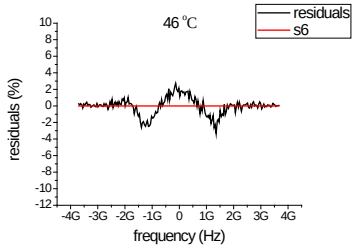
65	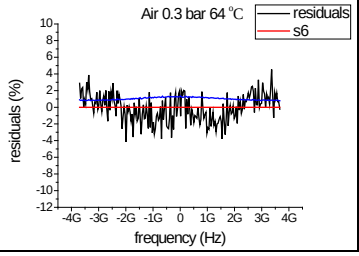	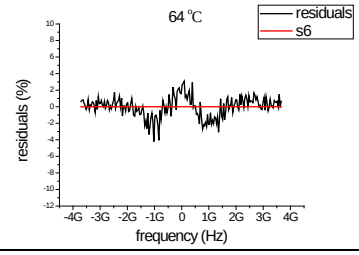	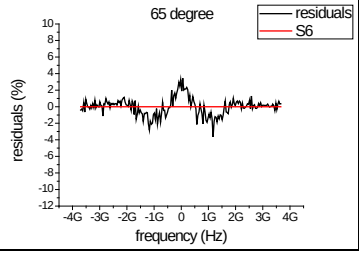	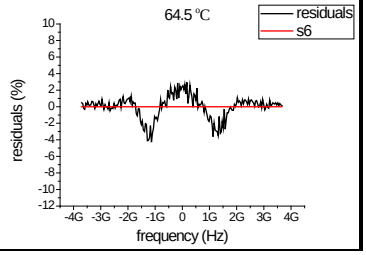

4.2 Temperature dependent trends for Air

The temperature dependence of the measured scattering profiles of air at 1 bar and 3 bar is shown in Figure 4-1 and
Figure 4-2. According to Figure 4-1 (b), the scattering profiles have 10% difference for a 80 K temperature range even at 1 bar. For 3 bar, the difference increases to 17%. The Brillouin peaks shift more from line center at higher temperatures, which is illustrated in Figure 4-2. Therefore, the profile is wider at high temperature than at low temperature. All scattering profiles are normalized to unit area.

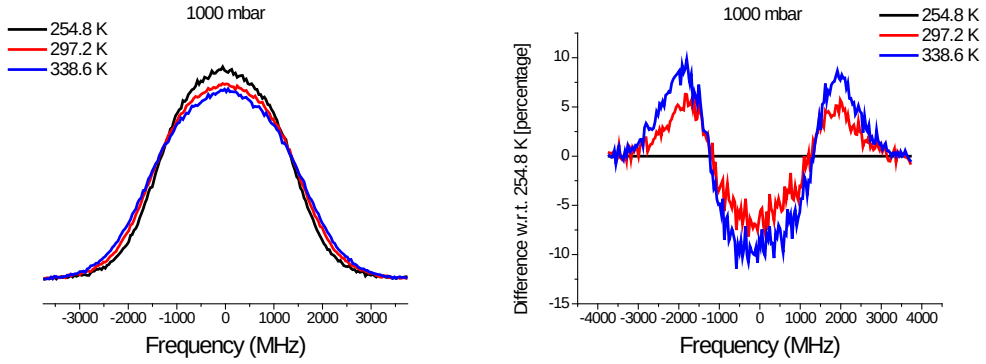

Figure 4-1 The comparison of the measured scattering profiles of 1 bar air at different temperatures. It shows a broadening trend as the temperature increases.

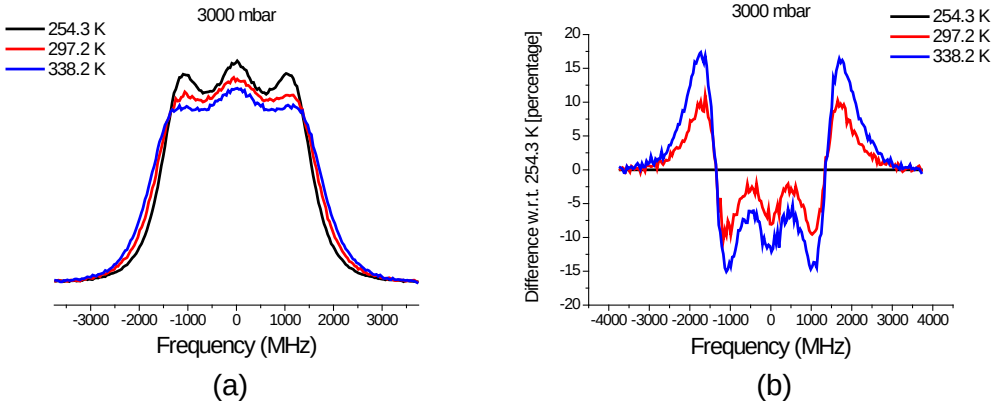

Figure 4-2 The comparison of the measured profiles of 3 bar air at different temperatures. It shows a broadening trend as the temperature increases. It is also noticeable that the Brillouin peaks shift more from the center at higher temperature, which agrees with the theory.

4.3 Experimental data on N_2

Scattering profiles of N_2 at a range of temperatures from around -20 °C to 65 °C at 1 bar and 3 bar have been recorded. The results and the corresponding Tenti S6 model spectra are shown in Table 4.4. The residuals of the measured profiles with respect to the models are shown in Table 4.5.

Table 4.4: Measured scattering profiles and Tenti S6 models, for measurements of N_2 performed at different pressures and different temperatures.

T [℃]	1 bar	3 bar
-20	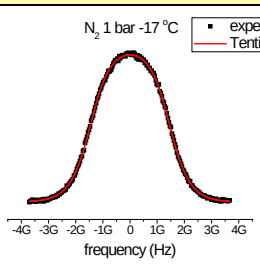	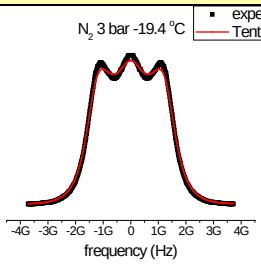
4	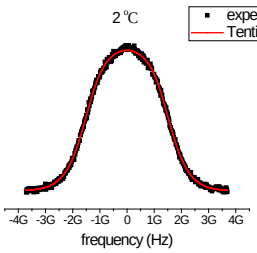	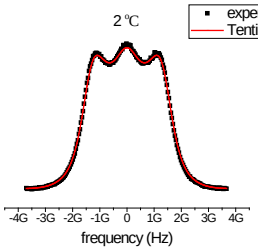
24	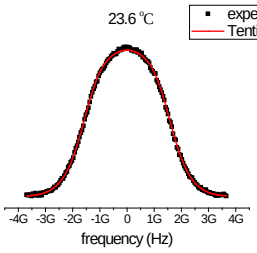	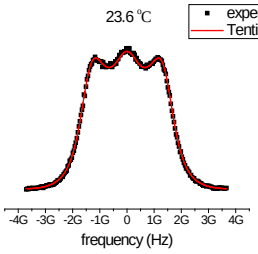
65	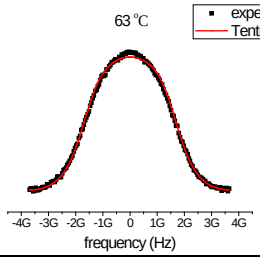	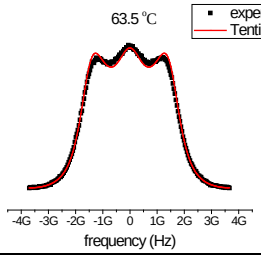

Table 4.5: Deviations model-measurement in percentage of the maximum signal of the model, for measurements of N_2 performed at different pressures and temperatures.

T [℃]	1 bar	3 bar
-20	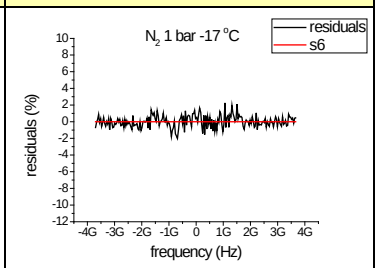	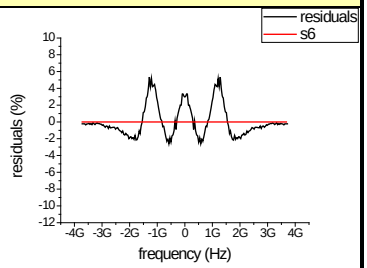
4	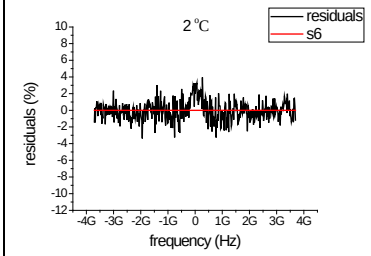	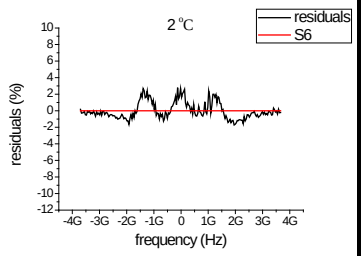
24	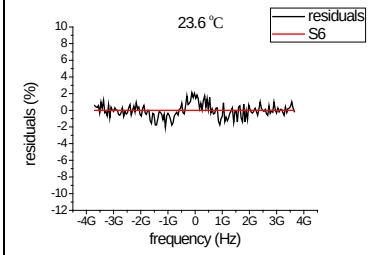	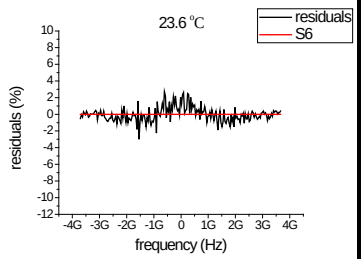
65	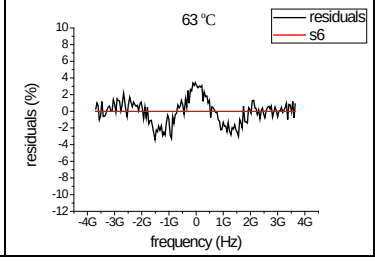	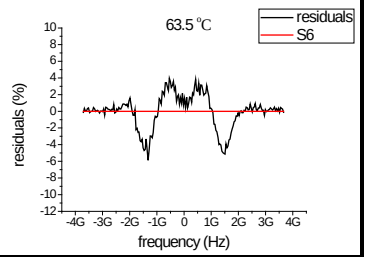

The relatively large discrepancy between the measured scattering profiles and the calculated ones is caused by an improper treatment of the bulk viscosity, shear viscosity and thermal conductivity at the corresponding temperature by the *RBS program*. The temperature dependence of the gas transport coefficients has to be built into the model (Tenti-model and RBS-code) to provide an updated description of the scattering profiles. This analysis is covered in Part III.

Table 4.6: The parameters of the experimental conditions and the values for the transport coefficients for N_2 used for modeling RB-scattering. The transport coefficients are always the same for different pressures and/or temperatures.

Original P (mbar)	Calculated P (mbar)	Wavelength λ (nm)	Temperature T (k)	Bulk viscosity (Pa·s)	Shear viscosity (Pa·s)	Thermal conductivity (W/m·K)
1000	862	366.84	256.0	1.290e-5	1.763e-5	2.520e-2
1000	287	366.84	276.0	1.290e-5	1.763e-5	2.520e-2
1001	1001	366.84	295.0	1.290e-5	1.763e-5	2.520e-2
1000	320	366.65	318.7	1.290e-5	1.763e-5	2.520e-2
3000	2563	366.84	254.7	1.290e-5	1.763e-5	2.520e-2
3000	2784	366.65	275.2	1.290e-5	1.763e-5	2.520e-2
3000	3000	366.65	296.7	1.290e-5	1.763e-5	2.520e-2
3000	3400	366.65	336.6	1.290e-5	1.763e-5	2.520e-2

4.4 Temperature dependent trends for N_2

Although the RBS program does not provide good calculations, the measured scattering profiles for N_2 at different pressures and temperatures still show a similar trend, as illustrated in Figure 4-3 and Figure 4-4.

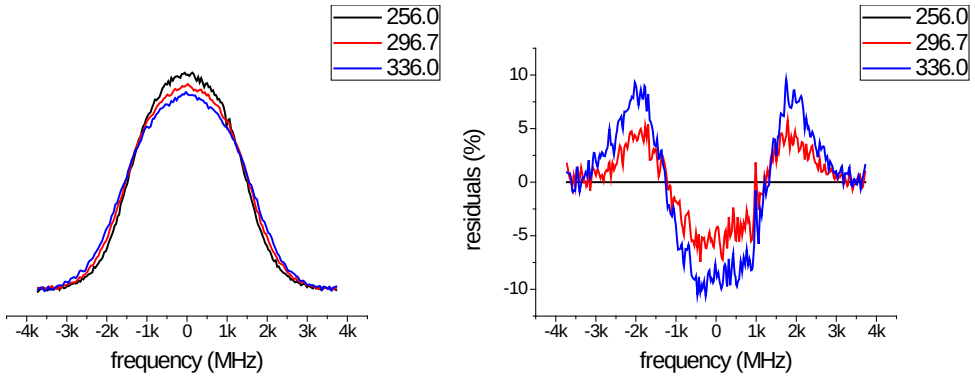

Figure 4-3 The comparison of the measured scattering profiles of 1 bar N2 at different temperatures. It also shows a broadening trend as the temperature increases.

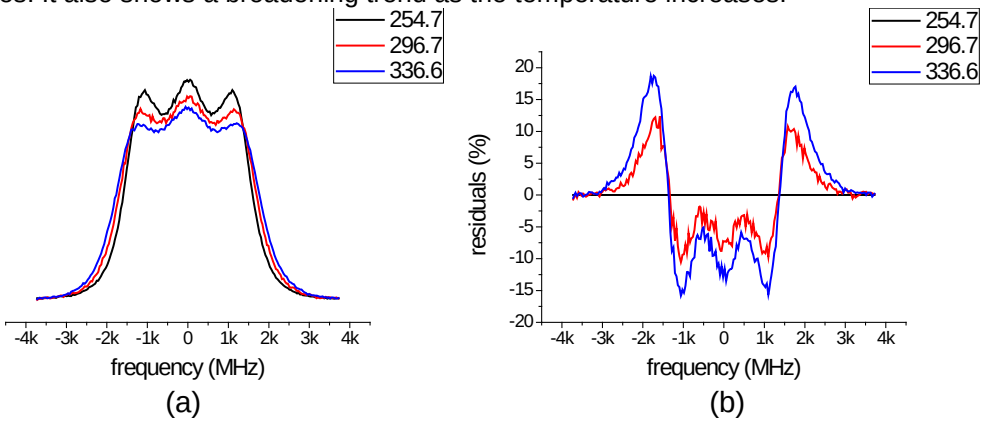

Figure 4-4 The comparison of the measured profiles of 3 bar N2 at different temperatures. The result is similar to that showed in

Figure 4-2.

5 Conclusion of Part I

The first objective of this part was to verify the experimental set-up by comparison of measurements of air and N_2 at room temperature and at 4 pressures with measurements performed during the previous activities. The repeatability of the measurements was within the measurement noise, and the set-up was further optimized to allow for less noisy measurements.
The second objective was to measure the temperature dependency of Rayleigh-Brillouin scattering at the same 4 pressure levels, in order to extend the applicability of the Tenti S6 model. The deviations of the measurements from the Tenti S6 model spectra calculated by the *RBS program* are within 3% for Air at all pressures and temperatures. The measurement noise is proportional to the square root of the detected photon counts per second + the additional electronic noise. For all the measurements the noise is ~ 1%. Therefore, the temperature dependency of the Rayleigh-Brillouin scattering is well described by the Tenti S6 model with a ~ 2% deviation from the measurements from this activity. The discrepancy between the measured and modeled spectra for N_2 should be solved by invoking updated values for temperature-dependent transport coefficients in the Tenti-model and the *RBS Program*. This will be discussed in Chapter 11.

Part II

6 Laser source of longer wavelength

In order to expand the parameter space for testing the Tenti S6 model, measurements at a wavelength significantly deviating from the chosen value of 366 nm need to be carried out. Because the Brillouin side band features become more *pronounced* at longer wavelengths, this domain is preferred for additional tests of the Tenti model, since it provides a more sensitive test ground for validating the Tenti S6 model.

6.1 Two possible choices

We considered two options:

1) A fixed-wavelength laser source at 532 nm

At this wavelength, a narrowband VERDI laser can be used delivering up to 10 Watts at a bandwidth of ~1 MHz. This opens up the opportunity of carrying out the RB-scattering measurements without the frequency-doubling and enhancement cavities, giving more flexibility in choosing scattering angles. A second marked advantage of performing RB-scattering experiments without the need for an enhancement cavity is that strict constraints on equipping the scattering cell with exact Brewster-angled windows for the chosen wavelength can be relaxed. In extra-cavity operation, small additional losses due to non-exact Brewster aligning of the entrance and exit windows of the scattering cell are permissible. The specific value of 532 nm is also of scientific importance: many LIDAR applications are performed at this specific wavelength, due to the wide availability of Q-switched Nd:YAG laser systems running at 1064 and 532 nm. At LaserLAB a VERDI-V10 is available (see Figure 6-1).

One of the possible drawbacks of the VERDI system is that its single-mode frequency may be subject to drift. Depending on the exact choice of the finesse and bandwidth of the Fabry-Perot analyzer the drift of the VERDI excitation laser adds to the instrument width, and that may influence the resolution of the detection setup and therefore the measured line shape of Rayleigh-Brillouin (RB) scattering. Therefore an assessment of the drift of the VERDI laser needs to be done before deciding to make it the light source of choice for this project.

Figure 6-1: Continuous wave narrowband VERDI laser delivering up to 10 Watts of output power at a bandwidth of 1 MHz at 532 nm. Temperature control of the solid base-plate on which the laser is mounted can be used to regulate the drift of the output frequency.

2) A wavelength-tuneable laser near 400 nm

This option will be followed if the problems regarding the drift of the VERDI-V10 laser are prohibitive. Radiation in the range 400-430 nm can be obtained via second harmonic generation (frequency-doubling) of the output of the continuous-wave Titanium-Sapphire laser system, which was also used for the measurements at 366 nm. Since the gain of the laser is higher near 800-850 nm than that at 733 nm, blue radiation at the level > 1 Watt can be produced with this system, as was demonstrated in our laboratory. It is noted that the frequency-doubled Ti-Sa laser has a bandwidth of only 1 MHz with negligible drift during measurement periods of ~1 hour. This is a clear advantage.

6.2 The assessment of the VERDI laser

To verify if the drift of the wavelength from VERDI laser is sufficiently small to be implemented in a RB scattering study, it was experimentally determined using a commercial ATOS wavelength meter. It is verified that immediately after being switched on and turned to the designated power, the frequency of the VERDI laser drifts as much as 100 MHz over a time interval of 15 minutes, indicated in Figure 6-2. However, when the laser power has been kept as constant for a warm-up period (typically 1 hour), the laser frequency will be stable afterwards. Figure 6-3 is a measurement after the warm-up period, which demonstrates that the laser frequency changes less than $\pm$20 MHz in 1 hour. For comparison, the Ti:Sa laser has a frequency drift of 18 MHz/h as shown in Figure 6-4. The ATOS wave meter itself exhibits a drift in the order of 10 MHz/h, so it is possible that the actual drift of the both two lasers are even smaller.

In conclusion, based on the outcome of the tests, the VERDI laser is as stable as the Ti:Sa laser, hence good enough for performing Rayleigh-Brillouin scattering experiments.

At the time it was concluded to focus on additional RB scattering measurements at wavelengths near 400 nm. In hindsight a choice to focus on use of a VERDI laser at 532 nm would have been even better defendable.

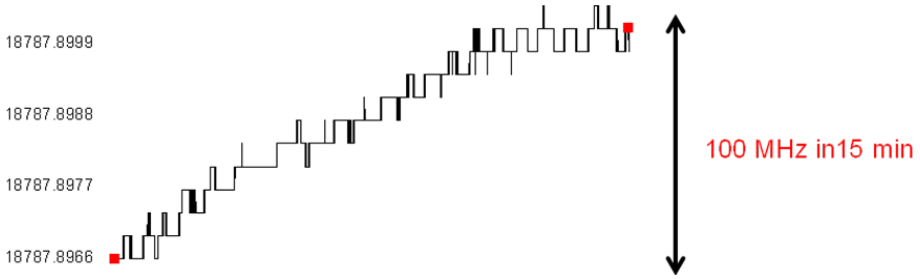

Figure 6-2: The drift of the wavelength of VERDI laser in the first hour after being switched on. The vertical axis (on the left) is in the unit of wave number (1 wave number is equal to 30 GHz).

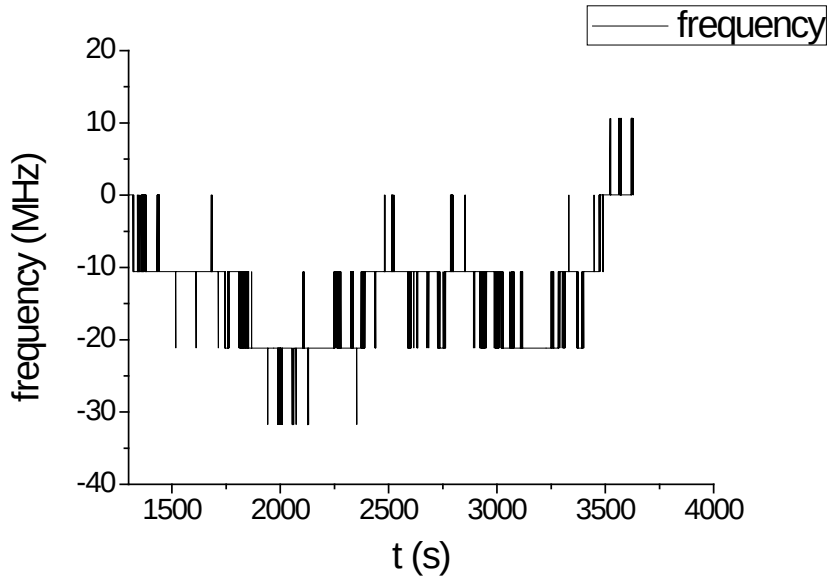

Figure 6-3: The frequency drift of the VERDI laser after 1 hour warming up.

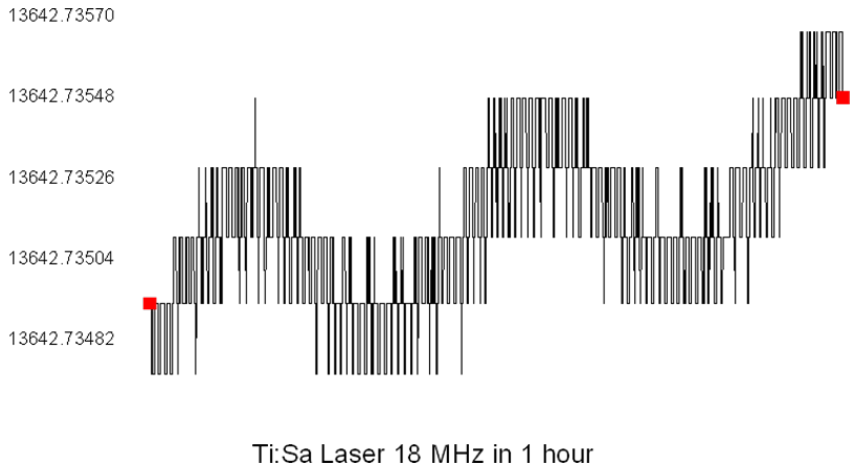

Figure 6-4: The drift of the wavelength of Ti:Sa laser measured by a commercial ATOS wavelength meter, which is known to drift itself by (less than) 10 MHz/hour. The vertical axis (on the left) is in the unit of wave number.

7 Experimental Setup

A choice was made to extend the range of the frequency-doubled Ti:Sa laser to longer wavelengths of approximately 400 nm for the case of right angle (90 degrees) scattering measurements.

7.1 Setup for scattering at 403/407 nm and 90° scattering angle

For the choice of the Ti:Sa laser as the light source for RB-measurements at longer wavelengths, a frequency-doubling cavity is needed to produce blue light. Moreover, an enhancement cavity is also needed to ensure sufficient intensity of the scattered radiation. As for the wavelength, a choice is made to operate the experiment at 403 nm. This is ruled by the operation optimum of the Ti:Sa laser, and the available mirrors to build the frequency-doubling cavity and the enhancement cavity. For the 403 nm operating wavelength, the initially-built frequency-doubling cavity, the enhancement cavity, and the Fabry-Perot Interferometer (FPI) are not suitable (because designed for 366 nm). An LBO crystal, for doubling the frequency from 806 nm to 403 nm also needs to be purchased.

Initially a choice was made for RBS measurements at 407 nm. However after the mirrors were purchased it turned out that their optimum resided at 403 nm. For this reason in this chapter values of both 403 and 407 nm appear. The final RB-measurements are carried out at 403 nm.

7.1.1 Construction of the frequency-doubling cavity

The layout of the frequency-doubling cavity to generate 403 nm light is the same as that for 366 nm. However, all mirrors need to be changed due to the alternate choice of wavelength. In order to obtain a high output power, three requirements need to be fulfilled; (1) the finesse of the cavity needs to be as high as possible, (2) the cavity needs to be impedance matched and (3) phase-matching in the LBO crystal for doubling the 806 nm output must be optimised. To achieve a high finesse, the reflectivity of the mirrors must be as high as possible. Therefore, the reflectivity of the 3 mirrors of the cavity is chosen to be 99.9% (at 806 nm). Thus, the losses due to the transmission of these 3 mirrors are ~0.03 % (1- 0.999^3). Additionally, due to the scattering loss on the mirror coatings and the reflection losses on the LBO crystal surfaces, the total round-trip loss is estimated to be 1%. Therefore, to achieve the impedance matching condition, which requires that the transmittance of the in-coupling mirror is exactly the same as the round trip losses of the laser beam inside the cavity, the reflectivity of the in-coupling mirror is chosen to be 99% at 806 nm. To fulfil the phase-matching requirement an LBO crystal, cut for a phase-matching angle of 30.2° (with respect to the optical axis - the polarization of the fundamental light and the second harmonic generated light are perpendicular to each other) was purchased from Fuzhou Caston Optronics Co.,Ltd, the same manufacturer of the LBO crystal used for 366 nm. In addition, to minimize the reflection losses on the crystal surfaces, the surfaces are also cut to have Brewster angle for 806 nm light.

With the chosen reflectivity of the mirrors and the chosen angle cut for the LBO crystal, the maximal obtained power of the 403 nm is 600 mW, when an input power of 1.6 W is used at fundamental wavelength.

7.1.2 The enhancement cavity

The layout of the enhancement cavity to effectively amplify the power of 403 nm light for scattering is also the same as that for 366 nm. Mirrors with proper coatings for 403 nm instead of 366 nm need to be installed. Switching from 366 nm to 403 nm, one may worry about the Brewster angles for the cell windows will vary significantly, requiring a re-built of the scattering cell. It will be shown below that this effect is only minor.

The equation for the Brewster angle is written as:

$$\theta_B = \arctan(\frac{n_2}{n_1})$$

where n_1 and n_2 represent the refractive index of the two media. In our case n_1 is almost equal to 1 and a constant since the medium is air. n_2 is the refractive index of the windows (fused silica), and it changes with respect to the wavelength of the incident light. n_2= 1.4744 and 1.4696 for wavelengths of 366 nm and 405 nm, respectively. Therefore the calculated Brewster angle is 55.8532° at 366 nm and 55.7664° at 405 nm. So there is only 0.09° difference. Figure 7-1 illustrates the reflectance of two laser beams (with different polarizations) with respect to the incident angle. From this figure we can conclude that the reflectance stays almost the same from 50° to 60°. Therefore, the 0.32° difference, which results from the change of the wavelength, only has a marginal influence. It wastherefore concluded that there is no need to rebuild the scattering cell for an updated Brewster angle.

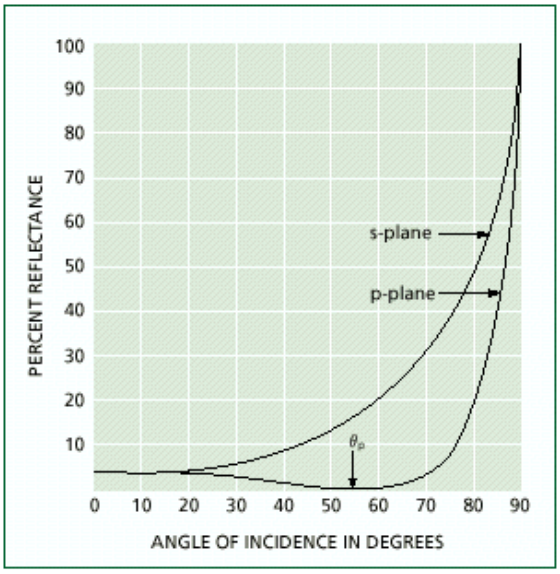

Figure 7-1 The reflectance of a laser beam with two different polarizations with respect to the incident angle. The Brewster angle of the RBS experiment is indicated by θ_B.

7.1.3 Fabry-Perot Interferometer

Since the wavelength is changed, a specific Fabry-Perot Interferometer (referred as FPI afterwards) also must be designed and built. A specially coated batch of mirrors was purchased to build the FPI (Laser-Optik GmbH). In the design of the FPI three important parameters must be defined: the Free Spectral Range (FSR), the in-coupling efficiency, and the finesse. The choices to be made on the optics parameters entail several compromises to be made for the reflectivities *R* and the radii of curvature *r* of the mirrors to be purchased.

7.1.3.1 Free Spectral Range

Figure 7-2 displays a schematic of the FPI used in the RB-measurements at 366 nm. It consists of two mirrors: one plane mirror with a reflectivity *R*=98% at 366 nm acts as an in-coupling mirror, while a plano-concave mirror with a reflectivity of 99% at the same wavelength acts as an out-coupling mirror. The radius of curvature (ROC) of this mirror, which is *r* = 10 mm, determines that the distance between these two mirrors *d* should be exactly 5 mm for con-focal operation (*d=r/2)*. For this choice the Free Spectral Range is *FSR=c/(2d)*, where *c* is the speed of light. Hence, the FSR of the FPI for 366 nm is 30 GHz. Since there are 4 modes inside the interferometer, the effective FSR is 7.5 GHz.

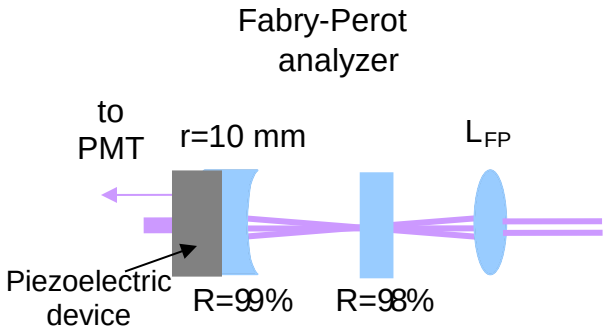

Figure 7-2: Design of the Fabry-Perot Interferometer.

To decide on the optimum radius of curvature (*r*) of the mirror for the extended study of RB scattering, simulations of RB-scattering were performed using the RBS Tenti-S6 code. The predicted scattering profiles (note that these profiles are not yet convolved with an instrument function associated with a specific FPI) are shown in Figure 7-3 and Figure 7-4. It can be concluded that although the scattering profile measured at 403 nm is significantly different from that measured at 366 nm, the span of frequencies covering the entire profile is almost the same (about 7 GHz), as long as the scattering angle is kept at the same value. Therefore, a FSR of 30 GHz is sufficient for the measurement at 403 nm for a scattering angle of 90 degrees. So we will keep the concave mirror at *r* = 10 mm.

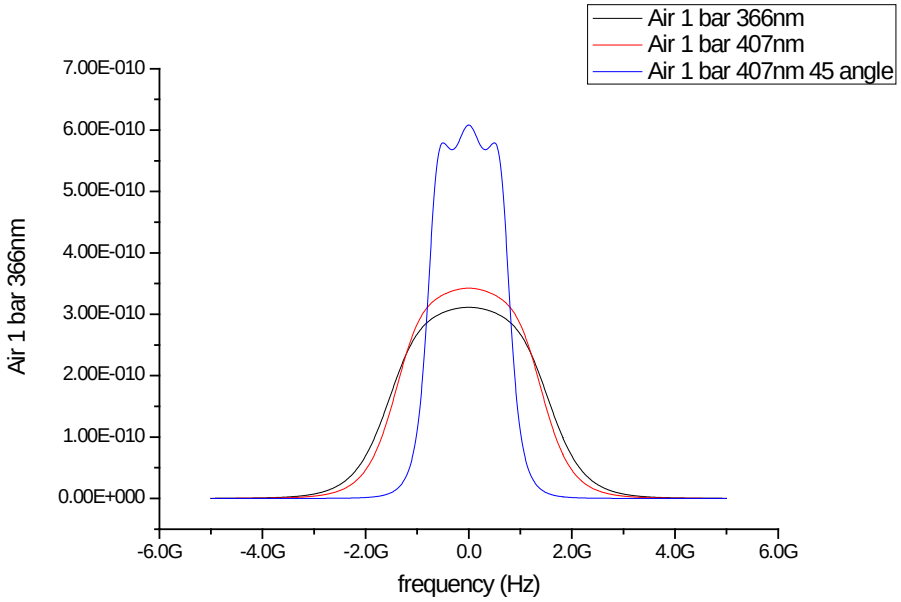

Figure 7-3: Predicted scattering profiles for air at 1bar. Calculations performed with the RBS-program for different wavelengths and detection angles. The resulting line shapes are not convolved with an instrument function of the FPI.

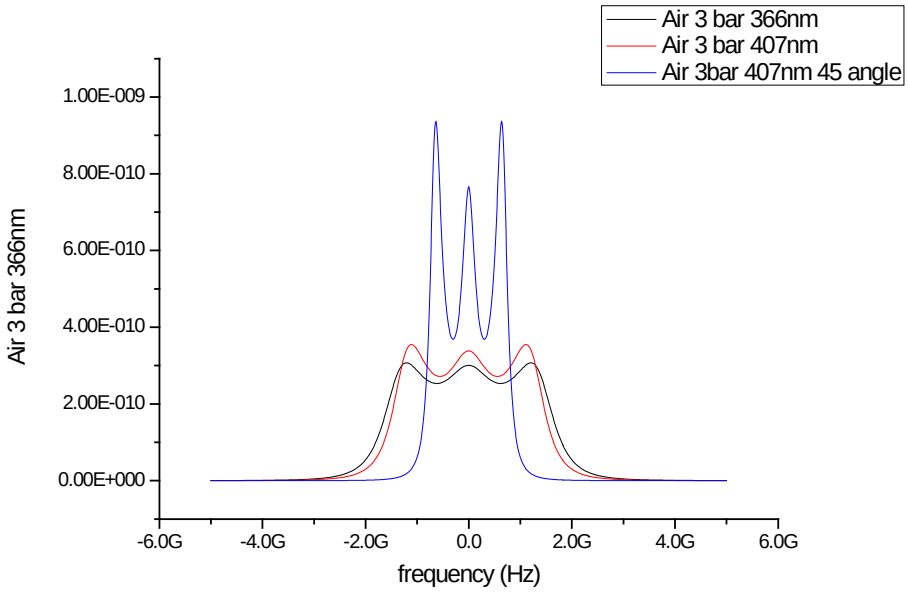

Figure 7-4: Predicted scattering profiles for air at 3 bar. Calculations performed with the RBS-program for different wavelengths and detection angles.

7.1.3.2 Finesse

The finesse of the FPI is associated with the reflectivity of the mirrors that are used to construct it. The finesse equals:

$$F = \frac{\pi\sqrt{\rho}}{1-\rho},$$

where $\rho=(VR)^{1/2}$ and R is the reflectivity of in-coupling mirror and $1\text{-}V$ are the losses per round trip (without taking into account the in-coupling mirror). These losses are caused e.g. by the transparency of the out-coupling mirror, imperfect mirror surfaces, fluorescence from the coatings, and scattering from the gas inside the cavity. Note that for low dissipative losses ($V \sim R_{out}$) this equation takes the more familiar form:

$$F = \frac{\pi\sqrt{R_{tot}}}{1-R_{tot}},$$

with $R_{tot}=(R_{in}R_{out})^{1/2}$. Note that the finesse also equals: $F = FSR/\Delta\nu_{instr}$.

Hence, when the *FSR* is kept at a constant value, a higher finesse *F* of the cavity will correspond to a narrower instrument profile. Therefore the detected profile will be more resolved. For different values of the finesse *F* of the FP, the measured profiles may be significantly different in terms of resolving the Brillouin side peaks, as is shown in Figure 7-3 and Figure 7-5. So, from the perspective of resolving power, the finesse is preferred to be as high as possible. This can be achieved by choosing the reflectivity of both in- and out-coupling mirrors as high as possible.
However, a compromise between good in-coupling efficiency and enough finesse must be sought for the experiment. This will be discussed in the next section.

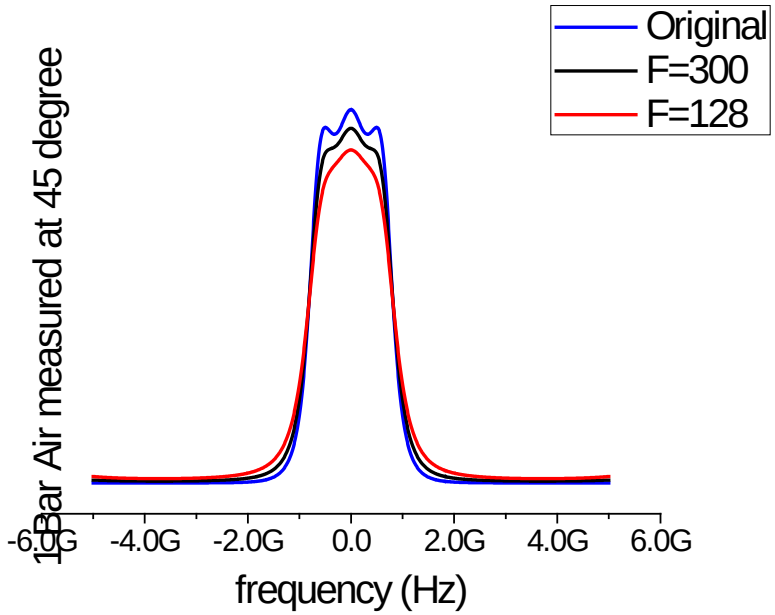

Figure 7-5: Predicted scattering profiles for RB scattering in air at 1 bar at 407 nm and 45 degree scattering angle (black). Resulting profiles for various values of the finesse of the FPI. Red curve F =300 (black) and F=128 (red). The blue curve pertains to the RB scattering profile without convolving an instrument profile. The effective FSR is 7.5 GHz.

7.1.3.3 Coupling efficiency

The in-coupling efficiency for the FPI is associated with the reflectivity of the mirrors. The amount of light coupled into a cavity depends on the impedance matching (reflectivity of the in-coupling mirror) and on the cavity mode matching (choice of in-coupling lens). In the following we assume a perfect Gaussian beam, perfectly mode-matched to the cavity. The coupling of the light into the cavity can be calculated as 1-*L*, where *L* is the part of the input beam that is reflected at the input mirror when the cavity is at resonance (when the length of the cavity is an integer of the wavelength):

$$L = \left(\frac{\sqrt{R} - \sqrt{V}}{1 - \sqrt{RV}} \right)^2$$

Here *R* is the reflectivity of the in-coupling mirror, and 1-*V* are the losses per round trip, without taking into account the in-coupling mirror reflectivity. Theoretically, according to the equation, *L* is zero when *R*=*V*, and this means that at *R*=*V* there is maximum light in-coupling. In the other word, for a perfect etalon, perfectly mode matched and impedance matched, the coupling efficiency of the FP analyzer can be as high as 100%.

The losses of the light inside a cavity can be classified:

- Transmission losses: the non-total reflectivity of the (out-coupling) mirror supposes a loss of the light inside the cavity (the in-coupling mirror is not taken into account). This means that if a mirror has a reflectivity of 97%, for every round trip, there will be a loss of 3% on this mirror. When the other losses (more about this below) are negligible, it means that V=97% and therefore the optimal coupling of the light occurs when the reflectivity of the in-coupling mirror is the same as for the out-coupling mirror.
- Dissipative losses: these losses are related to undesirable phenomena occurring inside the cavity: light scattered by the imperfections on the surface of the mirrors, gas molecules in between the mirrors, or fluorescence on the mirror surfaces. If these losses are of the order of the transmitted light (1-*R*), i.e. a few percent of the light, they are not negligible anymore and they will have an effect on the light coupled into the cavity.

In the previous (366 nm) campaign, it was decided to implement a R_{out}=99% concave mirror as an output coupler. For various mirror reflectivities R_{in} (for the input coupler) the impedance matching on the FPI was experimentally verified:

- R_{in} =99.5% delivered 5% coupling efficiency
- R_{in} =99% delivered 20% coupling efficiency
- R_{in} =96% delivered 40% coupling efficiency
- R_{in} =98% delivered 70-75% coupling efficiency. This is the mirror in use.

For an output coupler of R_{out}=99%, under the assumption of no dissipative losses, the most efficient input coupler would be R_{in}=99%. The fact that the best in-coupling is experimentally obtained with R_{in}=98%, implies that dissipative losses are in the vicinity of

1%. This can either be ascribed to real dissipation processes occurring inside the cavity, i.e. reflection losses, or for a part also to imperfect mode-matching at the input.

For the FPI to be designed for RB scattering at 407 nm, a choice for reflectivity R_{in}=99% would be preferred, to reach a high finesse. At longer wavelengths the dissipative losses due to mirror imperfections are expected to become gradually lower, while also scattering from the gas molecules in the cavity becomes less at longer wavelength. However, quantifying the losses without any test is impossible. Therefore, mirrors with reflectivities of 99%, 98.5% and 98% were tested in order to obtain the highest in-coupling efficiency.

7.1.3.4 The proposed structure of the FP analyser

For the measurements to be performed at 403 nm (initially 407 nm was defined) at a detection angle of 90 degrees, the radius of curvature (ROC) of the out-coupling mirror is determined to be the same as the one used for the 366 measurements (ROC = 10 mm), according to the simulation in Sec. *2.1.3.1*. The reflectivity is preferred to be 99% for the finesse requirement. The reflectivity of the in-coupling mirror might be 99%, if dissipative losses, which are expected to be lower at 403 nm than at 366 nm, are negligible. If the dissipative losses are about 0.5% or even 1% of the total light, however, the chosen reflectivity should be 98.5% or 98%, respectively, to acquire the maximum coupling efficiency. Theoretically, with the reflectivity of the in-coupling being 98%, 98.5% or 99%, the calculated finesse of the cavity is 155, 207 or 312. With an output coupler at ROC = 10 mm (so the FSR of the cavity is 30 GHz), the calculated instrument line width will be 193, 145 or 96 MHz, respectively. In practice, the finesse will be lower than the calculated one, because effects of improper impedance matching always will play a role. For example, the calculated finesse of the FPI currently used for 366 nm is 155, while the measured finesse is around 130. Test experiments will eventually decide on the choice of the optimum parameters for the optics. The proposed design of the FPI for 403 nm and 90 degree angle is shown in Figure 7-6.

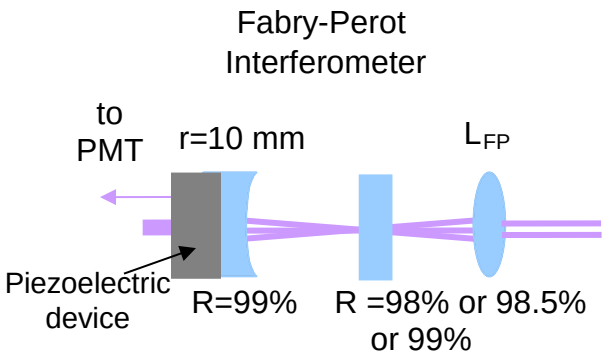

Figure 7-6: Design of the FPI for measurement at 403 nm with a detection angle of 90 degree.

7.1.3.5 Purchase of Coatings & Mirrors

Considering all requirements (finesse, FSR of the FPI and the coupling efficiency), a variety of mirrors with reflection coatings and ROCs were ordered, for the central wavelength of 407 nm. Each mirror is also to be coated with an anti-reflection coating at the rear surfaces to reduce the losses, and avoid unwanted stray light.

The coatings purchased from Laser Optik GmbH are listed below:

- Coating of R=99% @ 407nm
- Coating of R=98.5% @ 407nm
- Coating of R=98% @ 407nm
- Anti-reflection coating @ 407nm on the rear side of each mirror

Figure 7-7 displays the transmission curve of the coating R=99% from Laser Optik GmbH. The thick line shows the real transmission as a function of the wavelength with the smallest value at 407 nm. The thin line is the 10 X zoom in from the thick one. According to this figure, we can actually tune the transmission of the mirror by changing the wavelength of the laser to make the FP ideally optimized for the experiment (This is the reason that we finally use 403 nm instead of 407 nm for real measurements).

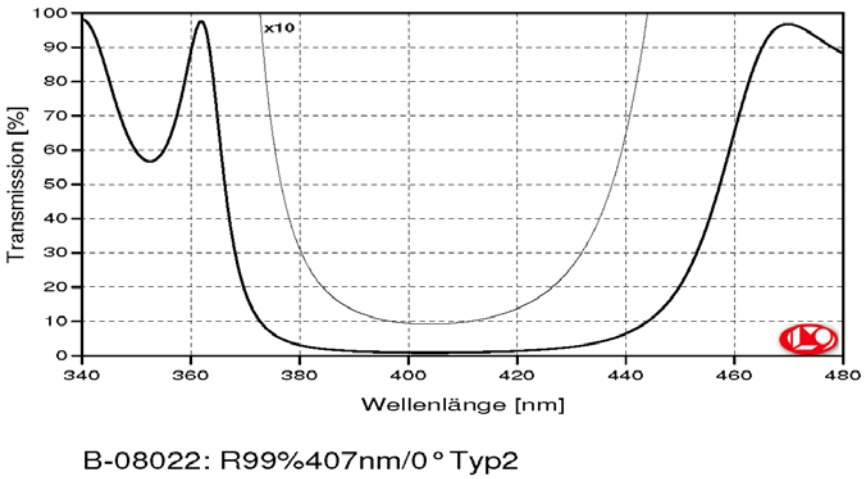

Figure 7-7: The transmission curve of the coating R=99% from Laser Optik GmbH. The thick line is the transmission curve and the thin one is the 10 X zoom in curve of the thick one.

The mirrors purchased form Laser Optik GmbH are listed below:

- Plano-concave mirrors with ROC = -10 mm: 3 pieces R99% + 2 pieces R98.5% + 2 pieces R98%
- Plano-concave mirrors with ROC = -15 mm: 3 pieces R99% + 2 pieces R98.5% + 2 pieces R98%
- Plano-concave mirrors with ROC = -18 mm: 1 pieces R99% + 1pieces R98.5% + 1 pieces R98%
- Plano-concave mirrors with ROC = -20 mm: 2 pieces R99% + 2 pieces R98.5% + 2 pieces R98%

- Plano-concave mirrors with ROC = -50 mm: 1 pieces R99% + 1 pieces R98.5% + 1 pieces R98%
- Plane-mirrors for the in-coupling of the FPI: 2 pieces R99% + 4 pieces R98.5% + 4 pieces R98%

The reason for ordering mirrors with *R*=98.5% and 98% as well as those with *R*=99% is that there is always an uncertainty of *R*=± 0.3% from the production process. To make sure that the experiment would not be delayed, mirrors with coatings and substrates to cover a wide parameter space were ordered.

7.1.3.6 Construction and characterization of the FPI

After trying several possibilities mentioned in the previous section, a plane mirror with 98.5% reflectivity is used as the in-coupling mirror of the FPI, while a mirror with 99% reflectivity and -10 mm radius of curvature is used for out-coupling. The FSR and instrument linewidth of the FPI are characterized by scanning the frequency of the reference laser beam and measuring the transmission curve of the FPI.

Figure 7-8 shows the transmission curve of the FPI in a full FSR scale. It indicates that similar to the FPI used at 366 nm, the new one also maintains four modes in a FSR.

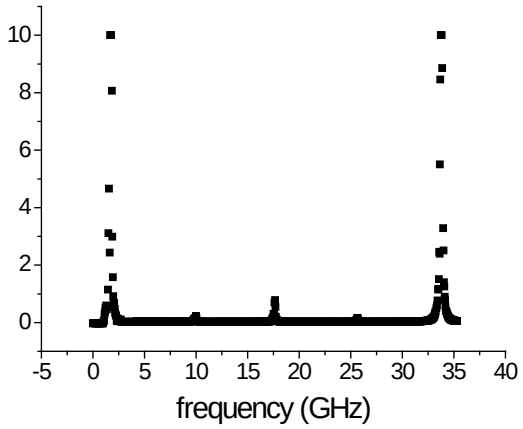

Figure 7-8: The transmission curve of the FPI on a full FSR scale

The accurate value of the FSR is measured by scanning the laser frequency over a wide range to measure multiple FSRs. The black points in Figure 7-9 indicate the (relative) laser frequency f_n where the nth maximum transmission of the FPI occurs. Because the FSR is a constant, f_n and *FSR* should follow the simple equation:

$$f_n = n \cdot FSR + f_0 ,$$

where f_0 is just a random number. So the slope of the linear fit of the black points in Figure 7-9, which 30.21 GHz as indicated in the table, is the averaged value of the FSR. The standard deviation of this fit (average) is 80 MHz.

The instrument linewidth, by definition, is the full width at half maximum (FWHM) of each mode. Because the cavity mode has a Lorentzian line shape, the FWHM is obtained by

fitting the maximum of the peak (mode) to a Lorentzian function. Figure 7-10 indicates that the width of the fitting Lorentzian peak, hence the instrument linewidth, has a value of 139.7 $\pm$ 1.9 MHz.

Knowing the FSR and the instrument linewidth (FWHM), the instrument function of this FPI can be written as:

$$A = I_0 \cdot \frac{1}{1 + \left(\frac{2 \cdot FSR}{\pi \cdot FWHM}\right)^2 \cdot \sin^2\left(\frac{\pi}{FSR} \cdot f\right)}$$

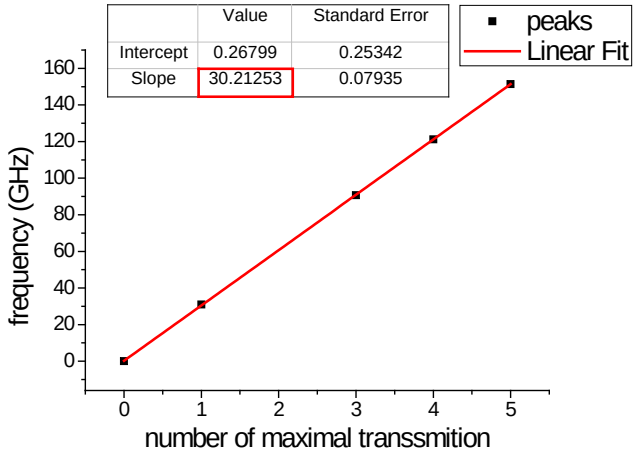

Figure 7-9: The (relative) laser frequency f_n where the nth maximal transmission of the FPI occur

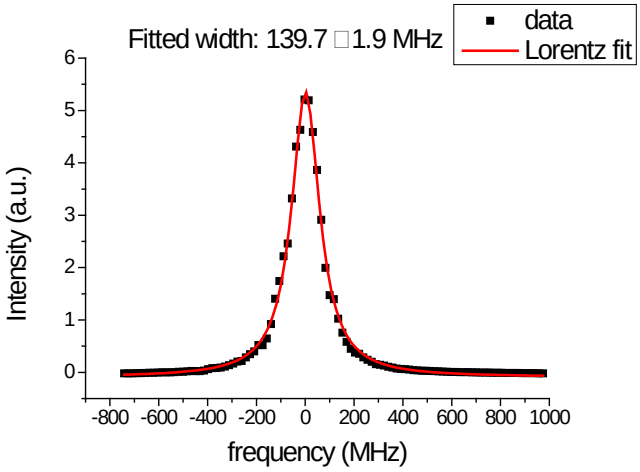

Figure 7-10: The transmission curve of one maximal FPI mode (black dots) and the Lorentzian fit to the data.

Alternatively, the instrument profile can be measured from a direct elastic scattering measurement. By putting a copper wire inside the scattering cell, light from the laser beam is elastically scattered into all directions. A fraction of the scattered light will follow

exactly the same path as the RB-scattered photons, going through the photon collecting arm, the Fabry-Perot Interferometer and finally being detected by the PMT. This method seems more robust to measure the true instrument function of the Fabry-Perot Interferometer. However, for this method we need to scan the applied voltage of Fabry-Perot Interferometer instead of the laser frequency, so the x-axis is in the unit of voltage, which needs to be converted into frequency using the results (measured FSRs) from the first (frequency-scanning) method mentioned above.

Figure 7-11 shows the elastically scattered photons measured by the PMT as a function of converted frequency. By following the same procedure which is always used to obtain the final RB-scattering profile or gases, all the elastically scattered peaks in Figure 7-11 are integrated and averaged into area unity, indicated as black line in Figure 7-12. The red line in Figure 7-12 represents a Lorentzian fit to the measured peak, deriving a FWHM of 141±0.8 MHz, which agrees with the result shown in Figure 7-10.

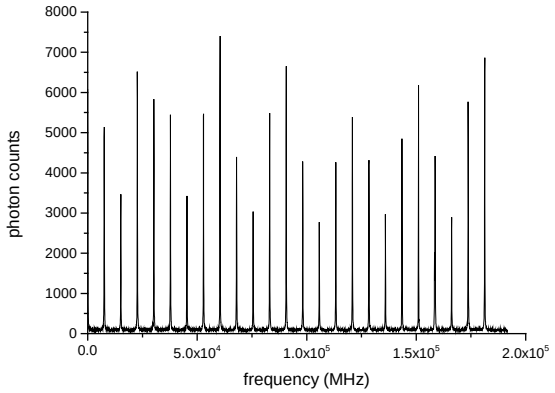

Figure 7-11: The measured elastically scattered photons as a function of converted frequency.

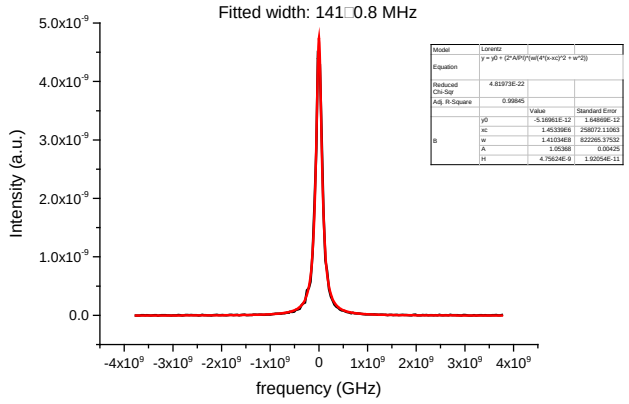

Figure 7-12: The averaged elastic scattering profile (black) and its Lorentzian fit (red), which derives a FWHM of 141±0.8 MHz.

7.1.4 Introduction of a narrow-band filter to remove light from non-RBS processes

RB scattering measurements always suffer from background problems. The side wings of the measured scattering profiles are always higher than side wings of the Tenti S6 calculations, even after the dark counts of the PMT and the overlap of consecutive FSRs have already been taken into account. This indicates that the measurements suffer from a background problem, which had been ascribed previously [6] to broadband fluorescence of the cell windows. However, fluorescence is unlikely to play a role here, because non-coated windows are used for the laser beam to pass through the cell and bare fused silica exhibits a fluorescence spectrum longward of 400 nm, while this part of the spectrum is filtered before detection.

Raman scattering, amounting to ~2.5% of the total cross section, is another possible source of background. The rotational Raman scattered light, with a large number of individual components of width ~3 GHz distributed over several nm, is effectively spread over many modes of the FPI, resulting in a broad, structureless background. Previously, this additional background, amounting to ~2% of the central Rayleigh peak intensity, was corrected by artificially adding some background in the models to fit the measured background and renormalizing the calculated models (see Figure 7-13 (a)), as detailed in [1] and [6]. Because of this additional fitting, one may question the reliability of the modified model. For the measurements at 403 nm a 1 nm bandwidth filter (see Figure 7-14), which is expected to filter out most of the rotational Raman scattering and all the vibrational scattering, was implemented in the setup. Although the measurements with the narrow band filter indicate that the side wings of the measurements are reduced to the original Tenti model (see Figure 7-13 (b)), the measurements still have 1~2% difference with respect to the Tenti S6 model (see Section 8.1 for all the measurements), indicating that all the previous measurements at 366 nm (see [1] and Section 4) without a 1 nm filter are reliable.

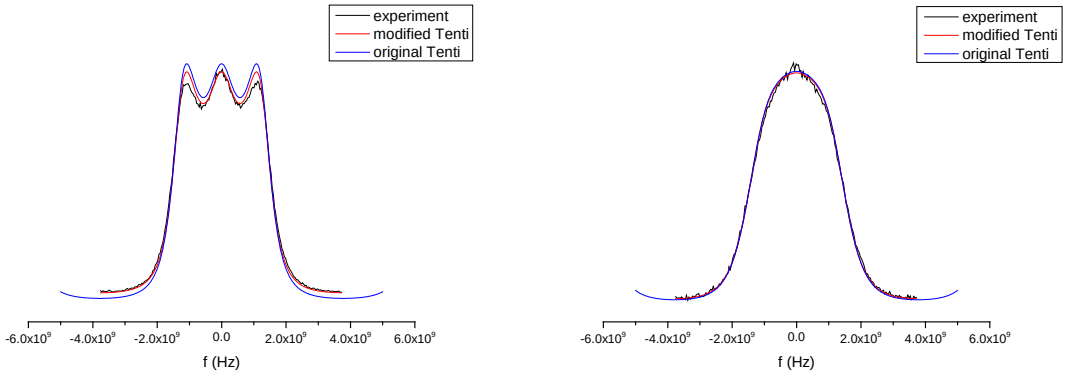

Figure 7-13: (a) The measurement (black) at 366 nm without a 1 nm filter maintains an higher side wings than those of the original Tenti model (blue). In order to compare the measurements with the model, the Tenti model was modified by adjusting the side wings to those of the measurements, followed by a renormalization procedure, which resulted in a modified Tenti model (red). (b) the measurement (black) at 403 nm with a 1 nm filter provided by DLR, the original Tenti model (blue) and the modified Tenti model (red) have the same level of background.

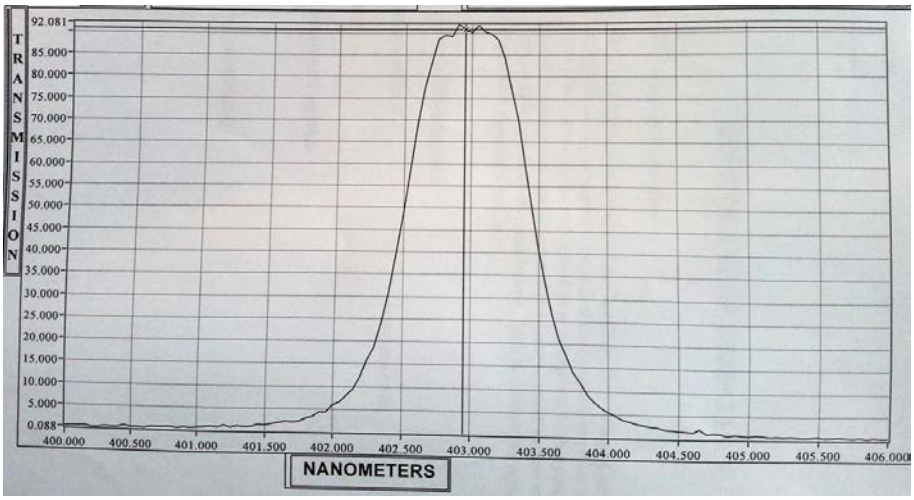

Figure 7-14: Transmission curve of the 1 nm filter used for 403 nm measurements.

7.2 Setup for scattering at 532 nm and smaller scattering angle

It was planned to perform small angle scattering measurements at a wavelength of 532 nm with use of a VERDI laser. Due to time constraints and costs a choice had to be made to first produce results on RB-scattering at 403 nm, and delay the collection of results from the small angle RB setup. Nevertheless progress was made in the construction of the setup for small angle scattering:

- Purchase of all optical components for 532 nm
- Design and manufacturing of a smaller angle (55^o) scattering cell
- Construction of a FPI for 532 nm

In the process of building this setup some problems were encountered, as described in section 2.2.2, which still have to be mastered. It is anticipated that measurements at 532 nm scattering at 55^o can be performed in the near future, after completion of ESA contract 21396/07/NL/HE CCN-2. In the following a description is given of the preperatory activities for the 532 nm small angle RB-scattering studies.

Figure 7-15 shows a sketch of the proposed layout of a setup to be used for small angle scattering at 532 nm. The laser beam generated by the VERDI laser, after 3 beam-steering reflections, is focused at the centre of the scattering cell providing the incident light for RB-scattering. A fraction of the laser beam leaking through M3, focused at the same point as the main beam, is used as a reference beam for aligning the Fabry-Perot Interferometer and the other optics. Basing on the geometry of the scattering cell, the scattering angle is constructed to be 55° (see Figure 7-16). Similar to methods previously used, the scattered photons are spatially cleaned by a 35 μm pinhole, spectrally filtered by another home-made Fabry-Perot Interferometer, and finally detected on a photo-multiplier tube (PMT).

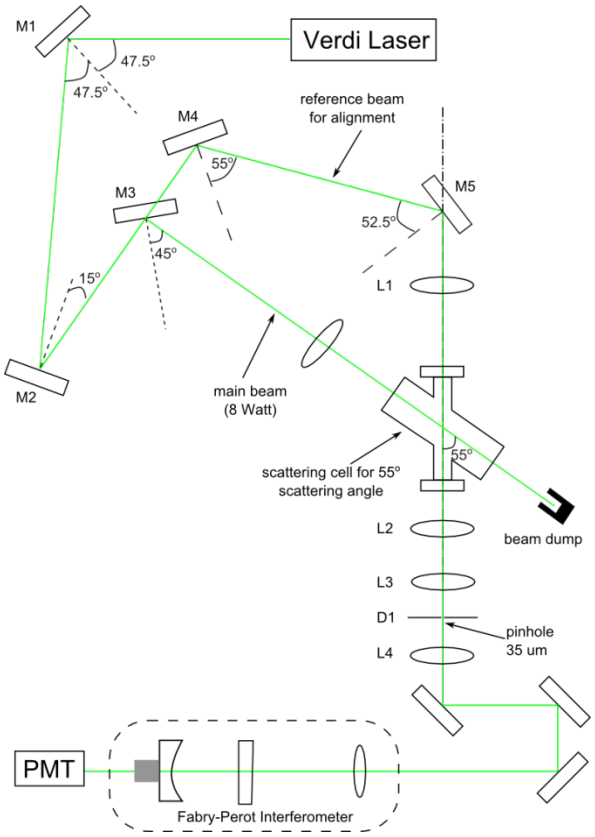

Figure 7-15: The proposed setup for the 532 nm 55° RB-scattering experiment.

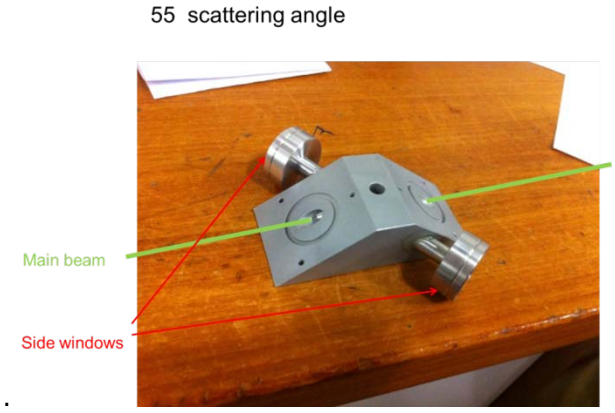

Figure 7-16: The scattering cell for 532 nm 55° RB-scattering experiments.

7.2.1 Fabry-Perot Interferometer for 55°

In order to choose optical elements with optimized properties for a FPI to detect RB-scattering at an angle of 55°, RB scattering profiles at this angle were calculated. Figure

7-17 shows simulations of scattering profiles of air at 1 bar and 3 bar for 532 nm wavelength and 55° scattering. It shows that both of the profiles cover a frequency range of ~3 GHz. Therefore, a FPI with a FSR of 12 GHz (4x3 GHz) should be most suitable.

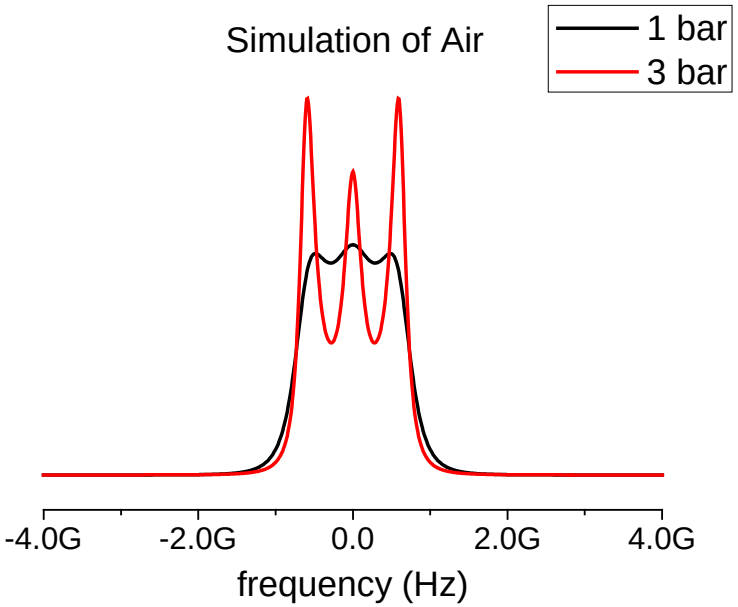

Figure 7-17: Simulated scattering profiles of air for 532 nm and 55° scattering angle. Note that these simulations are not yet convolved with the instrument function of a FPI.

7.2.1.1 The proposed layout of the FPI

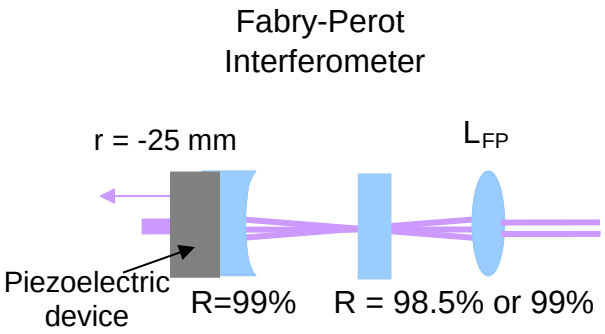

Figure 7-18: Proposed geometrical layout of the FPI.

A (plano-confocal) geometry is proposed for the FPI for 532 nm and 55° scattering angle (see Figure 7-18), similar as for the experiments performed at 366 nm and 403 nm. According to the simulation shown in Figure 7-17, the most suitable FSR is 12 GHz, which involves a mirror with ROC of - 25 mm (see Sec. 7.1.3.1 for the calculations). In order to obtain a high finesse, the reflectivity of the out-coupling mirror is proposed to be

99%, while that of the in-coupling mirror is proposed to be 98.5% or 99%, depending on impedance matching.

7.2.1.2 Purchase of Coatings & Mirrors

To ensure more degrees of freedom to build a suitable FPI, a set of mirrors covering a variety of focal lengths and reflectivity coatings were ordered. Again, these were purchased from Laser Optik GmbH.

Coating batches ordered:

- Reflectivity of 99% at 532 nm
- Reflectivity of 98.5% at 532 nm
- Reflectivity of 98% at 532 nm
- Anti-reflection coatings on the backside

Mirror substrates purchased:

- wedged window 25 x 6.35 mm (2 pieces 99%, 3 pieces 98.5%, 3 pieces 98%)
- Plano concave mirror r= -15 mm (2 pieces 99%, 2 pieces 98.5%, 2 pieces 98%)
- Plano concave mirror r= -25 mm (2 pieces 99%, 2 pieces 98.5%, 2 pieces 98%)
- Plano concave mirror r= -50 mm (1 pieces 99%, 1 pieces 98.5%, 1 pieces 98%)

7.2.1.3 Construction and characterization of the FPI

The final version of the FPI consists of a plano concave mirror with r = -25 mm and reflectivity R=99% (out-coupling mirror) and wedged window with R=98.5% (in-coupling mirror). Because r =-25 mm, the distance between these two mirrors should be 12.5 mm, thus the FSR should be 12 GHz.

All the components for this FPI have been mounted on a 70 mm thick aluminium base plate for stabilization over a measuring period of 3 hours. Figure 7-19 shows a photo of the display of an oscilloscope, showing the four modes of the FPI similar as found for the other FPI's constructed (366 nm and 403 nm). Improvement of the alignment is still warranted to generate symmetric modes with optimized coupling efficiency. This will be pursued in a later stage after the entire setup has been constructed.

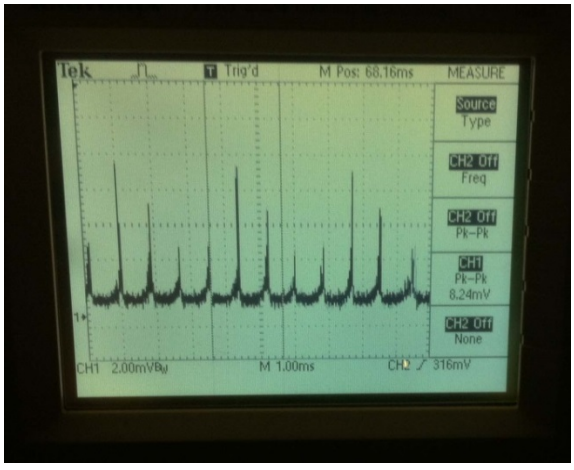

Figure 7-19: A photograph of the display of the oscilloscope which resolved the modes of the FPI.

7.2.2 Difficulties and improvements to be made

7.2.2.1 Accurate alignment of the setup

Not only the FPI for 55° needs to be precisely aligned, this also holds for the other parts of the setup. For example, the focus of the main beam, the focus of the reference beam and the center of the scattering cell should coincide in space, otherwise the reference beam cannot be used to align the photon collecting part and the FPI.

7.2.2.2 Sealing from ambient light

To detect the RB-scattering profile at a high signal to noise ratio, our setup is made to be extremely sensitive to photons. Therefore, any photons from ambient light will be detected by our system, and eventually affect the results of our measurements. Therefore the photon collecting arm and the FPI should be well sealed by black plates. The sealing setup still needs to be designed and constructed.

7.2.2.3 Elastic scattering problems

Elastic scattering inside the scattering cell has been known to cause major difficulty for the other setups designed for 90° scattering angles. To eliminate elastically scattered light from the inside of the cell, the walls should be covered by absorbing paint and several light traps and baffles should be installed inside the scattering cell. Figure 7-20 shows a side view of the designed (55°) scattering cell. The green laser beam incident from the right will experience several reflections before exiting the scattering cell. Each reflection causes an additional laser beam. Although these additional laser beams are much weaker than the main beam, they are still far stronger than the scattered light by gas molecules. Therefore each beam caused by the reflection needs to be trapped. There are already four traps (indicated in blue) constructed at the proper positions. However, there is still one reflection that has not been considered (indicated with a red cross). An additional trap needs to be made for this reflection. Moreover, the traps are not yet covered with special absorbing paint.

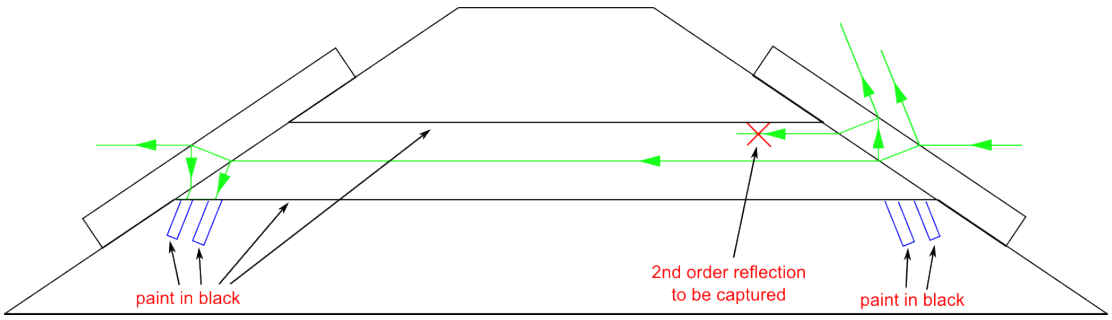

Figure 7-20: Side view of the scattering cell for 55° experiment. Laser beam paths are indicated in green. Red inserts indicate unfinished work.

7.2.2.4 On the choice of the 55° scattering angle

Figure 7-21 demonstrates the difficulty of combining a setup for small angle scattering with an enhancement cavity, which would be necessary for such measurements a 366 and 403 nm. The required geometry for the enhancement cell does not permit small scattering angle since the arms of the scattering cell will block the beam path (indicated in solid blue lines). For this reason, a choice was made to resort to the 532 nm VERDI

laser to be used at small angle scattering, because that laser produces sufficient laser power (> 9 Watt) at narrow bandwidth so that it can be used in an RB-scattering setup without enhancement. Still the angle cannot be chosen as small as desired, since in our cell design sealed windows are to be used for high pressure applications. That is the basis for a compromise at a 55^{o} scattering angle.

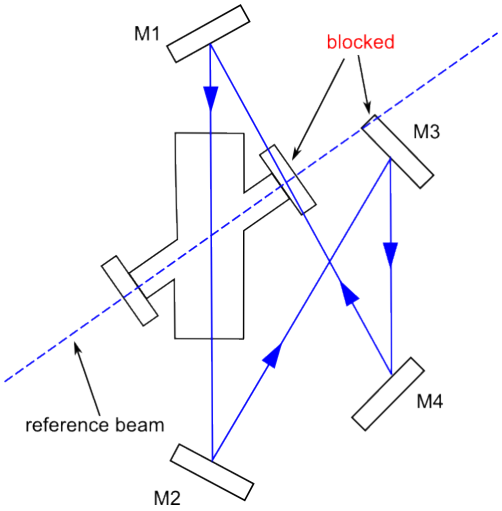

Figure 7-21: A sketch which demonstrates that placing the 55° inside the enhancement cavity for 403 nm is impossible.

8 Experimental results

8.1 Measurements at 407 nm and 90 degree scattering

Measurements in air and N_2 at both 1 and 3 bar, 403 nm with a detection angle at 90 degree are performed. The measured data are shown as black dots in Figure 8-1 to Figure 8-4. The red lines in each figure are the Tenti S6 calculations for the same conditions.

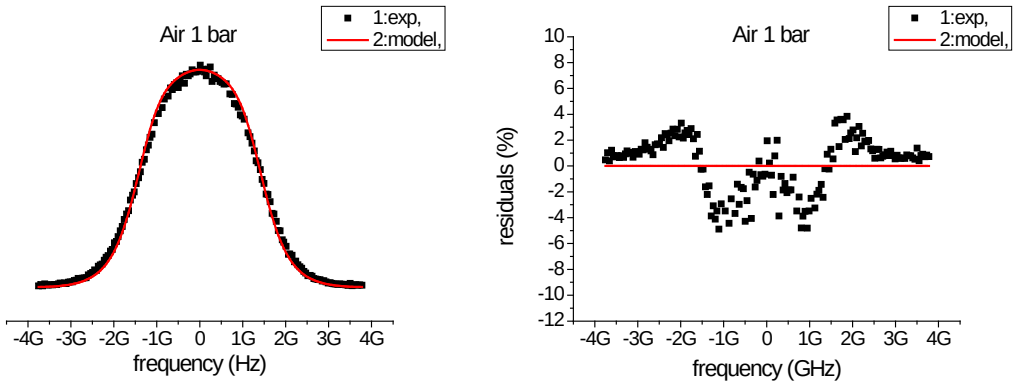

Figure 8-1: Comparison between measured (black dots) and calculated (red line) scattering profile for 1 bar air at room temperature.

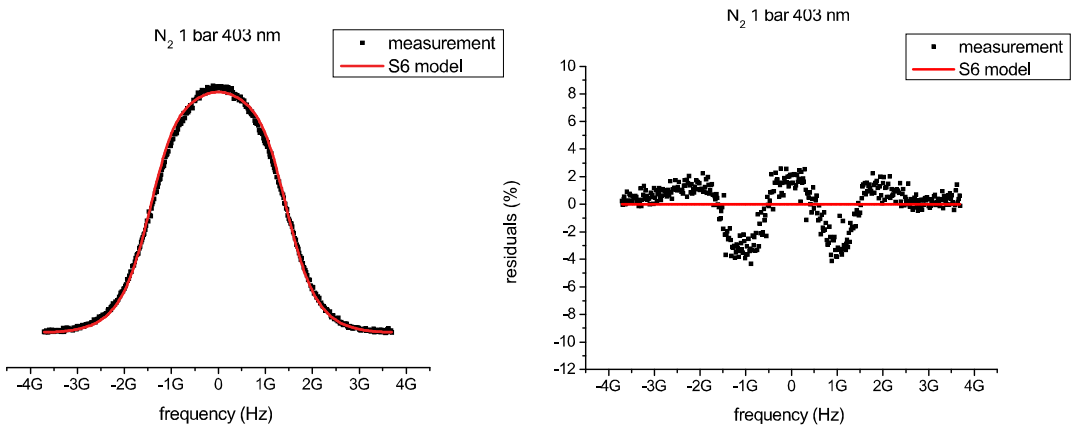

Figure 8-2: Comparison between measured (black dots) and calculated (red line) scattering profile for 1 bar N_2 at room temperature.

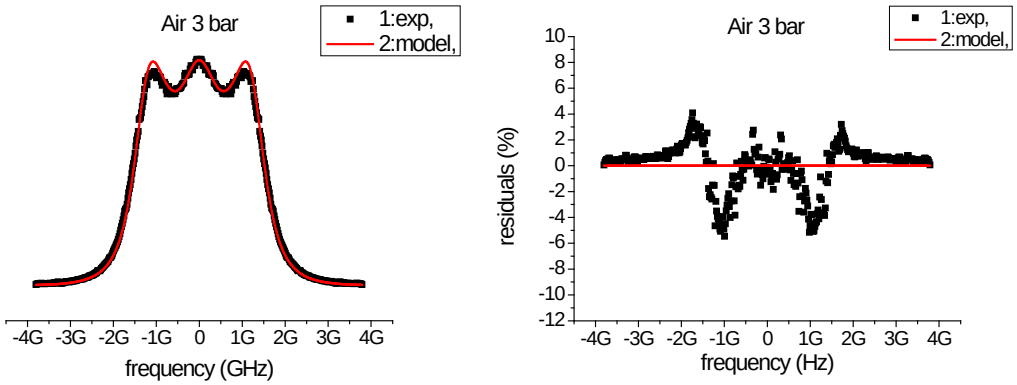

Figure 8-3: Comparison between measured (black dots) and calculated (red line) scattering profile for 3 bar of air at room temperature.

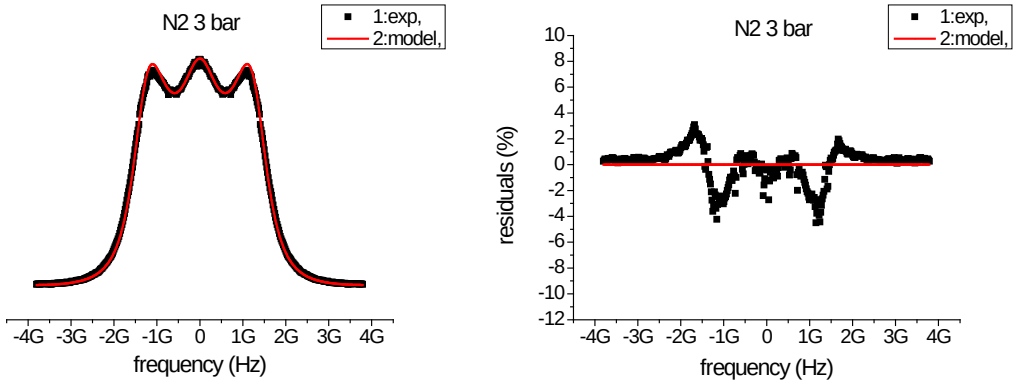

Figure 8-4: Comparison between measured (black dots) and calculated (red line) scattering profile for 3 bar of N2 at room temperature.

It is obvious that the residuals between the measured scattering profiles and the calculations are significant for all cases. Several months have been spent to find the actual reason for these deviations, before it was found that the scattering angle was ~2° larger than 90°. Figure 8-5 is a top view of the layout of the scattering cell for 90°. In principle, the two pinholes together with geometry of the scattering cell limit the scattering angle to be 90±0.9°. However, one of the two pinholes was removed when switching the wavelength from 366 nm to 403 nm to acquire more freedom in the alignment procedure. The pinhole was removed without carefully considering the consequences, presuming that it only acted as a filter for stray light. However, it is also a key component to limit the scattering angle. Extensive delay was caused to clarify this issue.

After finding that the scattering angle is the cause of the discrepancy, the new angle was applied to calculate the S6 model. The measurements and the calculations are compared in Tab. 3-1 to 3-5 for different pressures, temperatures and gases indicated. It is clear that now the measurements agree with the model very well. To further prove that the scattering angle stay within the deduced value of 91.8° ± 0.1° over a long time span, fitted angles (using the S6 model calculations) for the measurements on different dates

and at different conditions are plotted in Figure 8-6. It is clearly shown that the scattering angle stays the same for a period of 10 months, and for different conditions.

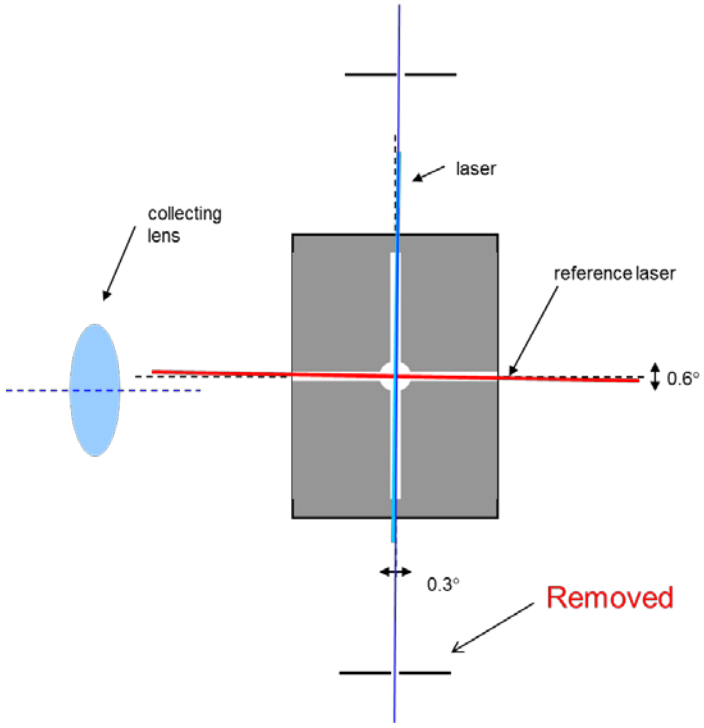

Figure 8-5: Top view of the layout of the scattering cell for 90°.

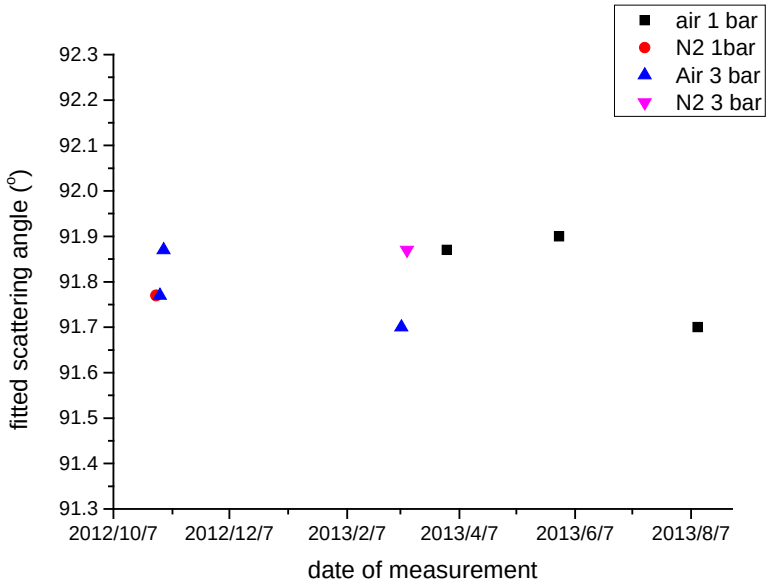

Figure 8-6: Fitted scattering angle for the measurements on different dates and at different conditions

Table 8.1: Measured scattering profiles and Tenti S6 models, for measurements of air performed at different pressures and temperatures.

T [℃]	1.0 bar	2.0 bar	3.0 bar
-20	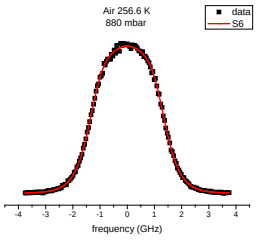		
4	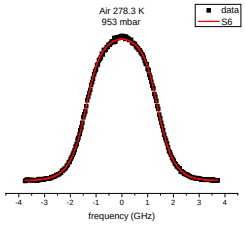	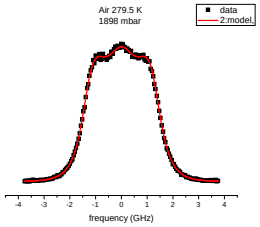	
24	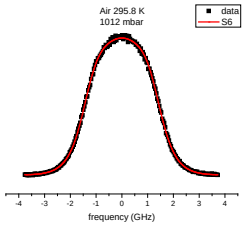	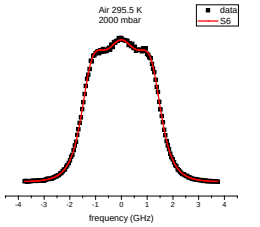	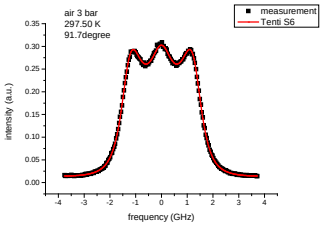
45	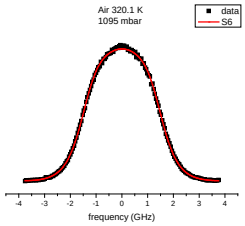	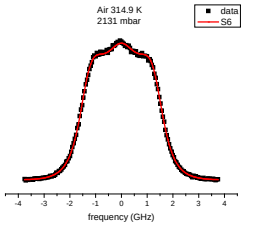	
65	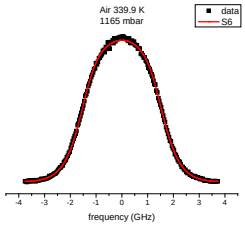	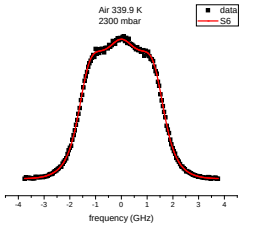	

Table 8.2: Deviations model-measurement in percentage of the maximum signal of the model, for measurements of air performed at different pressures and temperatures.

T [℃]	1.0 bar	2.0 bar	3.0 bar
-20	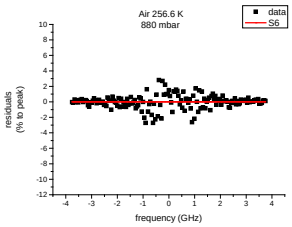		
4	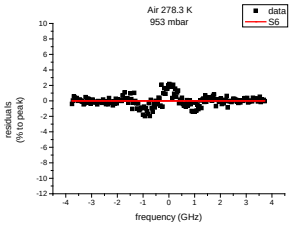	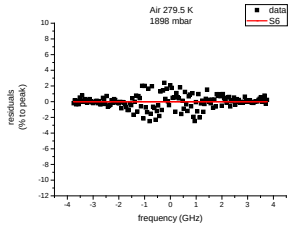	
24	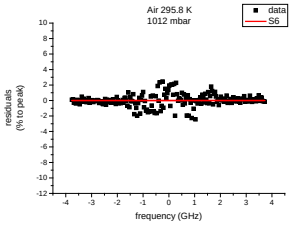	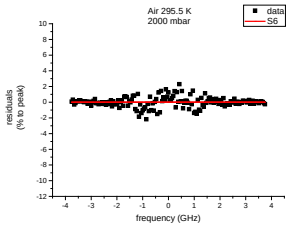	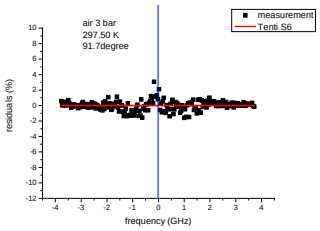
45	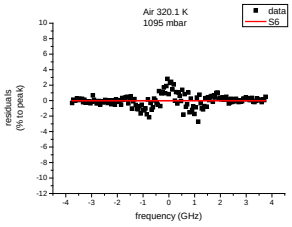	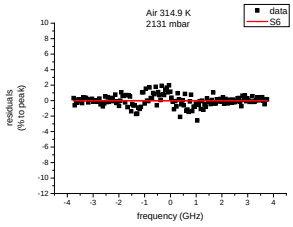	
65	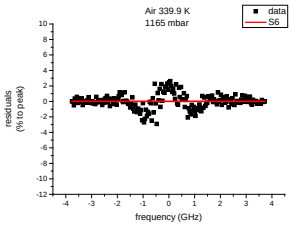	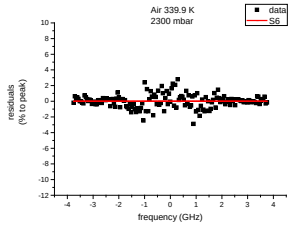	

Table 8.3: Measured scattering profiles and Tenti S6 models, for measurements of N_2 performed at different pressures and temperatures.

T [℃]	1.0 bar	3.0 bar
-20	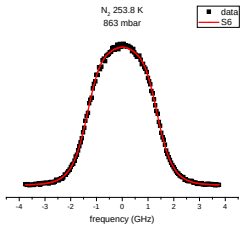	
4	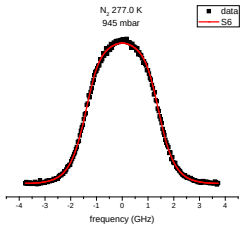	
24	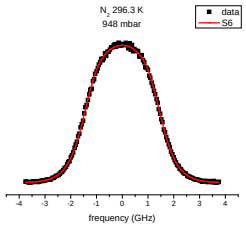	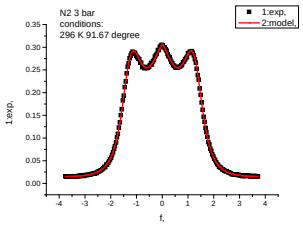
45	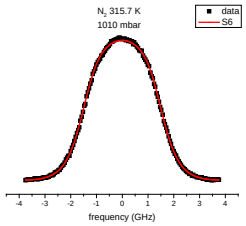	
65	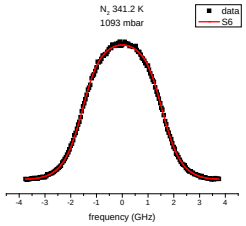	

Table 8.4: Deviations model-measurement in percentage of the maximum signal of the model, for measurements of N_2 performed at different pressures and temperatures.

T [℃]	1.0 bar	3.0 bar
-20	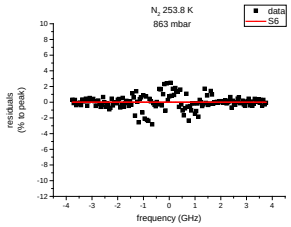	
4	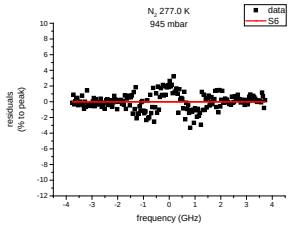	
24	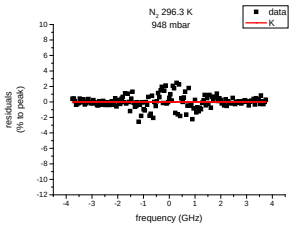	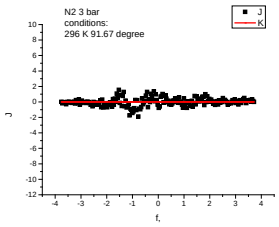
45	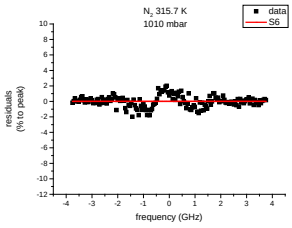	
65	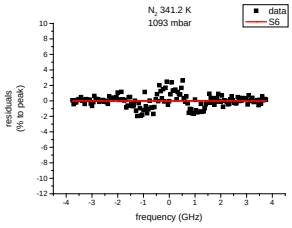	

Table 8.5: Measured scattering profiles and Tenti S6 models, and the deviations between them for measurements of other different gases performed at different pressures. All measurements at room temperature.

Gas & pressure	Comparison	Residuals
O2 1 bar	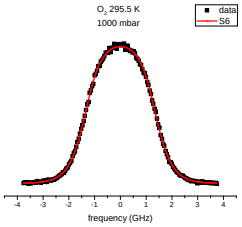	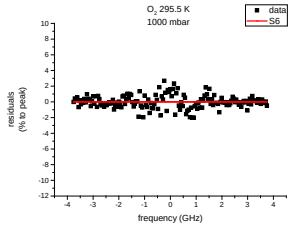
O2 2 bar	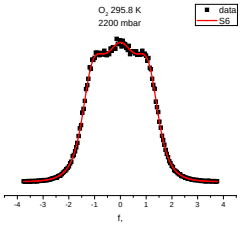	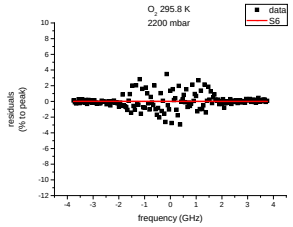
Ar 1 bar	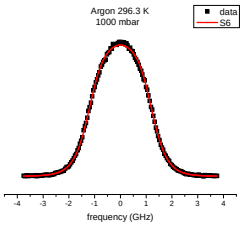	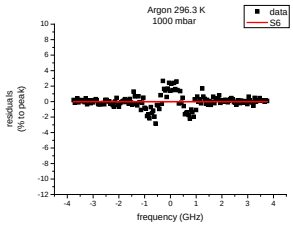
CO2 0.5 bar	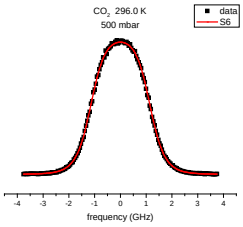	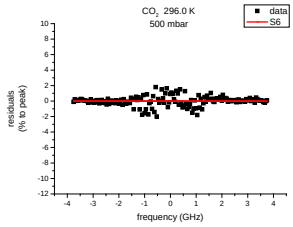
SF6 0.2 bar	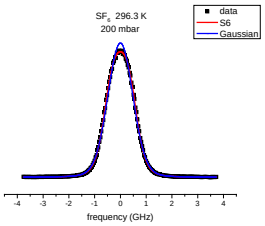	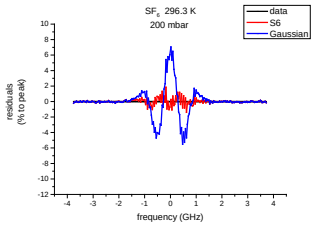

A further in-depth analysis of the experimental results will be given in the following sections.

9 Conclusion Part II

The objective of this part was to perform SRBS measurements at a wavelength significantly different from 366 nm and at a different scattering angle for air and nitrogen at 1 and 3 bar. Due to experimental difficulties, delays and time and cost constraints, measurements for a different scattering angle (55° at 532 nm) could not yet be performed, but an extensive investigation of SRBS for a large set of gases and mixtures at several pressures and temperatures at 403 nm could be realized. Nevertheless progress has been made in designing a setup for the angular measurements at 532 nm, purchasing optics and designing and manufacturing a scattering cell as well as a FPI, so that these measurements can be performed in the near future.

The experimental set-up was described together with the measurements (Table 8.1 to

Table 8.5). A more detailed measurement analysis will be presented in Part III of this report. The main conclusion from this investigation is that the Tenti model is proven to be valid for single-atomic and diatomic gases within 1~2% accuracy level at a new wavelength (403 nm). Implementing a narrow-band filter for SRBS measurements, which is aimed to eliminate contributions from non-SRBS processes, introduces no difference in the measurement-model comparisons. For the polyatomic gases and the gas mixtures consisting of significantly different gas components, the Tenti model fails in describing the measurements.

Part III

The objective of this part was to verify the Tenti S6 model using a set of Spontaneous Rayleigh Brillouin Scattering (SBRS) measurements in a range of settings for temperature, pressure, wavelength, and scattering angle, as obtain in Part II. Furthermore, the experimental and theoretical results will be analysed and discussed in detail.

At present the Tenti S6 code, as delivered under ESA contract 21396 and described in [1], is suited to calculate Rayleigh-Brillouin scattering profiles for a wide variety of conditions. In particular, the parameters describing the specific physical conditions and the geometry of the experiment (such as the wavelength dependence, and the angle dependence) can be straightforwardly implemented.

In [1], the Tenti S6 model was validated using measurements of air and N_2 at different pressures at room temperature at one given wavelength (366 nm). In the present activity, the experimental conditions have been extended to a larger temperature range. The S6 codes can therefore be further validated and optimized by adapting the transport properties of the gaseous materials as a function of temperature. A search in the scientific literature has been performed to obtain the temperature-dependent transport coefficients of different gases. Amongst these, the bulk viscosity, which is a macroscopic gas transport coefficient, is the less well known. Only sparse information from acoustic experiments on different gases is available, hence its value at hypersound frequencies (~ 1 GHz) of relevance to RB-scattering is largely unknown. In [1], the SRBS line shapes calculated by the Tenti S6 model were fitted to SRBS measurements performed in controlled laboratory experiments by adjusting the bulk viscosity. A FORTRAN version of the Tenti S6 code by Pan [7] was further modified to allow for the fitting of the bulk viscosity. The modified code from [1] is called the *RBS programme* in the remainder of this document. The transport coefficients in the *RBS programme* have been included for the gases at different temperatures and pressures. This is described in detail below.

We note that a numerical optimization of the Tenti models, at its foundations of gas kinetic theory, falls outside the scope of the present study. Rather, the model improvement will be performed through fitting of the existing model gas transport parameters. Currently, there exists no alternative as to the formalism of Tenti S6 (or S7) for describing SRBS profiles. However, analytical models have recently been developed by two different groups, and optimized based on a.o. measurements from [1] and this study. These have been published in open literature scientific journals [8-10].

10 Scattering processes as described by the Tenti S6 model

10.1 The origin of light scattering

Scattering occurs as the result of fluctuations in any of the optical properties of a medium, which can be described by the dielectric tensor [11]:

$$\varepsilon_{ik} = \varepsilon_0 \delta_{ik} + \Delta\varepsilon_{ik} \tag{10.1}$$

where ε_0 is the mean dielectric constant and $\Delta\varepsilon_{ik}$ represents the fluctuations in the dielectric tensor. These fluctuations can be separated in two parts:

$$\Delta\varepsilon_{ik} = \Delta\varepsilon\delta_{ik} + \Delta\varepsilon_{ik}^{(t)} \tag{10.2}$$

Here $\Delta\varepsilon$ represents a scalar contribution, arising from fluctuations in thermodynamic quantities such as the pressure, entropy, density, or temperature. It is a traceless tensor contribution of the dielectric tensor and results in scalar light scattering, including Rayleigh scattering and Brillouin scattering. Further, $\Delta\varepsilon_{ik}^{(t)}$ represents a traceless tensor contribution of the dielectric tensor, which can be written as:

$$\Delta\varepsilon_{ik}^{(t)} = \Delta\varepsilon_{ik}^{(s)} + \Delta\varepsilon_{ik}^{(a)} \tag{10.3}$$

where $\Delta\varepsilon_{ik}^{(s)}$ is the symmetric part of $\Delta\varepsilon_{ik}^{(t)}$, giving rise to Rayleigh-wing scattering, and $\Delta\varepsilon_{ik}^{(a)}$ is the anti-symmetric part, giving rise to (rotational and vibrational) Raman scattering. Due to the traceless nature of $\Delta\varepsilon_{ik}^{(t)}$ and $\Delta\varepsilon_{ik}^{(a)}$, Rayleigh-wing scattering and Raman scattering are depolarized scattering.

Since the objective of this research is Rayleigh-Brillouin scattering, we focus on the scalar contribution, $\Delta\varepsilon$, arising from fluctuations in thermodynamic quantities. Because the density ρ and temperature T are independent thermodynamic variables, we can separate the scalar fluctuations into two terms, the density fluctuations at constant temperature and the temperature fluctuations at constant density:

$$\Delta\varepsilon = \left(\frac{\partial\varepsilon}{\partial\rho}\right)_T \Delta\rho + \left(\frac{\partial\varepsilon}{\partial T}\right)_\rho \Delta T \tag{10.4}$$

According to [12], the second part of Eq. (10.4) contributes only for ~ 2% to the light scattering, hence is usually ignored. Then Eq. (10.4) becomes

$$\Delta\varepsilon = \left(\frac{\partial\varepsilon}{\partial\rho}\right)_T \Delta\rho \tag{10.5}$$

Again, we can choose the entropy s and pressure p to be the independent thermodynamic variables to represent the density fluctuations:

$$\Delta\rho = \left(\frac{\partial\rho}{\partial p}\right)_s \Delta p + \left(\frac{\partial\rho}{\partial s}\right)_p \Delta s \tag{10.6}$$

Here the first term describes pressure fluctuations (acoustic waves) leading to Brillouin scattering. The second term describes entropy fluctuations (isobaric density fluctuations) leading to Rayleigh-center scattering [11]. Therefore, in order to calculate the RB-

scattering profile, one must calculate the density fluctuations of the medium, which can be described by the Boltzmann equation.

10.2 From the Boltzmann equation to the Tenti S6 model

The Boltzmann equation for the microscopic phase space density *f(r, v, t)*, with *r* the position and *v* the velocity of the particle at time *t*, reads for a monatomic gas:

$$\left(\frac{\partial}{\partial t}+v\cdot\nabla\right)f=J(f,f) \tag{10.7}$$

where *J* is the collision operator, which for realistic models of polyatomic molecules involves both elastic and inelastic collisions to excited states. Since the collision operator is difficult to compute, a linearization (approximation) is used: $f(r,v,t) = \phi(v)\,(1 + h(r,v,t))$, where $\phi(v)$ is the Maxwell distribution. The thermal dynamics variables, such as density, velocity and heat flux are the velocity moments of *f*. It is the deviation *h* from thermal equilibrium that describes macroscopic transport. Therefore, the linearized Boltzmann equation is written as:

$$\left(\frac{\partial}{\partial t}+v\cdot\nabla\right)h=J[h] \tag{10.8}$$

This linearized Boltzmann equation can be cast into 6 or 7 matrix elements, which is now regarded as (Tenti) S6 [13] or S7 [14] model, respectively:

$$\begin{pmatrix} -J_{030}I_{00}^{00}-\frac{1}{n} & . & . & . \\ . & . & . & . \\ . & . & . & . \\ . & . & . & . \end{pmatrix}\begin{pmatrix} \nu(k,\omega) \\ . \\ . \\ . \end{pmatrix}=-\frac{1}{n}\begin{pmatrix} I_{00}^{00} \\ . \\ . \\ . \end{pmatrix} \tag{10.9}$$

For spontaneous Rayleigh-Brillouin scattering the right-hand side of Eq. (10.9) contains the initial condition, and the scattered light intensity is proportional to the real part of $\nu(k,\omega)$. It is possible to express the (6 or 7) matrix elements of *J* in Eq. (10.9) in terms of the transport coefficients, i.e. the shear viscosity, the bulk viscosity, and the thermal conductivity using the Chapman-Enskog analysis [15]:

$$\eta=-\frac{k_BT}{J_{020}}\ ,\ \eta_b=-\frac{2}{3}\left(\frac{c_{int}}{3/2+c_{int}}\right)^2\frac{k_BT}{J_{100}}$$
$$\kappa=-\frac{k_B^2T}{m}\cdot\frac{\frac{5}{2}J_{011}+c_{int}J_{110}+(10c_{int})^{1/2}J_{011}^{110}}{J_{011}J_{110}-\left(J_{011}^{110}\right)^2} \tag{10.10}$$

where c_{int} is the internal specific heat capacity per molecule, and J_{xxx}^{xxx} are the elements of the collision operator. In the other words, through the S6 or S7 model, RB-scattering profiles can be used to calculate the macroscopic transport coefficients, or vice-versa. It is worth noticing that in order to transfer the fluctuations of the dielectric tensor to the S6 or S7 model, many approximations (linearizations) are made and several physical

phenomena (such as the temperature fluctuations and depolarized scattering) are ignored. Therefore, the S6 or S7 model cannot be treated as fully accurate model.

11 Temperature-dependent transport coefficients

11.1 Shear viscosity

The shear viscosity expresses the ability of a fluid to flow freely. The macroscopic concept of shear viscosity is related to a statistical average of the (translational) momentum exchange between molecules of the fluid. For dilute gases, the shear viscosity is found to be proportional to the density, the mean free path, and the speed of sound in the gas. Because these three parameters are temperature- and pressure-dependent, the shear viscosity should be as well.

A widely used approximation to calculate the values of shear viscosity of diluted gases at different temperatures was put forward in a kinetic theory [16] using an idealized intermolecular-force potential. Sutherland's formula for the shear viscosity is written as [17]:

$$\frac{\eta}{\eta_0} \approx \left(\frac{T}{T_0}\right)^{3/2} \frac{T_0 + S_\eta}{T + S_\eta} \qquad (11.1)$$

where η is the shear viscosity, T is the temperature, S_η is the Sutherland constant, which is a characteristic property of gases, η_0 is the reference value of viscosity at reference temperature T_0. The parameters of Sutherland's formula for different gases and the errors due to the approximation are listed in Table 3.4.

Table 11.1, The parameters, errors and the applied temperature range of the Sutherland's formula of shear viscosity for different gases [17].

Gas	T_0 (K)	η_0 ($kg \cdot m^{-1} \cdot s^{-1}$)	Error (%)	Temperature range (K)	S_η (K)
Air	273	1.716e-5	±4	210-1900	111
Argon	273	2.125e-5	±3	200-1500	144
CO2	273	1.370e-5	±5	209-1700	222
CO	273	1.657e-5	±2	230-1500	136
N_2	273	1.663e-5	±3	220-1500	107
O2	273	1.919e-5	±2	230-2000	139
H2	273	8.411e-5	±2	80-1100	97

The shear viscosity for diluted gases is known to be nearly independent of pressure. For instance, an increase of pressure from 1 to 50 bar will only result in 10% change of the shear viscosity. In the present study the pressure remains below 3.5 bar, and hence the pressure effects on the transport coefficients can be treated as negligible.

Therefore, values for shear viscosity for different gases at different *p-T* conditions can be calculated according to Eq. (11.1) in combination with Table 3.4.

11.2 Thermal conductivity

From thermodynamics it is well known that a heat flow is the result of temperature variation, i.e., a temperature gradient. So the property, which is called thermal conductivity, is related to the vector rate of heat flow per unit area and the vector gradient of temperature. Similar to the shear viscosity, the thermal conductivity is also a temperature- and pressure-dependent transport coefficient of a gas. A Sutherland's formula can also be used to approximate the thermal conductivity at different temperatures for diluted gases with only 2 to 4 percent inaccuracy. Sutherland's formula for thermal conductivity is written as [17]:

$$\frac{\kappa}{\kappa_0} \approx \left(\frac{T}{T_0}\right)^{3/2} \frac{T_0 + S_\kappa}{T + S_\kappa} \tag{11.2}$$

where κ is the thermal conductivity, T is the temperature, S_κ is the Sutherland constant, which is different for different gases. κ_0 and T_0 are the reference values of thermal conductivity and temperature. The parameters of Sutherland's formula for thermal conductivity of different gases and the error due to the approximation are listed in Table 11.2.

Table 11.2 The parameters, errors and the applied temperature range of the Sutherland's equation for thermal conductivity of different gases [17].

Gas	T_0 (K)	κ_0 ($W \cdot K^{-1} \cdot m^{-1}$)	Error (%)	Temperature range (K)	S_κ (K)
Air	273	0.0241	±3	210-2000	194
Argon	273	0.0163	±4	210-1800	170
CO2	273	0.0146	±2	180-700	1800
CO	273	0.0232	±2	210-800	180
N_2	273	0.0242	±3	210-1200	150
O2	273	0.0244	±2	220-1200	240
H2	273	0.168	±2	200-1000	120

The thermal conductivity for diluted gases is nearly independent of pressure. Therefore, values of thermal viscosity for different gases at different *p-T* conditions can be calculated according to Eq. (11.2) in combination with Table 11.2.

11.3 RBS modelling of the scattering data

Both shear viscosity and thermal conductivity are transport coefficients required to calculate an RBS scattering profile within the Tenti S6 model. Therefore, the above

mentioned Sutherland's formulas need to be implemented in the so-called *RBS program,* a Fortran-based version of the Tenti S6 model, which was developed in [1]. The *RBS program* includes the temperature dependencies of shear viscosity and thermal conductivity for air. However, the formulas used for calculating shear viscosity and thermal conductivity are different from the formulas in Eq. (11.1) and Eq. (11.2).

The formulas used in the current *RBS program* are:

$$\eta = \eta_0 \cdot \left(\frac{T}{T_0}\right)^{3/2} \cdot \frac{T_0 + T_\eta}{T + T_\eta} \tag{11.3}$$

and

$$\kappa = \kappa_0 \cdot \left(\frac{T}{T_0}\right)^{3/2} \cdot \frac{T_0 + T_A \cdot e^{-T_B/T_0}}{T + T_A \cdot e^{-T_B/T}} \tag{11.4}$$

where η_0=1.864×10^{-5} kg$\cdot$m$^{-1}\cdot$s^{-1} is the reference shear viscosity and κ_0=0.0262 W$\cdot$K$^{-1}\cdot$m^{-1} is the reference thermal conductivity, at reference temperature T_0=300 K; T_η=110.4 K, T_A=245.4 K, and T_B=27.6 K are characteristic constants for air. Eq. (11.3) and (11.4) are from the book *Springer Handbook of Acoustics (Springer, 2007)* [18]. These two equations are also referred as the Sutherland's formulas in this book. So it is another form of the Sutherland's approximation. The numerical difference between Eq. (11.3) , (11.4) and Eq. (11.1), (11.2) is less than 1 % for a temperature range from 200 to 2000 K

The calculated transport coefficients of N_2 at different experimental temperatures are listed in Table 11.3. In Table 11.3, we assume that the bulk viscosity is proportional to the shear viscosity, which is a proper assumption for acoustic frequencies (the derivation of new values for the bulk viscosity will be explained in the following sections). In the next section, we will see that this assumption is not correct and new values for the bulk viscosity at light-scattering frequencies will be presented there. For comparison, the previously used values, which are always the values at room temperature, are also listed in the last row of the table (indicated in red).

Table 11.3 calculated transport coefficients of N_2

Temperature (K)	Shear viscosity (N*s/m2)	Bulk viscosity (N*s/m2)	Thermal conductivity (W/m*K)
254.7	1.563e-5	1.143e-5	0.02279
275.2	1.673e-5	1.224e-5	0.02436
336.6	1.950e-5	1.427e-5	0.02880
292 (used in the RBS program)	1.763e-5	1.290e-5	0.02520

Using the transport coefficients listed above, calculations with the RBS code for N_2 were performed.

Table 11.4 indicates that the newly obtained calculated line shapes (with modified transport coefficients) agree better with the experiments given the smaller residuals at the Brillouin peak positions.

Table 11.4 The measured and modelled scattering profiles (RBS code) for 366 nm using unmodified transport coefficients (the first two columns) and using modified transport coefficients (the last two columns). The results show that the residuals between the measured and modelled profiles are smaller when the transport coefficients are adapted to the proper temperature-dependent values for the transport coefficients.

T [℃]	3 bar (with unmodified transport coefficients)	residuals (with unmodified transport coefficients)	3 bar (with modified transport coefficients)	residuals (with modified transport coefficients)
-20	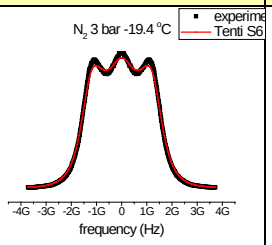	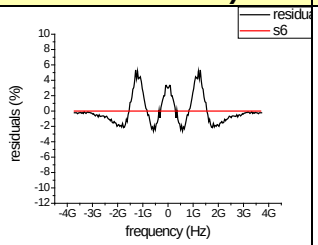	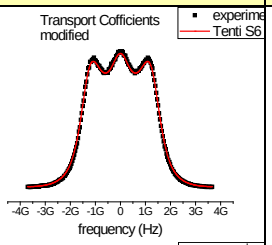	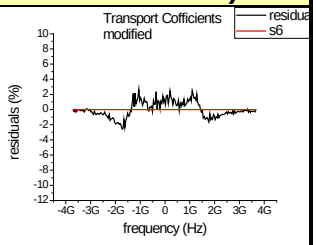
2	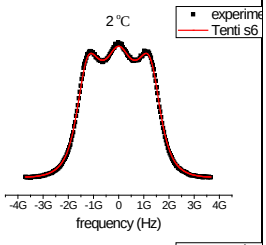	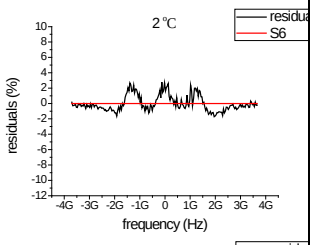	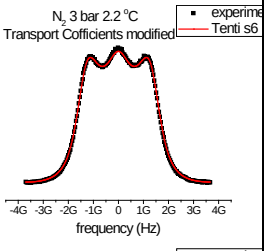	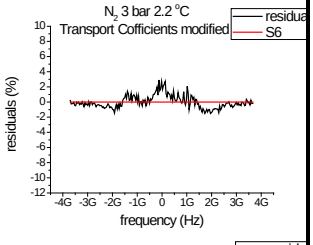
24	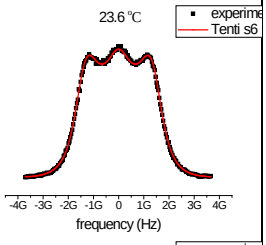	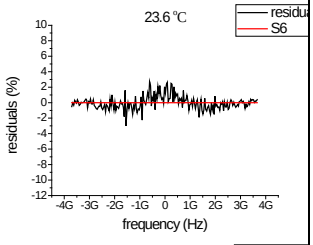	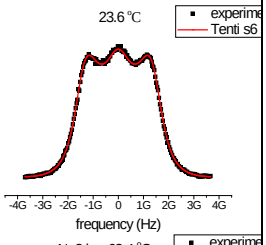	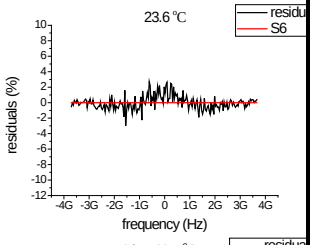
65	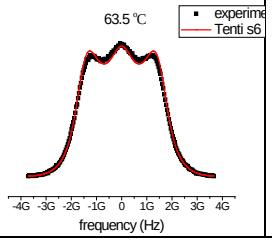	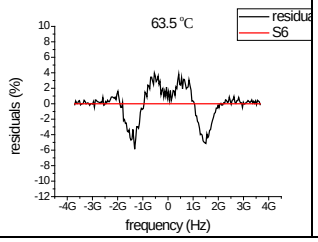	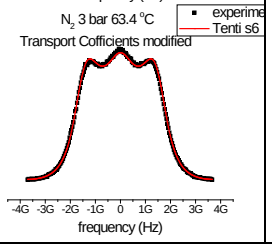	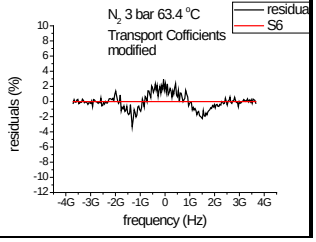

12 Derivation of the Bulk Viscosity

The bulk viscosity, η_b, expressing the resistance of a gas to rapid compression, is a parameter which is not well understood, or at least not well experimentally determined. This parameter is effectively a second macroscopic viscosity parameter depending on the internal degrees of freedom in the molecular constituents, and therefore does not play a role (η_b=0) in the thermodynamics of monoatomic gases. It must be considered what degrees of freedom effectively contribute to the bulk viscosity. Generally speaking, the bulk viscosity is larger when gas molecules process more internal (rotational and/or vibrational) degrees of freedom. Around room temperature (~ 300 K), the vibrational degrees of freedom for many diatomic gases are inaccessible due to the large vibrational characteristic temperature (3350 K for N_2 and 2240 K for O_2, thus much larger than room temperature [19]), and can therefore be safely neglected. Therefore, the bulk viscosity is influenced only by the rotational degrees of freedom. The dependence on the accessible degrees of freedom causes η_b to be temperature dependent. The value of η_b can in principle be measured via sound absorption and a number of studies have been performed in a variety of gases [20]. However, such measurements yield values for η_b in the MHz frequency domain, and they are most likely not directly applicable to the GHz regime, which is the region of concern for Rayleigh-Brillouin light scattering.

The Rayleigh-Brillouin profile for light scattering depends on the macroscopic transport coefficients (the shear viscosity η, the heat conductivity κ, the internal specific heat capacity c_{int}, and the bulk viscosity η_b), the temperature and pressure of the gas, and the mass of the particle constituents. While c_{int} and particle mass can be readily calculated and the transport coefficients η and κ are known from literature at high accuracy (see Table 3.4 and Table 11.2), the elusive transport coefficient η_b can be derived from Rayleigh-Brillouin scattering experiments if a model is established that links the scattering profile to the transport coefficients. Therefore, we can determine the effective bulk viscosity as the value providing the best fit between the measured scattering profiles (at high pressures) and profiles computed from the Tenti S6 model using the *RBS programme*. This is of course provided that all scattering processes contributing to the measured profile are understood and represented by the model.

In this section, we will derive the values of bulk viscosity for air and for N_2 at different temperatures in a least-square (χ^2) procedure, and we will show that similar to the shear viscosity, bulk viscosity also follows a linear trend with respect to the temperature.

Through the whole activity, air is treated as a single-component gas with an effective particle mass (m=29 amu) and effective transport coefficients, as reported in the literature for air.

It is worth noticing that values for the bulk viscosity can only be derived from measurements at high pressures where the bulk viscosity plays a decisive role. The data collection for 403 nm is still in progress. Such data will be collected and a bulk viscosity will be determined after finalizing this activity. For the time being, we directly apply the values measured at 366 nm to 403 nm, and good agreement between the 403 nm measurements and the S6 calculations are found (see Section 8.1), indicating that the bulk viscosity obtained from 366 nm measurements is also valid at 403 nm.

12.1 Least square fit between modelled and measured SRBS data

The χ^2 residual is defined as:

$$\chi^2 = \frac{1}{N}\sum_{i=1}^{N}\frac{\left[I_e(f_i) - I_m(f_i)\right]^2}{\sigma^2(f_i)} \qquad (12.1)$$

where $I_e(f_i)$ and $I_m(f_i)$ are the experimental and modelled amplitude of the spectrum at frequency f_i, and $\sigma(f_i)$ is the statistical (Poisson) error. Hence it is a measure for the difference between the measured and modelled RBS spectrum, which is should be 1 for a perfect fit between model and experiment. Figure 12.1 shows an example for extracting a value for η_b in the comparison of the Tenti S6 model with the Rayleigh-Brillouin profile in N_2 under conditions *T*=336.6 K and *p*= 3.40 bar. Figure 12.1 (a) shows the measurement (black dots) and the modelled scattering profiles for three different values of bulk viscosity η_b=1.0 $\times 10^{-5}$ kg·m^{-1}·s^{-1}, 2.0 $\times 10^{-5}$ kg·m^{-1}·s^{-1}, and 3.0 $\times 10^{-5}$ kg·m^{-1}·s^{-1}, respectively, and for values of the other transport coefficients as listed in Table 3.4 and Table 11.2. For the dimensionless internal specific heat capacity of internal degrees of freedom c_{int}, a value of 1 is used throughout. Residuals between the measurement and the three modelled scattering profiles are shown in Figure 12.1 (b). Figure 12.1 (c) shows a χ^2 calculation as a function of bulk viscosity employed in the Tenti S6 model. The optimized bulk viscosity is found where χ^2 has a minimum value, hence where the difference between the modelled and measured profiles is the smallest. The statistical error of this determination is calculated according to:

$$\sigma_{\eta_b} = \left(\frac{N'}{2}\frac{d^2\chi^2}{d\eta_b^2}\right)^{-1/2}, \qquad (2.2)$$

with N' the number of the independent samples in the spectrum and ~η_b the location of the minimum of χ^2. Accordingly, the statistical error in this case is 0.42$\times 10^{-5}$ kg·m^{-1}·s^{-1}, indicated in grey area in Fig. 2-1.

12.2 Derived bulk viscosity

By following the procedure discussed in Section 12.1, values of bulk viscosity for N_2 and for air at different temperatures can be obtained for the performed measurements. An example for the 3 bar data at 366 nm is given in Table 12.1 and Table 12.2. The results and the statistical errors are in Table 12.1 (for N_2) and Table 12.2 (for air). Values of the bulk viscosity derived here for 366 nm are implemented in the S6 model at 403 nm.

Table 12.1 Values and the statistical errors of bulk viscosity for N_2 at different temperatures, derived from the 3 bar data measured at 366 nm.

T (K)	Bulk viscosity (kg·m^{-1}·s^{-1})	Statistical error (kg·m^{-1}·s^{-1})
254.7	0.73 × 10^{-5}	0.13 × 10^{-5}
275.2	1.08 × 10^{-5}	0.24 × 10^{-5}
296.7	1.36 × 10^{-5}	0.43 × 10^{-5}
336.6	1.97 × 10^{-5}	0.42 × 10^{-5}

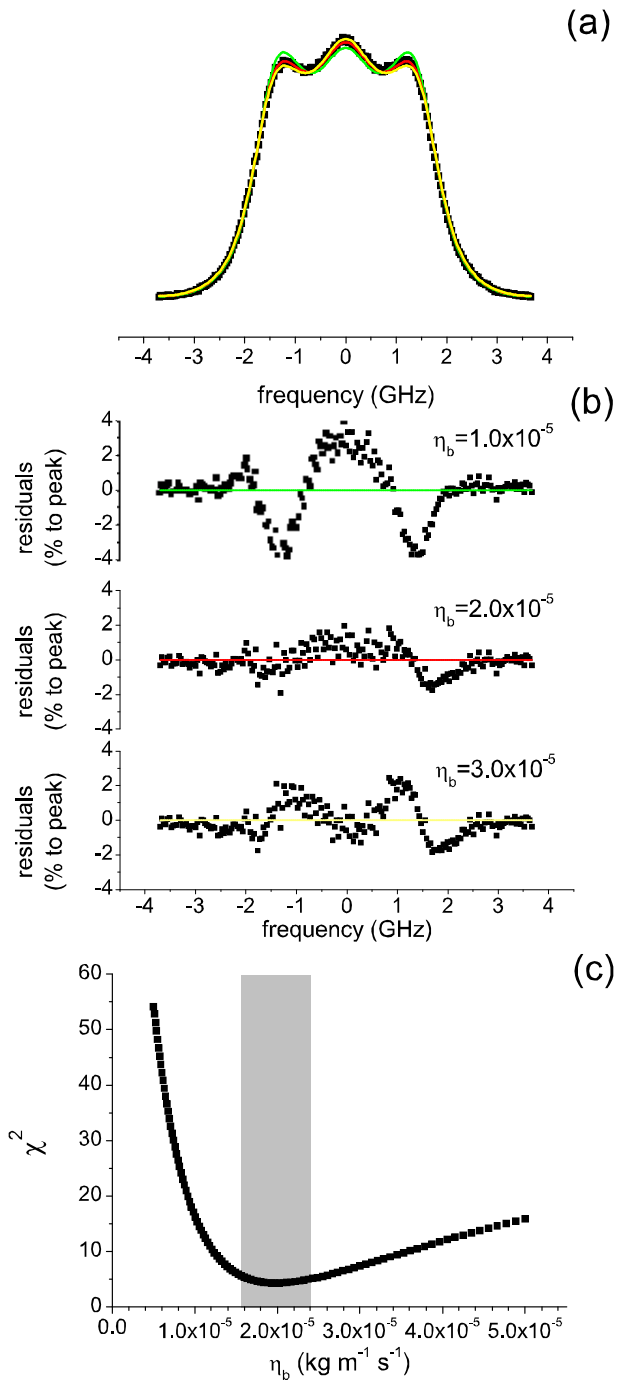

Figure 12.1: (a) Experimental RB scattering profile in N_2 for 3.40 bar and 336.6 K (black dots), and Tenti S6 calculations for bulk viscosity being 1.0 × 10^{-5} (green line), 2.0 × 10^{-5} (red line), and 3.0 × 10^{-5} (yellow line) kg·m^{-1}·s^{-1}, respectively. (b) Residuals between measured and calculated scattering profiles for these three values of bulk viscosity. (c) Plot of χ^2 as a function of bulk viscosity. The optimized value of bulk viscosity is found at the minimum of χ^2, with the grey area indicating the estimated statistical error, calculated according to Eq. (2.2).

Table 12.2 Values and the statistical errors of bulk viscosity for air at different temperatures, derived from the 3 bar data measured at 366 nm.

T (K)	Bulk viscosity ($kg \cdot m^{-1} \cdot s^{-1}$)	Statistical error ($kg \cdot m^{-1} \cdot s^{-1}$)
255.0	0.96×10^{-5}	0.08×10^{-5}
278.0	1.34×10^{-5}	0.16×10^{-5}
297.6	1.92×10^{-5}	0.16×10^{-5}
319.3	1.87×10^{-5}	0.16×10^{-5}
337.7	2.36×10^{-5}	0.18×10^{-5}

Values of bulk viscosity listed in Table 12.1 and Table 12.2 are plotted as black dots in Figure 12.2 and Figure 12.3, respectively.

For N_2 (Figure 12.2), we compare the newly derived results not only with the values from previous light-scattering experiments, but also with the values derived from sound absorption measurements (related to MHz acoustic frequencies). Values obtained by Vieitez *et al.* [2] (pink) for SRBS at 3 bar and room temperature slightly deviate from the presently derived values. However, no uncertainty was specified for that value, and if a similar uncertainty is assumed as in the present study, an agreement within combined 1σ is found. Meijer *et al.* [21] using CRBS (at 532 nm) at 5 bar N_2 deduced an even larger value, but still agree with the results obtained here within 2σ.

The present experimental results for the bulk viscosity in the temperature interval 254–337 K, shown as black dots in Figure 12.2, yield a linear dependence with temperature, roughly similar to the results obtained by Prangsma *et al.* [20] (red circles), using the sound absorption method. While the data of Prangsma *et al.* extend to temperatures as low as 180 K, and the present data extend to 337 K, for the overlapping range 250–300 K good agreement is found. Therefore, it is concluded that values of bulk viscosity for N_2 at GHz frequencies is comparable to the values at MHz range. This is very different from the CO_2 case, where orders of magnitude discrepancies were obtained [4, 5].

Similar to N_2, the derived values of bulk viscosity for air are plotted as black dots in Figure 12.3. Because there are no literature values (even for the sound absorption measurements) for air available, we compare them with the values of shear viscosity for air at each temperature, calculated according to Eq. (11.1). It is clear that, although Eq. (11.1) is rather complicated, shear viscosity establishes a linear dependency with respect to temperature. Therefore, we assume that the bulk viscosity for air is also linearly dependent on temperature. Figure 12.3 shows that the increase in η_b with temperature (1.653×10^{-7}) is more rapid than for η (0.477×10^{-7}). This result is not surprising because Prangsma *et al.* [20] also found similar differences in the temperature dependency of these two parameters for N_2.

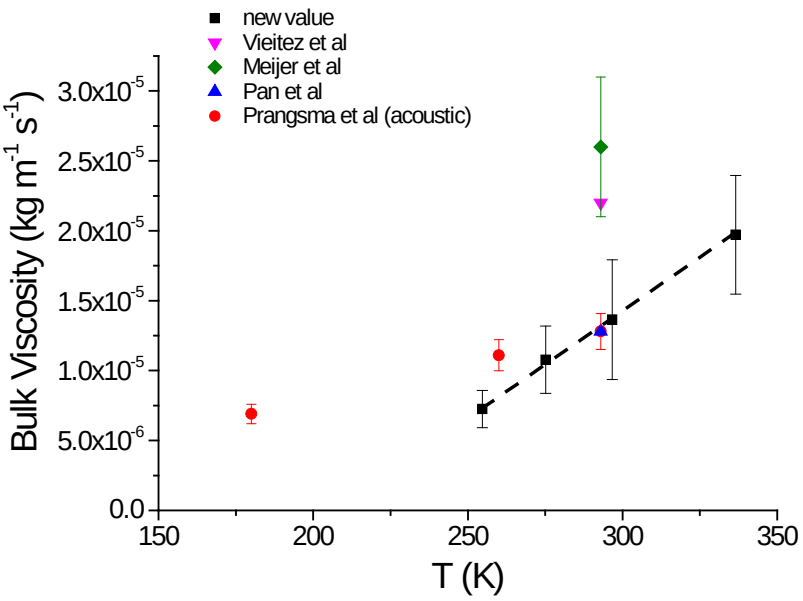

Figure 12.2: Comparison of values for the bulk viscosity measured from different experiments. Note that the result of Pan *et al.* [4] (blue triangle) overlays a data point by Prangsma *et al.* [20] (red circles). Data of Vieitez *et al.* [6] and Meijer *et al.* [21] are also included.

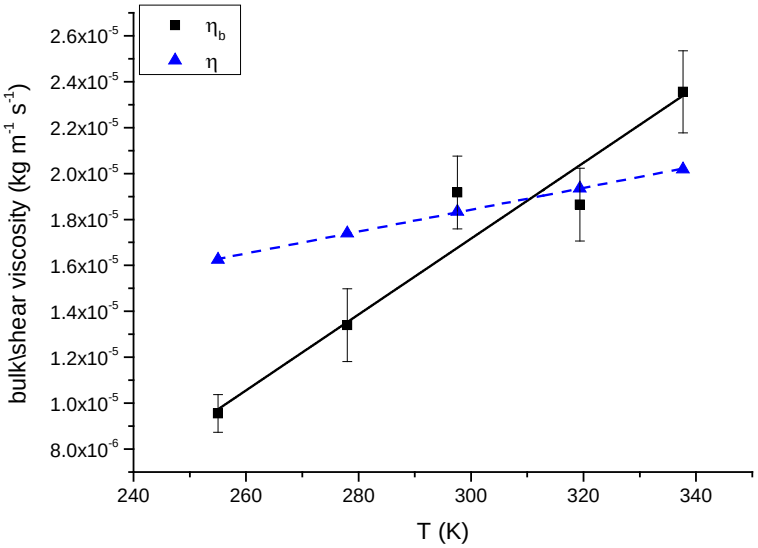

Figure 12.3: Bulk viscosities for air plotted as a function of temperature (black rectangular symbols) as determined from RB-scattering measurements around 3 bar air pressure and at 366.8 nm. The black straight line represents a linear fit to the experimental values. A comparison is made with values for the shear viscosity η (blue upper triangles) as calculated by Eq. (1.1). The blue dashed line is a linear fit to the η values.

12.3 Empirical equation for bulk viscosity

In view of the observed monotonic increase in η_b, a linear equation is used to represent the temperature effect on the bulk viscosity for N_2 and for air:
$\eta_b = a + b \cdot T$, yielding

$$a = (-3.18 \pm 0.15) \times 10^{-5},\ b = (1.54 \pm 0.05) \times 10^{-7} \text{ for } N_2 \qquad (12.2)$$

$$a = (-3.33 \pm 0.60) \times 10^{-5},\ b = (1.69 \pm 0.21) \times 10^{-7} \text{ for air} \qquad (12.3)$$

This empirical equation has been used in the measurement-model comparisons for experiments performed at 403 nm, because values for the bulk viscosity can only be derived from measurements at high pressures, and data collection for 403 nm is still in progress. A bulk viscosity will be determined after finalizing this activity. However, after directly apply Eq. (12.2) and (12.3) to 403 nm, we find good agreements between the 403 nm measurements and the model indicating that the bulk viscosity measured at 366 nm is also valid at 403 nm.

13 Angle and Mie-peak verification

13.1 Angle verification for the measurements at 366 nm

The value of the scattering angle was determined via assessment of the geometrical layout of the experimental setup, with an uncertainty of 0.9°, as documented in the final report of the previous activity [1]. It is found that this value can be further verified from the actual scattering data, as the RB-scattering profile is rather sensitive to the scattering angle. A complicating factor is that, both the bulk viscosity η_b and the scattering angle θ influence the RB profile, and for the data measured for 3 bar, the η_b value has the largest impact. Moreover, the scattering angle θ mainly affects the total width of the RB-scattering profile, where the bulk viscosity η_b determines the pronounced occurrence of Brillouin side features. Therefore the two parameters are not strongly correlated. For this reason, for 3 bar data a procedure is adopted to determine a preliminary value for the bulk viscosity η_b, and then subsequently a fit to the scattering angle was performed following the same least-square fitting procedure as for the bulk viscosity. An example of such a least-squares minimization to angle θ, for an experimental RB scattering profile of air at 366 nm, 337.7 K and 3.30 bar, is presented in Figure 13.1. Figure 13.1 (a) shows the residuals between the measurement (black dots) and the modelled scattering profile (red line), when three different scattering angles, 89.2°, 89.8°, and 90.4°, are used for modelling. The χ^2 values calculated from the residuals are 2.55, 1.68, and 2.44 for these three angles. In Figure 13.1 (b), values of χ^2 are plotted as a function of scattering angles θ employed in the S6 model. The χ^2 fit, represented by the full (green) line, yields an optimized scattering of θ=89.8° with a 1σ standard deviation less than 0.1°. This agrees well with the direct geometrical assessment of the angle 90±0.9°. The determined scattering angles for all the five temperatures of 3 bar air are plotted in Figure 13.1 (c), indicating that the scattering angles for the same temperature settings (hence number densities) are the same. It is noted that a leftmost point in (c) pertain to data recorded with time intervals of several months; after such down time, a full alignment of the optical system had to be performed, explaining the 0.4° scattering angle deviation.

By following the same procedure, the derived scattering angles for all the measurements in air and in N_2 at 366 nm are derived and listed in Table 13.1 and Table 13.2, respectively. All the derived values of θ are found in the range 90 ± 0.9°. The slight deviations are attributed to realignment of the laser beam path through the scattering cell. The number density variation inside the cell causes the index of refraction to change and therewith the angle of the laser beam with respect to the Brewster windows. Note that outside the cell, the atmospheric pressure is maintained. In order to keep the enhancement cavity at optimized circulating intensity, angular variations of a few 0.1° have to be imposed consequently.

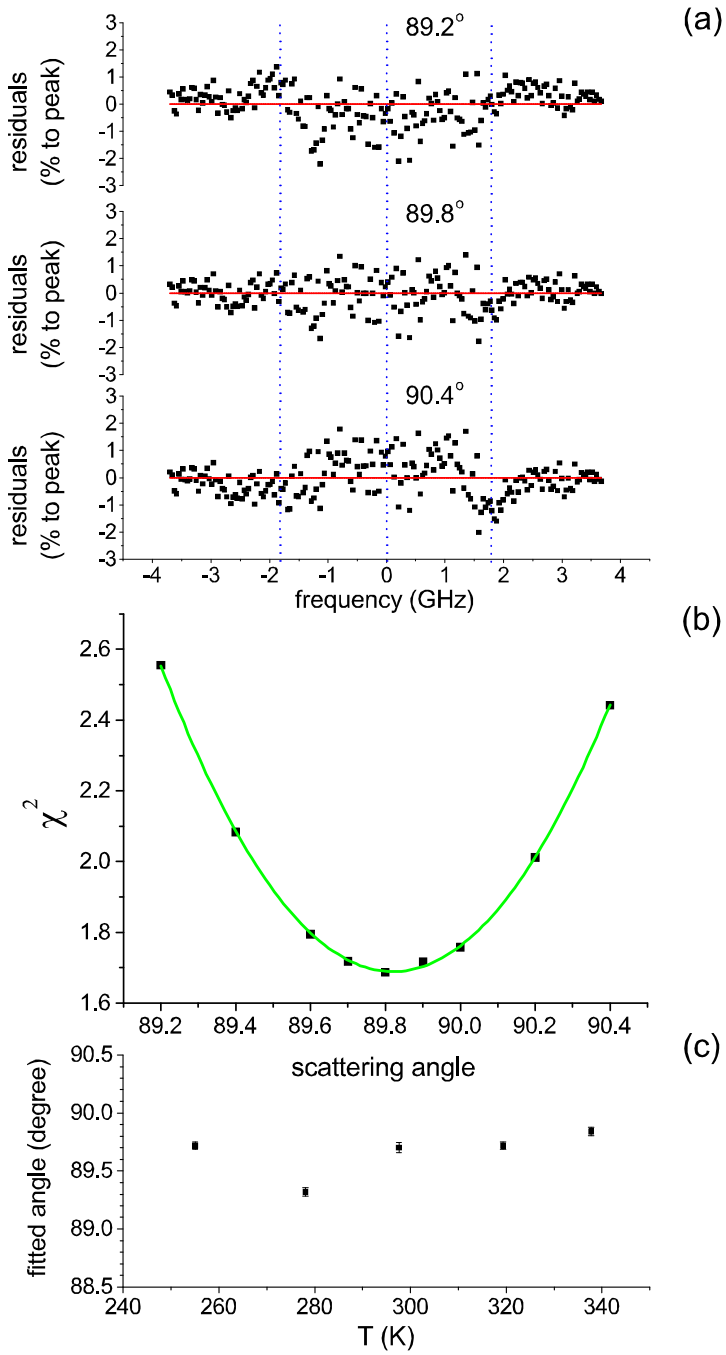

Figure 13.1: Graphical representation of the procedure for verifying the scattering angle θ; (a) Residuals between the experimental RB-scattering profile for air, measured at 366 nm, 337.7 K and 3.30 bar, and the Tenti S6 calculations for three selected scattering angles: 89.2°, 89.8°, and 90.4°. Note that a value of η_b=2.36 × 10^{-5} kg·m^{-1}·s^{-1}, a result of the study mentioned in the previous section, was adopted to produce the theoretical curve. (b) Values of χ^2 , calculated according to the residuals, as a function of scattering angle used for Tenti S6 modelling. The green line is the parabolic fit to the χ^2 values, giving a minimum at 89.8°. The estimated error (1σ) for this angle determination is less than 0.1°. (c) Optimized scattering angles together with their standard errors for all the measurements in air at 3 bar.

Table 13.1 the derived scattering angles for all the measurements in air under different gas conditions.

T (K)	Scattering angle (0.75 bar)	Scattering angle (1 bar)	Scattering angle (3 bar)
255	90.1	90.0°	89.7°
275	90.2	90.3°	89.3°
295	90.2	90.4°	89.7°
315	90.1	90.4°	89.7°
335	90.2	90.5°	89.8°

Table 13.2 the derived scattering angles for all the measurements in N_2 under different gas conditions.

T (K)	*Scattering angle (1 bar)*	*Scattering angle (3 bar)*
255	89.7°	89.4°
275	89.6°	89.5°
295	89.7°	89.6°
335	89.8°	89.6°

13.2 Angle verification for the measurements at 403 nm

For the 403 nm measurements, the procedure of verification of the scattering angle has been discussed in Section 8.1. In summary, we find that the scattering angle was ~2° larger than 90° because in order to switch the wavelength from 366 nm to 403 nm, all the optics, including the enhancement cavity, the beam steering optics and the Fabry-Perot interferometer were changed. In Section 8.1 it was shown that the scattering angle stays the same (~91.7°) for a period of 10 months, and for sequences of measurements on various gases at different temperatures and pressures.

13.3 Stray light verification

Due to the small scattering cross section of the gas molecules, any RB detection setup is sensitive to stray light from cell walls, cell windows, and from the beam-steering optics. Stray light typically exhibits the same bandwidth as the incident laser beam (2 MHz). It is a Mie-type scattering and is centred exactly at the laser frequency. Therefore, stray light will appear as a Lorentzian line located exactly in the centre of the RB scattering profile with 232 MHz bandwidth (for the 366 nm data, and smaller for the 403 nm data), corresponding to the FWHM of the FPI. Mie scattering induced by aerosol particles in the scattering cell would result in a similar frequency profile. Precautions were therefore taken to avoid aerosol scattering. Because there is a systematic structure of the residuals for nearly all measurements, with the central part of the Rayleigh peak being slightly higher than the model prediction and the Brillouin peaks lower. This may be interpreted as evidence for stray light contributing to the scattering profile in the present measurements. The fact that the deviations are most apparent at the low-pressure measurements supports this hypothesis, since the relative contribution of stray light should be largest at low pressures where the backscattered signal is the lowest.

However, it is worth noting that the additional residuals at the centre of the Rayleigh peak have a FWHM more than 2 times larger than 232 MHz. This may imply that the increased intensity is not only attributable to stray light.

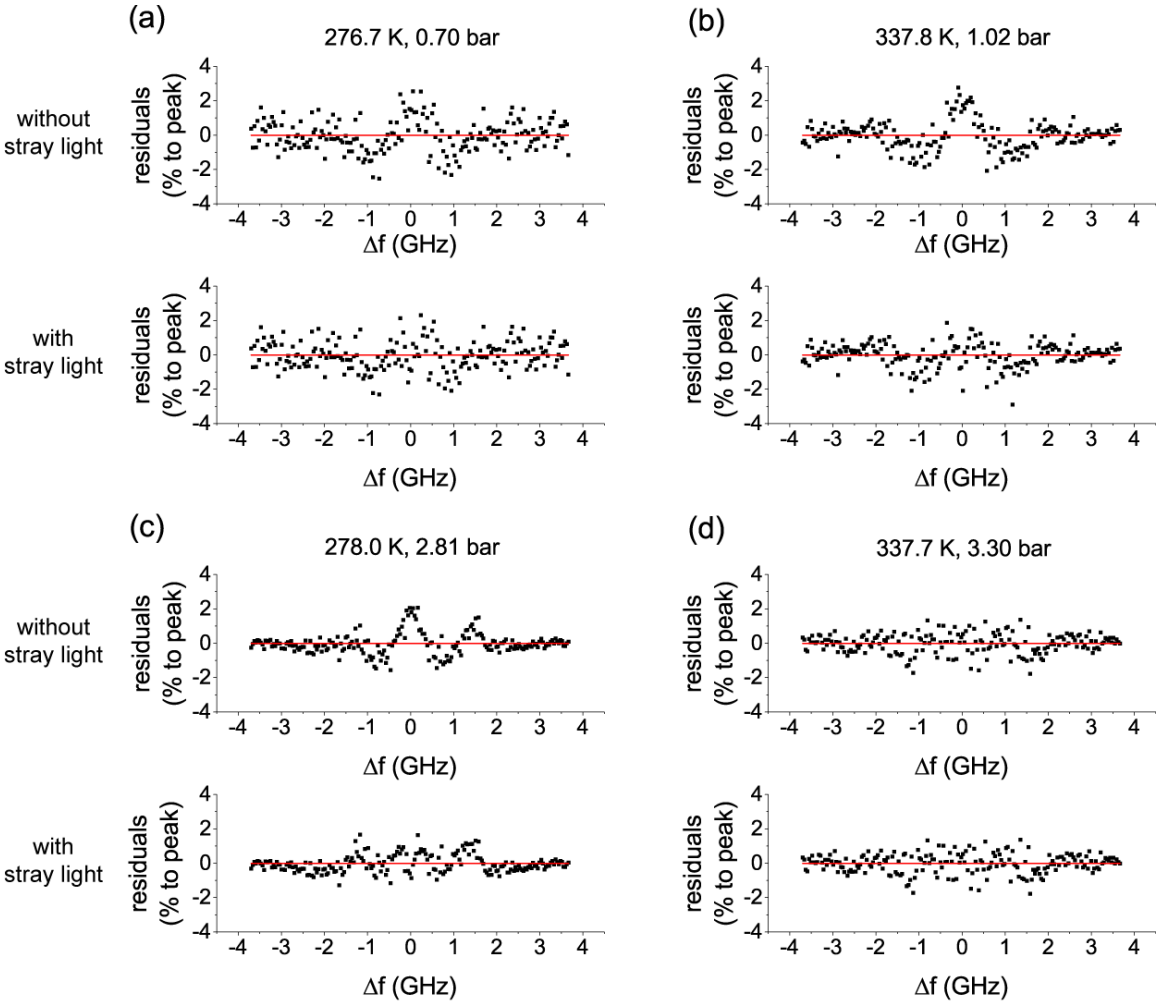

Figure 13.2: Comparison of residuals for four selected sample measurements of RB scattering profiles in air at 366 nm without and with stray light included.

In order to test the stray light hypothesis, we modified the *RBS program* added a spectral contribution $S\delta(f_i)$ for stray light to the modelled amplitude function $I_m(f_i)$, thus yielding a total amplitude of $I'_m(f_i) = I_m(f_i) + S\delta(f_i)$ [22]. After replacing the amplitude function $I_m(f_i)$ by $I'_m(f_i)$ in the analysis, the entire modelling procedure was repeated using the least-squares procedure with respect to the relative intensity of the stray light S. Via this means, in most cases, an improved fit to the scattering profile was obtained, for stray light intensities of S = 0–0.4%. Figure 13.2 shows four residuals of profiles with and without the inclusion of stray light. It can be seen that the fit between the modelled and measured data improved in some (Figure 13.2 (a) and Figure 13.2 (c)) but not all cases after the inclusion of a stray light contribution. The χ^2 is reduced from

2.15 to 1.93 when S=0.33% for Figure 13.2 (a), and from 5.67 to 4.00 when S=0.44% for Figure 13.2 (c). However, in some cases (e.g. Figure 13.2 (b), although the χ^2 is reduced from 2.65 to 1.80 after applying the stray light subtraction procedure, it leads to an over fitting, resulting in a conspicuous dip for the residuals $I_e(f_i) - I'_m(f_i)$ at f_i=0, with systematic deviations around ±1 GHz remaining, which is around the positions of the Brillouin peaks. For a few cases, Figure 13.2 (d) for example, the stray light does not play a role: a minimum of χ^2 is found when S=0%.

14 Temperature Retrieval from Spontaneous RB-Scattering Profiles

Besides determining wind velocities, retrieval of temperatures of the atmosphere with RB LIDAR methods is another interesting target for aeroscientists [23]. However, due to the low RB scattering cross section and complicated scattering profile calculations for air, the accuracy is limited. Therefore, Brillouin LIDAR techniques have only been applied to measure the temperature of water [24]. Here we demonstrate that with the RB scattering method, in comparison with the Tenti S6 model, it is possible to measure the temperature of air under atmospheric pressures.

Figure 14.1 shows the comparisons between the measured temperatures (with the PT-100 temperature sensors in the experimental setup) and derived temperatures for 0.75 bar and 1 bar data measured at 366 nm. The derived values are obtained by fitting *T* to a minimal χ^2, when the other parameters are fixed to the values used in the Tenti S6 calculations. The dashed black lines represent the condition where the derived and measured temperatures are equal. It is found that the derived temperatures agree well with the real (measured) temperatures for all the conditions: the maximal difference is 0.4 K.

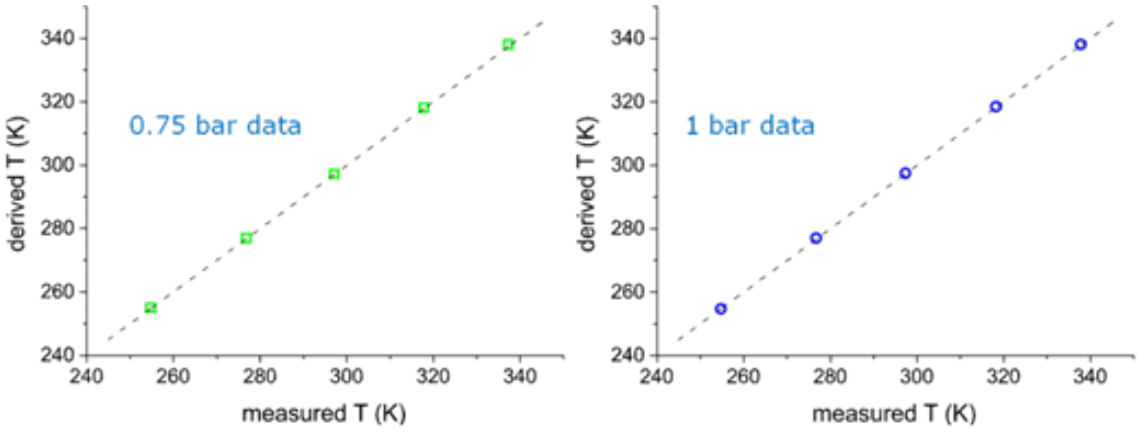

Figure 14.1: Temperature retrieval from the RB-scattering profiles measured in the present study, derived from measurements at 366 nm.

The same procedure has also been applied to the 403 nm measurements, and the results are shown in Figure 14.2. The dashed black line represents the condition where the derived and measured temperatures are equal, and the red line represents a linear fit to the derived temperatures. Note that the scattering angle for retrieving the temperature is set at 91.7 degree instead of 90 (cf. Section 8.1 for the reason). The large error bars in this figure are due to the uncertainty of the scattering angle for the 403 nm measurements.

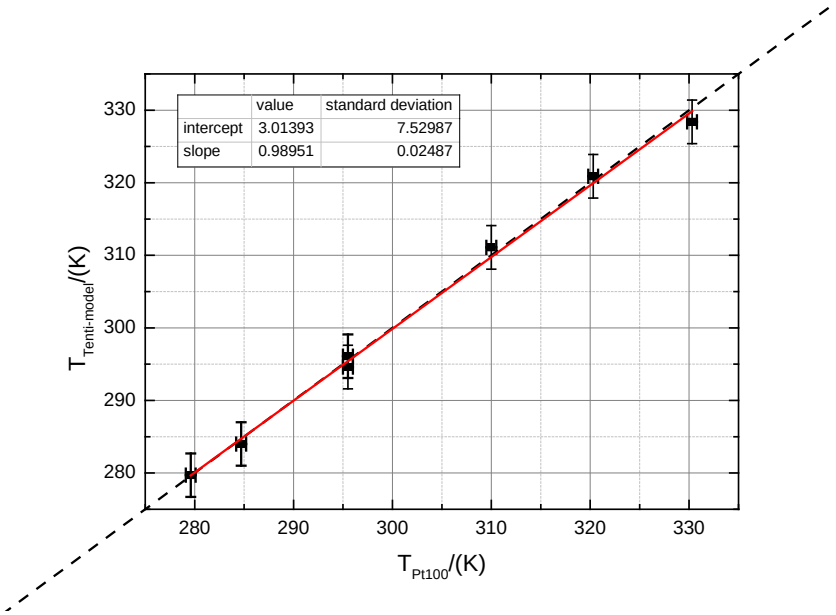

Figure 14.2: Temperature retrieval from the RB-scattering profiles measured at 403 nm. The dashed black line represents the condition where the derived and measured temperatures are equal, and the red line represents a linear fit to the data points (black squares).

15 Correction for contribution by Rotational Raman scattering

In the previous project [1] and for the first part of this report (all for 366 nm measurements), it was found that the side wings of the measured scattering profiles are always higher than side wings of the Tenti S6 calculations. This phenomenon was ascribed previously to broadband fluorescence of the cell windows. However, fluorescence is unlikely to play a role here, because non-coated windows are used for the laser beam to pass through the cell and bare fused silica exhibits a fluorescence spectrum longward of 400 nm [25], while this part of the spectrum is filtered before detecting the scattered light (at 366 nm). Raman scattering, amounting to ~2.5% of the total cross section, is another possible source of background, because as explained in Chapter 10, the Tenti S6 model does not include Raman scattering. In Section 7.1.4, it has been demonstrated that after utilizing a 1 nm bandwidth filter for all the 403 nm measurements, most of the rotational Raman scattering and all the vibrational scattering was filtered out and the side wings of the measurements are reduced to the original Tenti model. However, the measurements still have 1~2% difference with respect to the Tenti S6 model (see Chapter 8 for all the measurements), which is at the same level as for the 366 nm measurements without utilizing a 1 nm filter. This demonstrates that all the previous measurements at 366 nm (see [1] and Chapter 4) without a 1 nm filter are reliable.

16 The role of polarization

As explained in Chapter 10, the Tenti S6 model does not consider depolarized scattering, including Rayleigh-wing scattering and (rotational and vibrational) Raman scattering.

Rayleigh-wing scattering, i.e. the scattering in the wing of the Rayleigh profile, is the scattering due to fluctuations in the orientation of anisotropic molecules. It does not occur for molecules with an isotropic polarizability tensor, such as O_2, N_2 and CO_2. Therefore, Rayleigh-wing scattering does not play a role for all the laboratory air and N_2 measurements performed in this project. However, for the real atmospheric measurements, where a large amount of H_2O molecules exist, Rayleigh-wing scattering might need to be taken into account. Since the molecular reorientation process is very rapid, Rayleigh-wing scattering is broadband [11]. However, this component occurs in the wings of the Rayleigh profile, so it cannot be fully separated by means of narrow band filter (otherwise parts of the pure Rayleigh scattering will also be removed). Fortunately it has been proved that even for air with saturated water vapour we did not detect any significant Rayleigh-wing scattering effect [1], suggesting that the Rayleigh-wing scattering effect in the real atmospheric measurements are negligible.

For Raman scattering, it has been demonstrated previously that most of the signal can be filtered out by a 1 nm bandwidth filter. However, there exists a special part of rotational Raman scattering, which corresponds to no change of the rotational levels of the gas molecules (i.e. $\Delta J = 0$), but corresponds to a change of the projection of the rotational angular momentum of the molecules on a space-fixed axis (i.e. $\Delta m_J \neq 0$) [26]. Since there is no change in rotational levels, there is no change in energy, hence no frequency shift. However, its Raman scattering nature results in a depolarization effect. This scattering component is estimated to be ~1 % of the total scattering [26], which agrees with the amount of additional 1~2 % signal we detect in the centre of RB-scattering profile (see Figure 13.2 as an example). Therefore we hypothesize that the additionally detected signal for all the measurements at $\Delta f = 0$ is due to this Raman component instead of a Mie (or elastic) scattering. It is worth noticing that since this Raman scattering component occurs exactly at the centre of RB-scattering profile, it cannot be removed by a narrow bandwidth filter. A polarizer is not expected to completely remove the depolarized light neither, because the scattered light is depolarized into all the possible directions.

These phenomena of depolarization by Rayleigh-wing scattering and rotational Raman scattering could be subject of future investigations.

17 Gas Mixtures

Through the whole activity, we treat air as a single-component gas with an effective (weighted averaged) particle mass 29.0 u, and effective transport coefficients as obtained from experiment. This method entails an approximation, but will likely be valid because the two major components of air, N_2 and O_2, have similar molecular mass and molecular structure. However, for a gas mixture with significantly different components, this method should not be valid anymore.

Let us take He + Ar mixture as an example. Because the scattering signal is proportional to $(n-1)^2$, with *n* being the refractive index of the gas, the total scattering signal for He (with *n*=1.000035) is 65 times smaller than that for Ar (with *n*=1.000284). Furthermore, because the Rayleigh width is proportional to $m^{-1/2}$, the scattering profile of He (*m*=4 u) is more than 3 times broader than that of Ar (*m*=40 u). Therefore the maximum scattering amplitude for He is $3\times 65 \approx 200$ times smaller than that for Ar. Such small contributions to the scattering signal can in most cases be ignored. However, from the experimental observations shown in Figure 17.1, it is clear that the measured scattering profile of 2 bar He + 2 bar Ar mixture is significantly different from the scattering profile of 2 bar Ar. This demonstrates that the light He atoms have a significant influence on the scattering signal – although not directly from the scattering of the atoms itself.

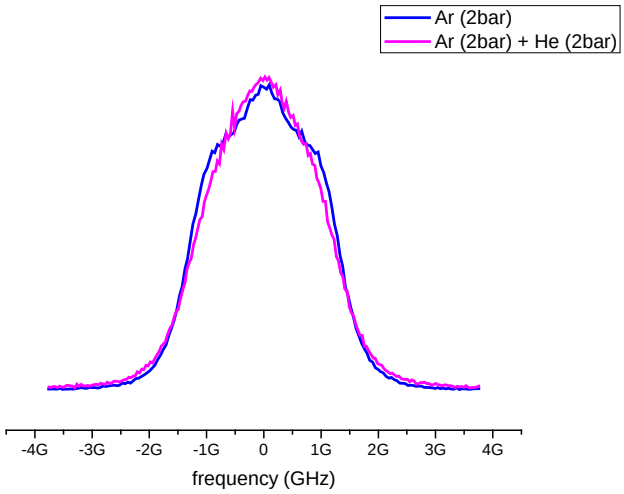

Figure 17.1: RB scattering profile of 2 bar Ar (blue) and of 2bar Ar + 2bar He mixture (purple).

It is worth keeping in mind that, although treating air as a single-component gas is proved to be accurate within 1~2% accuracy, it is still an approximation to the Tenti S6 model.

18 Conclusion part III

The objective of this part was to further validate the Tenti S6 model and to improve it. We have found that the effect of the temperature-dependence of shear viscosity and thermal conductivity can be accounted for. Their values at different temperatures can be calculated according to Sutherland's formula, Eq. (11.1) and (11.2) respectively. These formula have been implemented in *RBS program*, developed by W. van de Water, basing on the Fortran code from Xingguo Pan [7], who transferred the original Tenti code of SRBS into dual-applications (for both SRBS and CRBS). For the bulk viscosity, a parameter which is still not well-understood, values are derived via a least-square procedure to fit the 3 bar measurements at 366 nm, resulting in empirical equations (Eq. (12.2) for N_2 and Eq. (12.3) for air) to calculate the bulk viscosity at different temperatures. This method will be further tested for the set of data at 403 nm, which is currently only partially complete. Furthermore, the uncertainty of the scattering angle and the influence of the stray light on the measured scattering profiles have been investigated. The persistence of the systematic deviations between measured spectra and the model, even after fitting the bulk viscosity, scattering angle and elastic scattering, suggests that the Tenti model does not fully describe our experiment. One of the possible reasons is that the Tenti S6 model only deals with the polarized scattering, while our experiment is also sensitive to depolarized light (see Chapter 16). In a more general sense, the entire Tenti procedure is an approximate method to replace a description with the full Boltzmann equation. It has been shown here that the approximation method is adequate down to the level of 1%. A final conclusion pertains to the fact that air is treated as a single-component gas, with (known) macroscopic transport coefficients and a well-defined (and calculable) mass. Measurements are in preparation to validate the applicability of the Tenti model to a two-component gas.

19 Conclusions and further outlook

This activity set out to further validate the Tenti-model in a wider parameter space, specifically at different temperatures, wavelengths and scattering angles, with the first two achieved successfully. Although preparations for angle-dependent studies have reached a stage (with a new experimental setup ready) that these may be performed soon, it could not be studied due to the delay of the second target and the unexpected work load of building a completely new experimental setup with high accuracy and stability. Future activities recommended are to investigate the angle-dependence of the RB scattering profile, and the influence of depolarized scattering.

Depolarization scattering, such as Raman scattering or Rayleigh-wing scattering, are not considered by the Tenti S6 model. Rayleigh-wing scattering is induced by anisotropic molecules, hence does not play a role in experiments focusing on air, N_2 and O_2. For real atmospheric measurements, where H_2O molecules largely exist, the phenomena has also been proved to be negligible. Since this scattering occurs in the wings of Rayleigh, it cannot be separated from by means of any narrow band filters without destroying the whole RB-scattering profile. On the other hand, most of Raman scattering, corresponding to a large frequency (wavelength) shift, can be filtered out by a narrow bandwidth (1 nm or 0.5 nm) filter, while the rest of it is concluded to be (part of) the reason for the additional signal exactly at laser frequency, namely the center of the RB scattering profile.

It is of importance to notice that although both the Rayleigh-wing scattering and the Raman scattering are depolarized, the scattered light is depolarized to any possible angles, making the attempt to block all the depolarized light by using a polarizer impossible. Therefore, we suggest considering the depolarization phenomena in the real atmospheric measurements, which to our knowledge has not been well-studied yet and might be one of the objectives of our next study.

20 References

[1] W. Ubachs, E.-J. van Duijn, M.O. Vieitez, W. van de Water, M. Dam, J.J. ter Meulen, A.S. Meijer, J. de Kloe, A. Stoffelen, E.A.A. Aben, A spontaneous Rayleigh-Brillouin scattering experiment for the characterization of atmospheric lidar backscatter, ESA, 2009
[2] M.O. Vieitez, E.J. van Duijn, W. Ubachs, B. Witschas, A. Meijer, A.S. de Wijn, N.J. Dam, W. van de Water, Coherent and spontaneous Rayleigh-Brillouin scattering in atomic and molecular gases and gas mixtures, Physical Review A, 82 (2010) -.
[3] R.E. Graves, B.M. Argrow, Bulk viscosity: Past to present, Journal of Thermophysics and Heat Transfer, 13 (1999) 337-342.
[4] X.G. Pan, M.N. Shneider, R.B. Miles, Coherent Rayleigh-Brillouin scattering in molecular gases, Physical Review A, 69 (2004).
[5] X.G. Pan, M.N. Shneider, R.B. Miles, Power spectrum of coherent Rayleigh-Brillouin scattering in carbon dioxide, Physical Review A, 71 (2005) 045801.
[6] M.O. Vieitez, E.J. van Duijn, W. Ubachs, B. Witschas, A. Meijer, A.S. de Wijn, N.J. Dam, W. van de Water, Coherent and spontaneous Rayleigh-Brillouin scattering in atomic and molecular gases and gas mixtures, Physical Review A, 82 (2010).
[7] X. Pan, Coherent Rayleigh-Brillouin Scattering, in, PRINCETON UNIVERSITY, 2003, pp. 162.
[8] Y. Ma, F. Fan, K. Liang, H. Li, Y. Yu, B. Zhou, An analytical model for Rayleigh-Brillouin scattering spectra in gases, Journal of Optics, 14 (2012).
[9] Y. Ma, H. Li, Z. Gu, W. Ubachs, Y. Yu, J. Huang, B. Zhou, Y. Wang, K. Liang, Analysis of Rayleigh-Brillouin spectral profiles and Brillouin shifts in nitrogen gas and air, Optics Express, 22 (2014) 2092-2104.
[10] B.W. Witschas, B., Analytical model for Rayleigh-Brillouin line shapes in air, Applied Optics, 50 (2011) 267-270.
[11] R.W. Boyd, Nonlinear optics, 2008.
[12] I.L. Fabelinskiĭ, Molecular Scattering of Light, By Immanuil L. Fabelinskii. Translated From Russian, by Robert T. Beyer, 1968.
[13] G. Tenti, C.D. Boley, R.C. Desai, Kinetic-Model Description of Rayleigh-Brillouin Scattering from Molecular Gases, Canadian Journal of Physics, 52 (1974) 285-290.
[14] C.D. Boley, G. Tenti, R.C. Desai, Kinetic Models and Brillouin-Scattering in a Molecular Gas, Canadian Journal of Physics, 50 (1972).
[15] S. Chapman, T.G. Cowling, The Mathematical Theory of Non-uniform Gases: An Account of the Kinetic Theory of Viscosity, Thermal Conduction and Diffusion in Gases, Cambridge University Press, 1970.
[16] W. Sutherland, The viscosity of gases and molecular force, The London, Edinburgh, and Dublin Philosophical Magazine and Journal of Science, 36 (1893) 507-531.
[17] F.M. White, Viscous Fluid Flow, McGraw-Hill, 1991.
[18] T.D. Rossing, Springer Handbook of Acoustics, Springer, 2007.
[19] G. Emanuel, Bulk viscosity in the Navier-Stokes equations, International Journal of Engineering Science, 36 (1998) 1313-1323.
[20] G.J. Prangsma, A.H. Alberga, J.J.M. Beenakker, Ultrasonic determination of the volume viscosity of N2, CO, CH4 and CD4 between 77 and 300 K, Physica, 64 (1973) 278-288.

[21] A.S. Meijer, A.S. de Wijn, M.F.E. Peters, N.J. Dam, W. van de Water, Coherent Rayleigh-Brillouin scattering measurements of bulk viscosity of polar and nonpolar gases, and kinetic theory, Journal of Chemical Physics, 133 (2010).
[22] Z.Y. Gu, W. Ubachs, Temperature-dependent bulk viscosity of nitrogen gas determined from spontaneous Rayleigh-Brillouin scattering, Optics Letters, 38 (2013) 1110-1112.
[23] H. Shimizu, K. Noguchi, C.Y. She, Atmospheric-Temperature Measurement by a High Spectral Resolution Lidar, Applied Optics, 25 (1986) 1460-1466.
[24] K. Schorstein, A. Popescu, M. Gobel, T. Walther, Remote water temperature measurements based on Brillouin scattering with a frequency doubled pulsed Yb : doped fiber amplifier, Sensors, 8 (2008) 5820-5831.
[25] H.B. Zhang, Z.J. Yuan, J. Zhou, J.X. Dong, Y.R. Wei, Q.H. Lou, Laser-induced fluorescence of fused silica irradiated by ArF excimer laser, Journal of Applied Physics, 110 (2011).
[26] R.B. Miles, W.R. Lempert, J.N. Forkey, Laser Rayleigh scattering, Measurement Science & Technology, 12 (2001) R33-R51.